



HAL
open science

Lattice, magnetic excitations and their coupling in multiferroic materials

Jiaji Liu

► **To cite this version:**

Jiaji Liu. Lattice, magnetic excitations and their coupling in multiferroic materials. Strongly Correlated Electrons [cond-mat.str-el]. Université Paris 7 – Denis Diderot, 2013. English. NNT: . tel-01493385

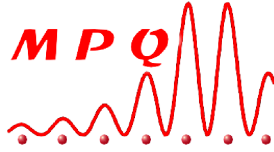
HAL Id: tel-01493385

<https://hal.science/tel-01493385>

Submitted on 21 Mar 2017

HAL is a multi-disciplinary open access archive for the deposit and dissemination of scientific research documents, whether they are published or not. The documents may come from teaching and research institutions in France or abroad, or from public or private research centers.

L'archive ouverte pluridisciplinaire **HAL**, est destinée au dépôt et à la diffusion de documents scientifiques de niveau recherche, publiés ou non, émanant des établissements d'enseignement et de recherche français ou étrangers, des laboratoires publics ou privés.



**THESE DE DOCTORAT DE
L'UNIVERSITE PARIS DIDEROT**

Spécialité : **Physique**

Ecole doctorale : ED 518

Présentée par :

JIAJI LIU

Pour obtenir le grade de

DOCTEUR DE L'UNIVERSITE PARIS DIDEROT

Sujet de la thèse :

**Lattice, magnetic excitations and their coupling in
multiferroic materials**

soutenue le 15 Avril 2013.

devant le jury composé de :

Ricardo Lobo	Directeur des Recherches LPEM-ESPCI, Paris	Rapporteur
Yves Dumont	Professeur Université de Versailles, St-Quentin-en-Yvelines	Rapporteur
Dorothee Colson	Chercheur CEA, Saclay	Membre du jury
Virginie Simonet	Chercheur Institut Néel, Grenoble	Membre du jury
Alain Sacuto	Professeur Université Paris Diderot, Paris	Codirecteur de Thèse
Maximilien Cazayous	Professeur Université Paris Diderot, Paris	Directeur de Thèse

Acknowledgement

At the end of my thesis, I would like to thank all the people who accompanied me to grow up scientifically and humanly. It is my honor and pleasure to work and live with all of you.

I would like to express my sincere gratitude to Alain Sacuto for welcome in his research group and Maximilien Cazayous for their supervision and guidance. Maximilien is very experienced in guiding thesis and has profound knowledge in condensed matter physics and experimental technologies. The same time, he has excellent personal character : never give up spirit, rigorous and optimism. All these give me a very good environment to chase my dream.

I would like to thank other faculties of SQUAP group, Yann Gallais and Marie-Aude Méasson for their scientific discussions, assistance in experiment and suggestion during my thesis.

I also would like to express my gratitude to the people who I have collaborated with in my thesis. Without their assistances and contribution, it was impossible for me to finish in two years. First of all, I want to thank Agnès Barthélémy and Manuel Bibes of Unite Mixte de Physique CNRS/Thales and Université Paris-Sud for the synthesis of high quality BiFeO_3 thin films on different substrates. With these samples, we observed clear signals at frequency which have been difficult to obtain. I also would like to thank L. Bellaiche, D. Rahmedov of University of Arkansas for the effective Hamiltonian calculation and A. K. Zvezdin of Moscow Institute of Physics and Technology State University for the Landau-Ginzburg theory on BiFeO_3 thin films and J.-M. Le Breton, J. Juraszek of Université de Rouen for the Mössbauer measurements of BiFeO_3 thin films. Moreover, I would like to thank S. W. Cheong of Rutgers University for providing YbMnO_3 and HoMnO_3 single crystal samples and L. Pinsard of Laboratoire de Chimie des Solides in Paris-Sud University for the synthesis of YMnO_3 single crystal.

I want to express my sincere thank to Ricardo Lobo and Yves Dumont for accepting to be the referees of my thesis. I would also like to thank Dorothee Colson and Virigine Simonet as the committee members of thesis defense. I also want to thank the director of MPQ lab Carlo Sirtori for accepting me and the director of Doctor school Thomas Coudreau for his suggestion and informations. I also would like to thank Anne Servouze, the secretary of the lab, she was always there to solve my problems.

Furthermore, I want to thank other members (some of them are already graduated) of SQUAP group : Pauline Rovillain, Ludivine Chauviere, Sébastien Blanc, Jonathan Buhot, Constance Toulouse, Siham Benhabib, Elisa Riccardi, Yanqing Yang and Pierre

Massat. Thank you for the wonderful memory with your accompany.

I also want to thank all the PhD students and postdocs in 645B room : Alexandre Baksic, Loïc Freton, Alexandre Leboite, Luc Nguyen-the, Philippe Petit, Peng Yang, Juan Restrepo, H el ene Prunier, Motoali Bamba and Yuk-Nga Chen et al. I have troubled you so much but all of you are so patient and nice. Thank you for your help.

Moreover, I would like to express my gratitude to my friends in Ecole Normale Sup erieure of Paris and five-stars basketball club : Junjun Li, Yun Li, Megan, Zhitao Han, Fan Zhang, Xin Li, Jie Hu, JianHua TIAN, Xiongtu ZHOU, Kevin, Ding Yu, Haiyang Wang, Zidi Liu, Yuanjing Xiao, Xin Liu, Guangfei Feng et al. We had so many memorable activities.

Finally, I want to express my sincere gratitude to my mom Lihua, my dad Guoqiang and my wife Rongzi. You are my most valuable treasures. Thanks for your support and encourages which are the most important motivation for me to pursuit my career and dreams.

Thanks all the people who accompany me through the three years.

Résumé

Les multiferroïques présentent la rare propriété de posséder simultanément un ordre magnétique et un ordre ferroélectrique qui interagissent via le couplage magnétoélectrique. Ces caractéristiques font ressortir de nouveaux phénomènes physiques et offrent des possibilités de nouvelles fonctionnalités en vue d'applications. Dans ce travail, nous avons étudié les excitations de spin et réseau dans les composés $RMnO_3$ hexagonaux ($R = Yb, Y, Ho$) et dans les films minces $BiFeO_3$.

Nos mesures de $RMnO_3$ hexagonaux mettent en évidence le couplage entre les excitations du réseau et les excitations magnétiques. En outre, les résultats montrent clairement que les interactions inter-plan le long de l'axe c entre $R-Mn$ et $R-R$ sont importantes pour l'établissement de la structure magnétique de ces composés.

Dans les films minces $BiFeO_3$, nous avons observé la présence de la cycloïde de spin dans les échantillons faiblement contraints et la disparition de cette dernière à plus forte contrainte. Dans l'état de faible contrainte, une nouvelle structure de spin cycloïdale avec un vecteur d'onde de propagation le long de $[110]$ est prédit et observé expérimentalement. Nos résultats sont comparés avec succès à des mesures Mössbauer et à des calculs théoriques. Ces résultats ont des implications profondes pour la mise en œuvre des films de $BiFeO_3$ dans les futurs dispositifs magnoniques et spintroniques.

Abstract

Multiferroic materials present the rare properties that simultaneously exist magnetic and ferroelectric orders and interaction between them. These features in multiferroics bring out novel physical phenomena and offer possibilities for new device functions. BiFeO_3 and hexagonal RMnO_3 are two most investigated multiferroics. In this work, we have studied the lattice and spin excitations in hexagonal RMnO_3 single crystals ($\text{R}=\text{Yb}, \text{Y}, \text{Ho}$) and BiFeO_3 thin films on different substrates.

Our measurements of hexagonal RMnO_3 single crystals indicate the coupling of lattice and spin excitations. Moreover, the results clearly show that the R-Mn and R-R interplane interactions along c-axis also play an important role in the magnetic phase transitions of h- RMnO_3 .

In the case of BiFeO_3 thin films, we have observed that high epitaxial strain can destroy the bulk-like cycloidal modulation and the non-collinear orders are stable at low strain. A mixture phase of two magnetic orders is also detected in BiFeO_3 thin films. In the lower-strain state, a new cycloidal spin structure with a propagation wavevector along $[110]$ is predicted and experimentally observed. Our findings have profound implications for the implementation of BiFeO_3 films in magnonic and spintronic devices. Indeed, our Raman scattering measurements reveal that strain can completely quench high energy magnon modes, offering exciting possibilities for BiFeO_3 -based magnonic devices.

Table des matières

Introduction	1
1 The multiferroic	3
1.1 The Motivation	3
1.2 The ferroic properties	6
1.2.1 The ferroelectricity	6
1.2.1.1 Definition	6
1.2.1.2 Theories of ferroelectricity	8
1.2.1.3 Phase transition	8
1.2.2 The Magnetism	12
1.2.2.1 The Paramagnetic	13
1.2.2.2 The Ferromagnetic	13
1.2.2.3 Antiferromagnetic	14
1.2.2.4 The magnon	16
1.2.3 The magnetoelectric effect	17
1.3 The type I multiferroics	18
1.3.1 Perovskites Multiferroic	18
1.3.2 Ferroelectricity due to charge ordering	19
1.3.3 Ferroelectricity due to lone pairs	20
1.3.4 “Geometric” ferroelectricity	20
1.4 The type I multiferroic : BiFeO ₃	20
1.4.1 Bulk BiFeO ₃	20
1.4.1.1 Structure	20
1.4.1.2 Ferroelectricity	22
1.4.1.3 Magnetic properties	22
1.4.1.4 Magnetoelectric coupling	24
1.4.1.5 Spin modes	25
1.4.2 Thin film BiFeO ₃	29
1.4.2.1 Structure	29
1.4.2.2 Ferroelectric properties	31
1.4.2.3 Magnetic properties	32
1.4.2.4 Magnetoelectric coupling	33
1.5 The type I multiferroic : Hexagonal RMnO ₃	34
1.5.1 Structure	35

1.5.2	Ferroelectricity properties	36
1.5.3	Magnetic structure	36
1.5.4	Spin-lattice coupling	38
1.6	The type II multiferroics	40
1.6.1	Magnetism	41
1.6.2	Ferroelectric induced by the spiral spin order	42
1.6.3	Ferroelectric induced by E-type antiferromagnet	43
2	Raman light scattering and samples	45
2.1	The principle	45
2.2	The macroscopic theory of scattering by phonon	46
2.3	Raman tensors and selection rules	48
2.4	The microscopic theory of scattering by phonon	49
2.5	The theory of scattering by magnon	52
2.5.1	The scattering by ferromagnets	52
2.5.2	The scattering by antiferromagnets	54
2.6	The optical path	55
2.7	Spectrometer	56
2.8	The sample chamber	58
2.8.1	The temperature measurements	58
2.8.2	The measurements in magnetic field	60
2.9	The samples	61
2.9.1	BiFeO ₃ thin film	61
2.9.2	Hexagonal RMnO ₃	61
3	Hexagonal RMnO₃ : Lattice and magnetic excitations	63
3.1	Crystal structure	63
3.2	Magnetic structure	66
3.3	Hexagonal YbMnO ₃	67
3.3.1	Lattice excitations	67
3.3.2	Magnetic excitations	70
3.3.3	Conclusion	74
3.4	YMnO ₃	75
3.4.1	Lattice excitations	75
3.4.2	Magnetic excitations	78
3.4.3	Conclusion	82
3.5	HoMnO ₃	82
3.5.1	Lattice excitations	82
3.5.2	Magnetic excitations	85
3.5.3	Conclusion	87
3.6	Conclusion	88

4	Magnetic excitations in BiFeO₃ thin films	89
4.1	Raman spectroscopy of BiFeO ₃ thin films	89
4.1.1	Magnetic excitations in BiFeO ₃ single crystal	89
4.1.2	Strain effect on thin film	90
4.1.3	Spin excitations in BiFeO ₃ thin film	90
4.2	Mössbauer measurements of BiFeO ₃ thin film	95
4.2.1	Mössbauer spectroscopy	95
4.2.2	Mössbauer spectra of BiFeO ₃ thin films	97
4.2.3	Landau-Ginzburg theory	101
4.3	Raman measurements under magnetic field	104
4.4	Conclusion	106
	Conclusion and perspectives	107
	Bibliographie	111

Introduction

One of the very promising approaches to create novel materials is to combine different physical properties in one material to achieve rich functionalities. Electricity and magnetism were combined into one common discipline in the 19th century by Maxwell equations. Nonetheless electric and magnetic ordering in solids is most often considered separately and usually with good reasons : the electric charges of electrons are responsible for the electricity, whereas electron spins govern magnetic properties. However, there are some cases in which these two orders coupled strongly. For example, in the field of spintronics, the effects of spins on the transport properties of solids (and vice versa) allow the possibility to control one by the other. Another case is the finding of a strong coupling of magnetic and electric fields in insulators which can be traced back to Pierre Curie(Curie, 1894). Schmid (Schmid, 1994) first introduced the term “multiferroic” to name this type of materials. In multiferroics, there are several different ferroic orders : ferroelectric (polarization), ferroelastic (deformation) or ferromagnetic (magnetization). The coupling of these orders in multiferroics is presented in Fig. 1.

Such multiferroics were studied to some degree in the 1960s and 1970s,(Dzyaloshinskii, 1959; Astrov, 1960; Ascher et al., 1966) but then languished, in large part because single-phase materials with both properties could not be widely produced. However three events revived the study of multiferroics. The first one was the theoretical research of multiferroics origin. In the first year of 21st century, Nicola A. Hill published an important study, in which she detailedly addressed the question : why are there so few magnetic ferroelectrics?(Hill, 2000) They found out that the transition metal d electrons, which are essential for magnetism, reduce the tendency for off-center ferroelectric distortion. The other two events were experimental achievements that identified two distinct classes of multiferroics which bypass the problem issued in Hill’s paper. In 2003, Ramesh’s group successfully grew thin films of one of the most popular multiferroics, BiFeO₃ which is called type-I multiferroics(Wang et al., 2003). The multiferroic properties of bulk BiFeO₃ were fairly weak at that time, but the properties of BiFeO₃ thin-film are greatly enhanced. Also in 2003, the phenomenon that magnetism causes ferroelectricity was discovered in TbMnO₃ by Tokura and Kimura defining a new class the type-II multiferroics(Kimura et al., 2003a), and Cheong et al. found a similar effect in TbMn₂O₅ (Hur et al., 2004). The detail of these two types multiferroics will be discussed in chapter 1. Later, giant magneo-elastic coupling was found in hexagonal manganites such as HoMnO₃ (Lee et al., 2008). The realization that these materials have great potential for practical applications has lead to an extremely rapid develop-

ment of multiferroics.

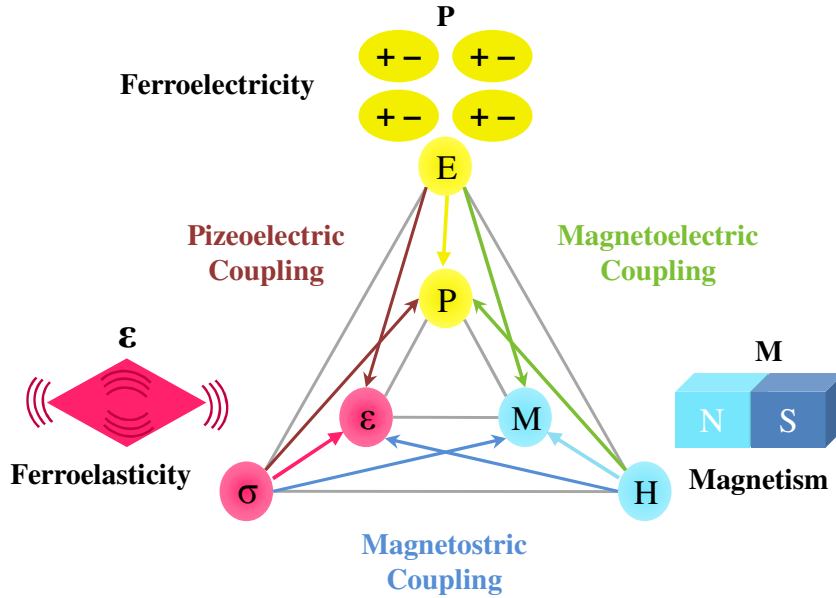


FIGURE 1: The electric field E , magnetic field H , and stress σ control the electric polarization P , magnetization M , and strain ϵ , respectively. In a ferroic material, P , M , or ϵ are spontaneously formed to produce ferromagnetism, ferroelectricity, or ferroelasticity, respectively. In a multiferroic, the coexistence of at least two ferroic forms of ordering leads to additional interactions. In a magnetoelectric multiferroic, a magnetic field may control P or an electric field may control M . (Spaldin & Fiebig, 2005)

In this work, we measure the spin and lattice excitations in hexagonal RMnO_3 single crystals and BiFeO_3 thin films by optical methods. In the first chapter, after recalling application of multiferroics and the ferroelectric and magnetic properties, I set up a review of the main theoretical and experimental results obtained on multiferroics, specially on BiFeO_3 and hexagonal RMnO_3 . Chapter 2 explains the experimental techniques used in this work : Raman scattering and describes the experimental setups. The chapter 3 is devoted to experimental results of hexagonal RMnO_3 single crystals and the investigation of the coupling of lattice and spin excitations. The results clearly show that the R-Mn and R-R interplane interaction along the c -axis also play an important role in the magnetic structure of $h\text{-RMnO}_3$. In chapter 4, we show the experimental results of BiFeO_3 thin films and found out that non-collinear orders are stable at low strain. High epitaxial strain can destroy the bulk-like cycloidal modulation. Our findings have profound implications for the implementation of BiFeO_3 films in magnonic and spintronic devices.

Chapitre 1

The multiferroic

Multiferroics, defined as the multifunctional materials in which two or more kinds of fundamental ferroicities coexist, have become one of the hot topics of condensed matter physics and material science in recent years. The coexistence of several order parameters in multiferroics brings out novel physical phenomena and offer possibilities for new device functions (Fiebig, 2005). To understand the basic phenomena and appreciate the main achievements in this field, we can classify multiferroics by the microscopic mechanism that determines their properties. Generally speaking, there are two groups of multiferroics. (Khomskii, 2009) The first group, called type-I multiferroics, contains those materials in which ferroelectricity and magnetism have different origins and appear largely independently of one another, though there is some coupling between them. The second group, called type-II multiferroics, is relatively recently discovered materials, in which magnetism cause ferroelectricity, implying a strong coupling between them. However, the polarization in these materials is usually much smaller. In this chapter, firstly we will discuss the motivation of our work and the microscopic mechanism of magnetism and ferroelectricity in these materials. Then we will analyze the two types of multiferroics, especially BiFeO_3 and hexagonal RMnO_3 compounds.

1.1 The Motivation

There are two main motivations for the research of multiferroic materials. The first one is the plenty and representative physics phenomena and mechanisms involved in these materials, such as polarization induced by magnetic order. The other motivation is the possible applications in the industry. The main promising applications include magnetic sensors and magnetoelectric (ME) memory. I am presenting the motivation below.

Magnetic sensors

The simple and direct application of multiferroics is magnetic sensors. In magnetic sensors, the ferroelectric polarization can be controlled by a magnetic field as shown in Fig. 1.1 a, which has been demonstrated in several multiferroic materials such as

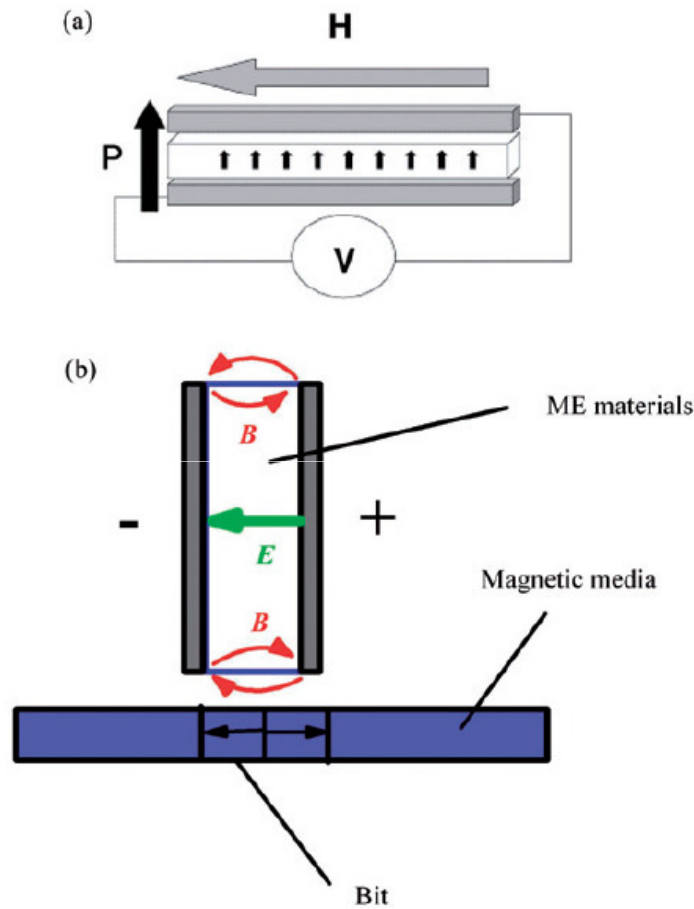


FIGURE 1.1: **a.** Multiferroic materials as a probe of the magnetic field. The middle layer (the white layer) is multiferroic, and the upper and lower layers (grey layers) are ferromagnetic metals. An external magnetic field will induce the electric polarization perpendicular to the magnetic field direction, and then a voltage. **b.** The read-head device using the probe in **a.** The blue layer is the magnetic media (magnetic disk) and the black arrows in it indicate two opposite bits.(Wang et al. 2009)

TbMnO_3 and TbMn_2O_5 . (Kimura et al., 2003a; Hur et al., 2004) The typical model of multiferroics magnetic sensors is the read head of memory device as shown in Fig. 1.1 b. Highly sensitive magnetic field sensors can be created using multiferroics with high ME coefficient.

Magnetoelectric memory

As ferroelectric polarization and magnetization are used to encode binary information in FeRAM (ferroelectric random access memories) and MRAMs(magnetic random access memories) respectively, the coexistence of magnetization and polarization in multiferroic materials allow the realization of four-state logic in a single device.(Gajek et al., 2007) Theoretically, more complex schemes have been proposed in order to store

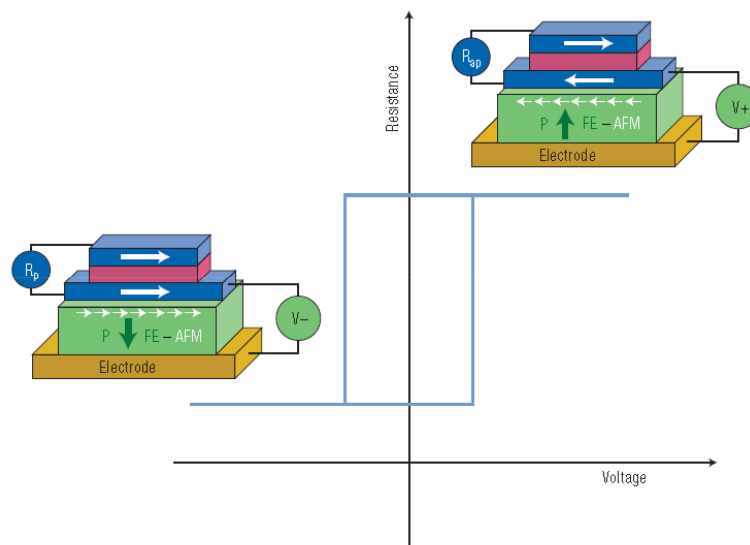


FIGURE 1.2: **a.** Multiferroic materials as a probe of the magnetic field. The middle layer (the white layer) is multiferroic, and the upper and lower layers (grey layers) are ferromagnetic metals. An external magnetic field will induce the electric polarization perpendicular to the magnetic field direction, and then a voltage. **b.** The read-head device using the probe in (a). The blue layer is the magnetic media (magnetic disk) and the black arrows in it indicate two opposite bits.(Bibes & Barthelemy, 2008)

up to eight logic states.(Yang et al., 2007)

Beyond the combination of the ferroic properties in a single device, the electric control of magnetization via the ME coupling offers the opportunity of combining the respective advantages of FeRAMs and MRAMs in the form of non-volatile magnetic storage bits that are switched by an electric field, called magnetoelectric random access memories (MERAM). These devices could drastically reduce the writing energy of MRAMs. The basic operation of MERAM combines the ME coupling with interface exchange, between a multiferroic and a ferromagnet, to switch the magnetization of ferromagnet layer by using a voltage as shown in Fig. 1.2.(Bibes & Barthelemy, 2008) In MERAMs, ME coupling enables an electric field to control the exchange coupling at the interface of the multiferroic with ferromagnet. The exchange coupling across the interface then controls the magnetization of the ferromagnetic layer, so that ultimately this magnetization can be switched by the electric polarization of the multiferroic. This triggered much attention in the research for the exchange bias using multiferroics. (Bea et al., 2008; Laukhin et al., 2006; Binek & Doudin, 2005)

In 2010, Wu et al. demonstrate electrical control of exchange bias using a field-effect device employing multiferroic (ferroelectric/antiferromagnetic) BiFeO_3 as the dielectric and ferromagnetic $\text{La}_{0.7}\text{Sr}_{0.3}\text{MnO}_3$ (LSMO) as the conducting channel, therefore they can reversibly switch between two distinct exchange-bias states by switching the ferro-

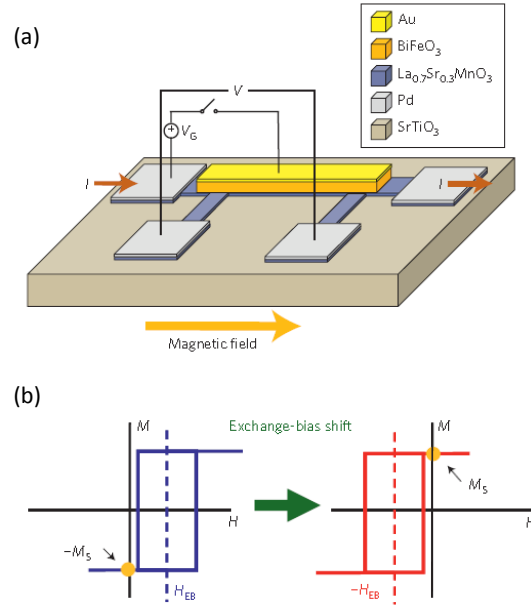


FIGURE 1.3: **a.** A schematic of the BFO/LSMO field-effect device. To change the BFO polarization, a voltage pulse V_G is applied between the gate and the LSMO channel (b) An example of how magnetization switching might occur in a system with reversible switching of exchange bias. Initially the magnetic layer is in the $-M_S$ state with positive exchange bias. When switched to negative exchange bias, the magnetization switches to $+M_S$. (Wu et al., 2010)

lectric polarization of BiFeO_3 . Figure 1.3 a and b shows the scheme of BFO/LSMO field-effect device and the reversible switching of exchange bias. (Wu et al., 2010)

In conclusion, although many issues remain to be resolved, the impact of multiferroics application is tremendous. Therefore, the involved physics mechanism and excellent application potential make the multiferroics one of the hot research topics in Physics.

1.2 The ferroic properties

1.2.1 The ferroelectricity

1.2.1.1 Definition

Ferroelectricity is characterized by a spontaneous polarization in the absence of an external electric field. The spontaneous polarization can be switched by applying an external electric field. Ferroelectric materials undergo a structural phase transition from a paraelectric phase to a ferroelectric phase upon cooling through the Curie temperature, T_C . Above T_C , the crystal has a centrosymmetric structure and has no spontaneous polarization. Below T_C , the crystal exhibits ferroelectricity and has a structure resulting from a change in the symmetry of the unit cell.

When an external field is applied in a direction opposite to the polarization, the polarization can be reoriented in the direction of the electric field. This process is reversible and is called polarization switching. When the polarization is parallel to applied electric field, the switching is done. However, it is not necessary that the polarization is exactly reoriented along the electric field direction. The net polarization of an initially unpolarized ferroelectric material is small. The polarization switching can be observed by measuring the displacement current that flows while the applied electric field is scanned. The charge associated to the polarization as a function of the applied electric field can be calculated by integrating the displacement current. The polarization-electric field hysteresis loop obtained in this way is an important characteristic of a ferroelectric. (Setter et al., 2006) Figure 1.4 shows a typical hysteresis loop from which the values of the remnant polarization P and coercive electric field E_C can be determined.

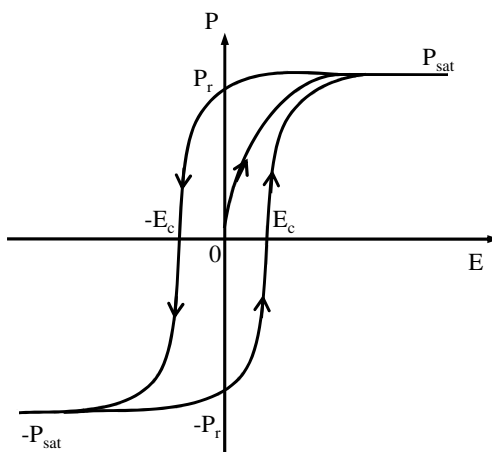


FIGURE 1.4: Ferroelectric hysteresis loop showing the evolution of the polarization P as a function of the applied electric field E . P_r is the remanent polarization, P_{sat} is the saturation polarization.

As shown in Fig. 1.4, when an electric field is applied at the beginning, there is a linear relationship between the polarization and the applied electric field. In this case, there is no polarization switching. As the electric field increases, however, domains in which the direction of spontaneous polarization is opposite to electric field begin to switch to a more energetically favorable direction. The switching process continues until all of the domains are aligned along electric field direction. When the field returns to zero, the polarization does not return back to the initial value. The amount of switchable polarization after removal of an electric field is called the remnant polarization, P_r . The strength of the electric field to switch the opposite polarization domain is called the coercive electric field, E_c . This process can be repeated. The spontaneous polarization results in the breaking of the space reversal symmetry ($x \rightarrow -x$): $\mathbf{P} \rightarrow -\mathbf{P}$ and $\mathbf{M} \rightarrow \mathbf{M}$. (\mathbf{M} is magnetization)

1.2.1.2 Theories of ferroelectricity

Any lattice of oppositely signed point charges is inherently unstable. Ionic materials are stable because of short-range repulsions between adjacent electron clouds. The existence or absence of ferroelectricity is determined by a balance between these short-range repulsion, which favor the nonferroelectric symmetric structure, and additional bonding considerations, which may stabilize the ferroelectric phase. Even in ferroelectric materials, the short-range repulsions dominate at high temperature, resulting in the symmetric, unpolarized state. As the temperature is decreased, the stabilizing forces associated with the polarization of the ions as they are displaced become stronger than the short-range repulsive ion-ion interactions, and the polarization state becomes stable, even in the absence of an applied field.

The ferroelectrics can be classified into two categories according to the main driving force of phase transition. The first driving force for the ferroelectric transitions comes from the structural instability toward the polar state associated with electronic pairing. The typical materials are BiFeO_3 and BiMnO_3 . The second driving force is complex lattice distortion. The typical materials are Hexagonal manganites RMnO_3 with R the rare earth elements (Ho-Lu or Y).

1.2.1.3 Phase transition

Landau symmetry-based treatment of phase transitions was first applied to the case of ferroelectrics by Devonshire. (Landau & Lifshitz, 1969; Devonshire, 1949, 1954) The free energy, F , in the vicinity of the transition can be generally expanded as a power series of the order parameter. The coefficients can be fitted to experiments or gleaned from microscopic calculations. Moreover we ignore the strain field and choose the origin of energy for the free unpolarized crystal to be zero, hence the free energy equation is

$$F(P) = \frac{a}{2}P^2 + \frac{b}{4}P^4 + \frac{c}{6}P^6 - \mathbf{E} \cdot \mathbf{P} \quad (1.1)$$

The equilibrium configuration is determined by finding the minima of F , $\mathbf{E} \cdot \mathbf{P}$ is the contribution to the free energy under external electric field \mathbf{E} .

$$\frac{\partial F}{\partial P} = 0 \quad (1.2)$$

This equation gives us an expression for the electric field E as a function of the polarization

$$E = aP + bP^3 + cP^5 \quad (1.3)$$

Then we can determine the linear dielectric susceptibility above the transition by differential this equation with respect to P and then setting $P=0$ to obtain

$$\chi = \left. \frac{\partial P}{\partial E} \right|_{E=0} = \left. \frac{\partial E}{\partial P} \right|_{P=0} = \frac{1}{\alpha} \quad (1.4)$$

In the Landau-Devonshire theory, it is assumed that around the Curie point

$$a = a_0(T - T_C) \quad (1.5)$$

The other coefficients in the free-energy expansion are independent of the temperature. According to the last two equations, we find an expression for the dielectric stiffness

$$K = \frac{1}{\chi} = a_0(T - T_C) \quad (1.6)$$

which captures the Curie-Weiss behavior observed in most ferroelectrics for $T > T_C$. If we include the linear temperature dependence of a , we have the general expression for the free energy

$$F(P) = \frac{a_0}{2}(T - T_C)P^2 + \frac{b}{4}P^4 + \frac{c}{6}P^6 - EP \quad (1.7)$$

where a_0 and c are both positive in all known ferroelectrics. How this free energy transforms between the paraelectric and the ferroelectric phase will be determined by the sign of the coefficient b . Its sign will determine the nature of the paraelectric-ferroelectric transition.

The second-order phase transition

In the case of $b > 0$, then a second-order transition occurs at $T = T_C$. When temperature decreases from above T_C to below T_C , the lowest free energy will evolve from the first scheme ($P=0$) to the second ($P=P_S$) as shown in Fig. 1.5 a. . The spontaneous polarization can be estimated by setting external electric field $E=0$ giving :

$$P_0 = \left[\frac{a_0}{b}(T - T_C) \right]^{\frac{1}{2}} \quad (1.8)$$

In Fig. 1.5 b. , we see that the spontaneous polarization P_S will increase with decreasing temperature from T_C . We note that if we determine the dielectric stiffness below the transition then we find

$$K = \frac{1}{\chi} = 2a_0(T - T_C) \quad (1.9)$$

The evolution of K and P_S as a function of temperature is presented in Fig. 1.5 b. and c respectively.

The first-order phase transition

In the case of $b < 0$, which is the first-order phase transition, Fig. 1.6 a shows the shape of the free energy at different temperatures. There are three characteristic tem-

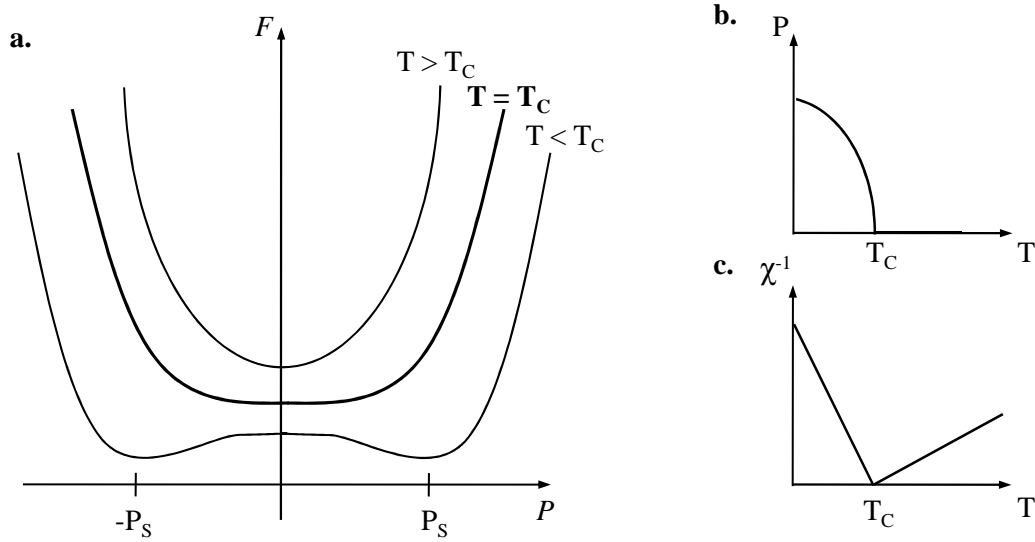


FIGURE 1.5: **a.** Evolution of the free energy of the system as a function of the temperature in second order phase transition. Evolution of **b.** polarization and **c.** the dielectric stiffness in function of the temperature.

peratures T_1 , T_2 and T_C . For $T > T_2$, the curve $F(P)$ has only one minimum $P = 0$, which means that above this temperature no spontaneous polarization can exist. For $T_2 > T > T_1$, the curve $F(P)$ has two minima $P = P_S$.

Above T_C , the energy of these two minima is greater than the minimum at $P = 0$, so they are metastable states. Below T_C , the local minimum at $P = 0$ becomes metastable. At T_C , the three local minima have the same energy. For $T < T_1$, there are only two minima at $P = P_S$ which are the equilibrium positions. The material then develops a spontaneous polarization P_S . The most important feature of this phase transition is that the order parameter jumps discontinuously to zero at T_C . This type of phase transition is usually found in solid-liquid transitions.

Soft mode

The soft mode of ferroelectric transition is a phonon mode. In the second-phase transitions the phonon mode is polar, that is to say associated with atomic vibrations in the direction of the spontaneous polarization. This type of transition is governed by one or more polar phonons with a soft mode behavior. The soft mode was first predicted in BaTiO_3 . (Spitzer et al., 1962) This is the transverse optical phonon mode of lowest energy whose frequency tends to zero in the phase transition temperature. Its eigenvectors correspond to displacements of the atoms oscillating out of position centrosymmetric. Below the transition temperature, the atoms deviate more from their centrosymmetric position and begin to oscillate around their new equilibrium position. Then, the crystal becomes ferroelectric. (Scott, 1974) In the new structure, there are one or two soft phonon modes whose frequency increases when the temperature decreases. Figure 1.7 shows the temperature evolution of the frequency of the soft mode in the

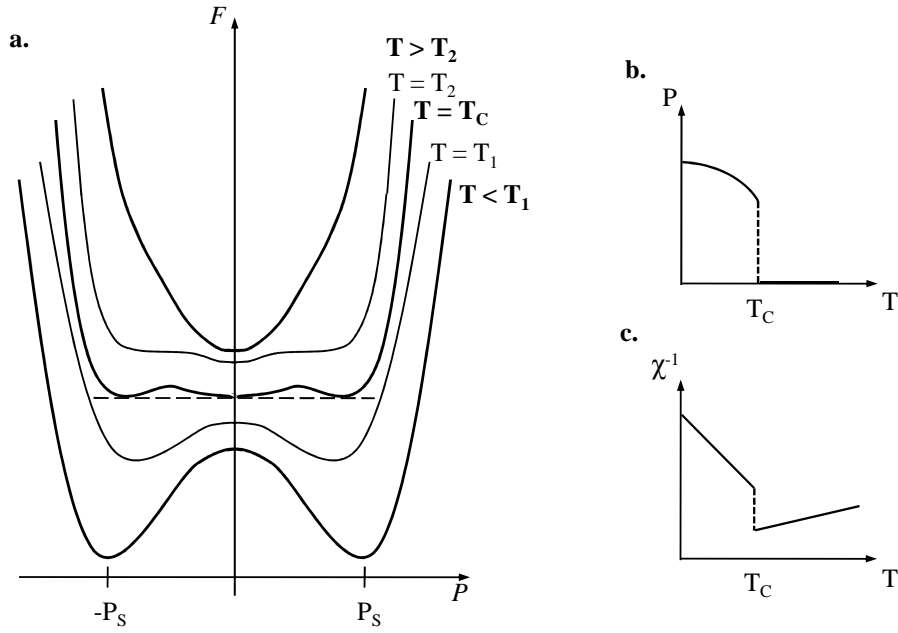


FIGURE 1.6: **a.** Evolution of the free energy of the system as a function of the temperature in first order phase transition. Evolution of **b.** polarization and **c.** of the inverse of the dielectric stiffness as a function of the temperature.

paraelectric phase of SrTiO_3 with a ferroelectric phase transition around 105 K. (Pytte & Feder, 1969) This figure clearly shows that the frequency of three-dimensional phonon mode in the paraelectric phase decreases down to T_c . Below T_c , this mode is split into two modes soft, a two dimensional mode and a one-dimensional mode and their frequencies increase as the temperature decreases in the ferroelectric phase.

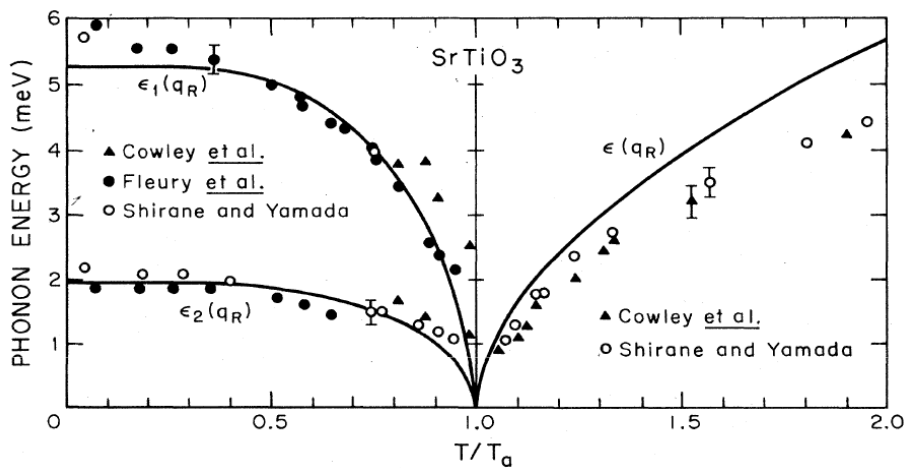


FIGURE 1.7: Mode frequencies soft phonon in function of the temperature before and after the structural phase transition, paraelectric-ferroelectric SrTiO_3 . The temperature was normalized to the transition temperature $T_a = 105$ K. (Pytte & Feder, 1969)

1.2.2 The Magnetism

When a magnetic field, H , is applied to a material, the response of the material is called magnetic induction, B . The relationship between B and H is a property of the material. The equation involving B and H is

$$B = H + 4\pi M \quad (1.10)$$

where M is the magnetization of the medium which depends on both the individual magnetic moments of the constituent ions, atoms, or molecules, and how these dipole moments interact with each other. The linear regime of M to H ratio is called the susceptibility :

$$\chi = \frac{M}{H} \quad (1.11)$$

The susceptibility indicates how a material responds to an applied magnetic field. The ratio of B to H is called the permeability :

$$\mu = \frac{B}{H} \quad (1.12)$$

It indicates how permeable the material is to the magnetic field.

Graphs of M or B versus H are called magnetization curves, and are characteristic of the type of material. According to the M - H curves, there are four main classes of magnetic material : the para-, antiferro-, ferro-, and ferrimagnets. The spin directions are shown in Fig. 1.8.

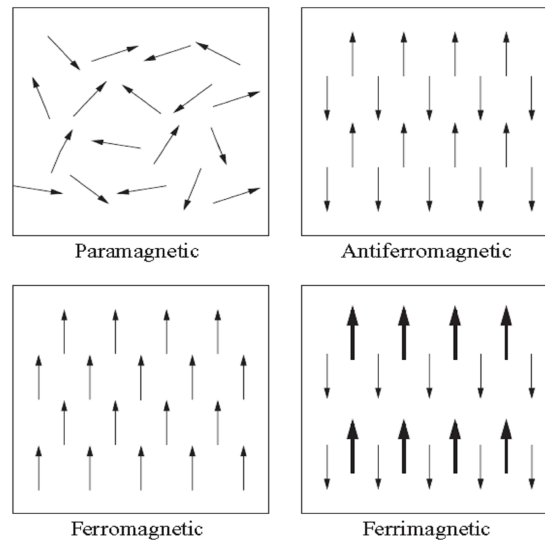


FIGURE 1.8: Spin orders in para-, antiferro-, ferro-, and ferrimagnets.

1.2.2.1 The Paramagnetic

In paramagnets, the individual atoms or ions have magnetic moments, but these moments are disordered, so that there is no net magnetization. The susceptibility is positive, because the external field causes the moments to partially align with it, and it is small, because the thermal energy which tends to disorder the moments is large compared to the magnetic energy that tends to align them along the field direction. The susceptibility of many paramagnetic materials obey to the Curie-Weiss theory :

$$\chi = \frac{M}{H} = \frac{C}{T - \theta} \quad (1.13)$$

where C is a constant. Paramagnets become ordered below the Curie temperature, T_C .

1.2.2.2 The Ferromagnetic

A ferromagnetic material undergoes a phase transition from a high-temperature phase that does not have a macroscopic magnetic moment to a low-temperature phase that has a spontaneous magnetization below Curie temperature even in the absence of an applied magnetic field. The macroscopic magnetization is caused by the magnetic dipole moments of the atoms tending to line up in the same direction. The susceptibility can be very large and is often hysteretic because the magnetization process proceeds via domain-wall motion. The microscopic mechanism of the line-up of moments is the exchange interaction.

Exchange interaction

The quantum mechanism exchange energy, J , between two electrons is formally defined as twice the energy difference between their symmetric and antisymmetric two-body wavefunctions :

$$J = \langle \phi_1(r_1)\phi_2(r_2) | H_{12} | \phi_1(r_2)\phi_2(r_1) \rangle \quad (1.14)$$

where r_1 and r_2 describe the positions of the two electrons, each of which may occupy orbitals ϕ_1 and ϕ_2 . H_{12} is the Hamiltonian operator of interaction between the two electrons. When J is positive, which is always the case when the electron-electron interaction is the usual coulomb repulsion, the exchange energy favor electrons with parallel spins and causes ferromagnetism.

In a crystal, the generalization of the Heisenberg Hamiltonian in which the sum is taken over the exchange Hamiltonians for all the (i,j) pairs of atoms of the many-electron system gives :

$$\mathcal{H} = - \sum_J JS_i \cdot S_j \quad (1.15)$$

1.2.2.3 Antiferromagnetic

In antiferromagnets, the magnetic moments on the individual atoms or ions align in an antiparallel fashion so as to cancel each other out. There is no net zero-field magnetization and a small positive susceptibility. There are several types of antiferromagnetic structures and some are shown in Fig. 1.9 .

Generally, antiferromagnetic order may exist at sufficiently low temperatures, vanishing at and above Néel temperature. Above the Néel temperature, the material is typically paramagnetic. The reason of antiparallel alignment of the moments is the superexchange interaction. Notice that (anti)ferromagnetic order leads to the breaking of time reversal symmetry. ($t \rightarrow -t$) : $\mathbf{P} \rightarrow \mathbf{P}$ and $\mathbf{M} \rightarrow -\mathbf{M}$.

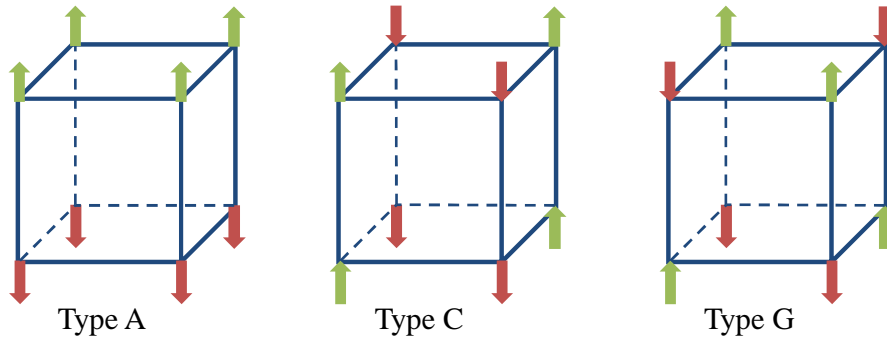


FIGURE 1.9: The three different types of antiferromagnetic structures.

Superexchange interaction

The superexchange interaction is an antiferromagnetic or ferromagnetic coupling between two next-to-nearest neighbor cations through a non-magnetic anion. In this way, it differs from direct exchange in which there is coupling between nearest neighbor cations not involving an intermediary anion. Superexchange was proposed by Hendrik Kramers in 1934 when he noticed that in crystals like MnO, Mn atoms interact with one another despite having nonmagnetic oxygen atoms between them (Fig. 1.10). (Kramers, 1934) Phillip Anderson later refined Kramers' model in 1950 (Anderson, 1950) Therefore, we use MnO as our example. The O^{2-} ion has an occupied p orbital oriented along the Mn-O-Mn axis. Each Mn^{2+} ion contains five 3d electrons, which occupy the 3d orbitals with one electron per orbital and their spins parallel. The p orbitals from oxygen and d orbitals from manganese can form a direct exchange. There is antiferromagnetic order because the singlet state is energetically favoured. This configuration allows a delocalization of the involved electrons due to a lowering of the kinetic energy as shown in Fig. 1.10.

Here we evaluate the magnitude of effective interaction between two Mn^{2+} . We introduce two parameters : (i) the energy matrix element t for shifting p-electron to one Mn^{2+} and (ii) the increase of energy ($= \xi$) for the shift of p-electron to Mn^{2+} . Then the probability of the above process is evaluated as $(t/\xi)^2$. The resultant exchange

energy is $J(t/\xi)^2$. The same thing happens for the case when one of the p electrons from the O^{2-} hops over to the other Mn^{2+} ions. So the resultant exchange energy is given by $2 J(t/\xi)^2$. S_1 and S_2 are spins of Mn^{2+} ions, the superexchange is given by $E_{ex} = -2J'S_1 \cdot S_2$, where $J' = J(t/\xi S)^2$. When $J' < 0$, S_1 and S_2 are antiparallel, favoring the antiferromagnetic spin arrangement. (Anderson, 1950)

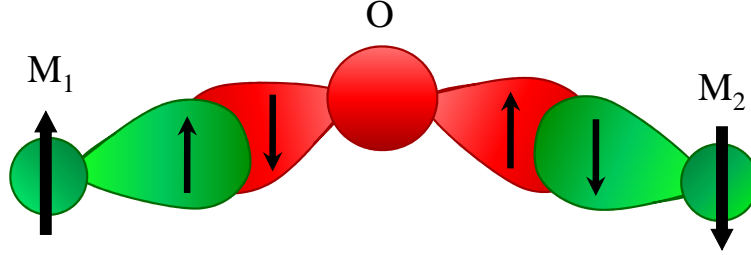


FIGURE 1.10: The orbital configuration of magnetic atoms (M_1 and M_2) and oxygen by superexchange interaction.

Dzyaloshinskii-Moriya interaction

The Dzyaloshinskii-Moriya interaction is a relativistic correction of the superexchange. Dzyaloshinskii-Moriya theory (DM) was developed to explain the low magnetic moment in the antiferromagnetic compound Fe_2O_3 . (Moriya, 1960; Dzyaloshinsky, 1958) In 1958, I. E. Dzyaloshinskii shows that the symmetry of the system remains the same if the spins are collinear and parallel to the axis of symmetry. If the spins are not collinear there is a ferromagnetic component. Then an interaction term antisymmetric is introduced into the free energy :

$$\mathbf{D} \cdot (\mathbf{S}_1 \times \mathbf{S}_2) \quad (1.16)$$

where D is the Dzyaloshinskii-Moriya vector and S_1 and S_2 are spins of M_1 and M_2 , a canting of the spins is favored giving birth to a low ferromagnetic moment. In 1960, T. Moriya developed a microscopic theory of this interaction. It showed that this interaction is due to the spin-orbit coupling which adds a antisymmetric component. In addition, T. Moriya shows that in the system of two magnetic atoms M_1 (S_1) and M_2 (S_2), when the middle of (M_1 , M_2) is not the system inversion center, D will not be zero. Thus, D is dependent on the position of the ion O . The DM interaction is connected to the symmetry of the system and promotes non-collinear alignment of the magnetic moments as shown in Fig. 1.11

Geometrical frustration

Geometrical frustration is an important feature in antiferromagnets, where it stems from the topological arrangement of spins. A simple 2D example is shown in Fig. 1.12. Three magnetic ions reside on the corners of a triangle with antiferromagnetic interactions between them—the energy is minimized when each spin is aligned opposite to

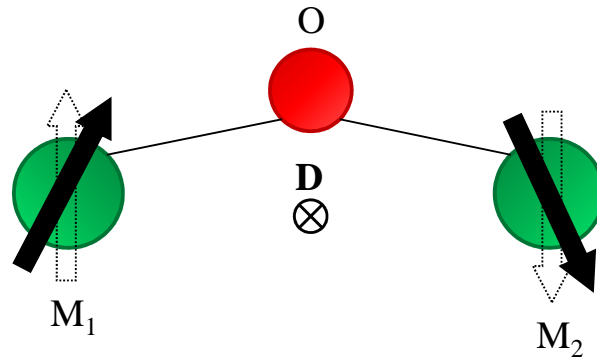


FIGURE 1.11: Dzyaloshinskii - Moriya Interaction in system consisting of two magnetic ions M_1 and M_2 and a diamagnetic ion O . DM vector \mathbf{D} is non-zero because the geometric center of $[M_1 M_2]$ is not the center of inversion of the system. \mathbf{D} is dependent on the position of O and promotes a canting of the spins of M_1 and M_2 .

its neighbors. Once the first two spins align anti-parallel, the third one is frustrated because its two possible orientations, up and down, give the same energy. The third spin cannot simultaneously minimize its interactions with both of the other two, which result in the frustration. The spin configuration of hexagonal RMnO_3 , where R is a rare earth elements, is the result of frustration. The detail will be discussed in chapter of hexagonal RMnO_3 .

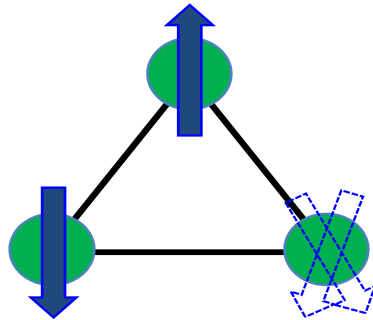


FIGURE 1.12: The spin configuration of magnetic frustration.

1.2.2.4 The magnon

A magnon is a collective, quantized excitation of the periodic magnetic order in a crystal lattice. In the equivalent wave picture of quantum mechanics, a magnon can be viewed as a quantized spin wave. As a quasiparticle, a magnon carries a fixed amount of energy and lattice momentum throughout the spin structure. Magnons with nonvanishing average magnetization could interact with electromagnetic waves via ac magnetic

field. Depending on the magnetic ground state such optical magnons are termed either ferromagnetic resonances (FMR) or antiferromagnetic resonances (AFMR). Therefore, magnons are responsible for the magneto-active absorption.

Nevertheless, magnons in magnetoelectric multiferroics are generally not pure spin waves but contain significant contributions from electric dipole matrix moments. Such excitations are thus given the name electromagnon. Due to the coupling between the lattice and spin orders, electromagnons correspond to hybrid spin-lattice excitations that can be excited by the electric component of electromagnetic wave. (Pimenov et al., 2006)

1.2.3 The magnetoelectric effect

The magnetoelectric effect, in its most general definition, describes the coupling between electric and magnetic fields in matters (i.e. induction of magnetization (M) by an electric field (E) or polarization (P) generated by a magnetic field (H)). In 1888, Röntgen observed that a moving dielectric compound placed in an electric field became magnetized, which was followed by the observation of the reverse effect : polarization generation of a moving dielectric in a magnetic field. Both, however, are not the intrinsic effects of matters. (Rontgen, 1888) In 1894, by crystal symmetry consideration, Curie predicted the possibility of an intrinsic magnetoelectric effect in some crystals. (Curie, 1894) Subsequently, Debye coined this kind of effect as a “magnetoelectric effect”. (Debye, 1926) The first successful observation of the magnetoelectric effect was realized in Cr_2O_3 , and the magnetoelectric coupling coefficient was 4.13 ps/m. (Astrov, 1960) Up to now, more than 100 compounds that exhibit the magnetoelectric effect have been discovered or synthesized. Thermodynamically, the magnetoelectric effect can be understood within the Landau theory framework, approached by the expansion of free energy for a magnetoelectric system,

$$F(\mathbf{E}, \mathbf{H}) = F_0 - P_i^S E_i - M_i^S H_i - \frac{1}{2} \epsilon_0 \epsilon_{ij} E_i E_j - \frac{1}{2} \mu_0 \mu_{ij} H_i H_j - \alpha_{ij} E_i H_j - \frac{\beta_{ijk}}{2} E_i H_j H_k + \frac{\gamma_{ijk}}{2} H_i E_j E_k - \dots \quad (1.17)$$

Then the polarization is

$$P_i = \alpha_{ij} H_j + \frac{\beta_{ijk}}{2} H_j H_k + \dots \quad (1.18)$$

and the magnetization is

$$M_i = \alpha_{ij} E_j + \frac{\gamma_{ijk}}{2} E_j E_k + \dots \quad (1.19)$$

where F_0 is the ground state free energy, subscripts (i, j, k) refer to the three spatial coordinates, E_i and H_i the components of the electric field \mathbf{E} and magnetic field \mathbf{H} , respectively, P_i^S and M_i^S are the components of spontaneous polarization \mathbf{P}^S and ma-

gnetization M^S , ϵ_0 and μ_0 are the dielectric and magnetic susceptibilities of vacuum, μ_{ij} and α_{ij} are the second-order tensors of dielectric and magnetic susceptibilities, β_{ijk} and γ_{ijk} are the third-order tensor coefficients and, most importantly, α_{ij} is the components of tensor which is designated as the linear magnetoelectric effect and corresponds to the induction of polarization by a magnetic field or a magnetization by an electric field. The rest of the terms in the equations 1.17, 1.18 and 1.19 correspond to the high-order magnetoelectric effects parameterized by tensors β_{ijk} and γ_{ijk} . Unfortunately, the magnetoelectric effect in single-phase compounds is usually too small to be practically applicable. One way to enhance the magnetoelectric response in single-phase compounds significantly is to make use of strong internal electromagnetic fields in the components with large dielectric and magnetic susceptibilities. This possibility corresponds to type-I multiferroics. The other way is looking for materials with strong coupling of ferroelectric and ferromagnetic orders like the type-II multiferroics.

1.3 The type I multiferroics

Type-I multiferroics are “older” and more numerous. They are often good ferroelectrics, and the critical temperature of the ferroelectric transition can be well above room temperature. Unfortunately, the coupling between magnetism and ferroelectricity in these materials is usually rather weak. The challenge for this group of multiferroics is to keep all their positive features, but enhance this coupling. In the following, we will focus on four of the major subclasses.

1.3.1 Perovskites Multiferroic

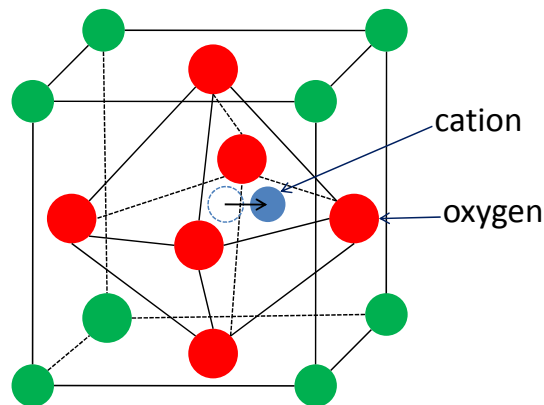


FIGURE 1.13: Structure of Multiferroic perovskite, shift of the cation to oxygen atoms leads to polarization.

Probably the best-known ferroelectrics are the perovskites like BaTiO_3 or $\text{Pb}(\text{ZrTi})\text{O}_3$ (PZT). The structure of perovskite is shown in Fig. 1.13. There are many magnetic

materials among perovskites, and also many ferroelectrics. However there is practically no overlap of these two types of perovskites. For magnetism one needs partially filled d shells of a transition metal. Practically all ferroelectric perovskites contain transition metal ions with an empty d shell, such as Ti^{4+} , Ta^{5+} , W^{6+} ions. Ferroelectricity in these systems is caused by the off-center shift of the transition metal ion, which forms strong covalent bonds with one (or three) oxygens, using their empty d states. The presence of real d electrons in d^n configurations of magnetic transition metals suppresses this process, preventing ferroelectricity in magnetic perovskites. (Hill, 2000) One possible way around this problem may be making “mixed” perovskites with d^0 and d^n ions. Unfortunately the coupling of magnetic and ferroelectric subsystems in mixed perovskites is rather weak.

1.3.2 Ferroelectricity due to charge ordering

Another mechanism that can lead to ferroelectricity and classified to type-I multiferroicity can be charge ordering, often observed in transition metal compounds, especially those formally containing transition metal ions with different valence. If, after charge ordering, both sites and bonds turn out to be inequivalent, this can lead to ferroelectricity [Fig. 1.14] . This mechanism is involved in systems such as $\text{Pr}_{1/2}\text{Ca}_{1/2}\text{MnO}_3$ (Efremov et al., 2004) or in nickelates RNiO_3 (Cheong & Mostovoy, 2007) with charge ordering. Figure 1.14 a. is the charge-ordering pattern with a simple check board type which is characterized by the alternation of Mn^{3+} and Mn^{4+} sites. The second pattern correspond to that charges localized not on the sites but on bonds as shown in Fig. 1.14 b. Besides these two pure states, the intermediate pattern is indicated in Fig. 1.14 c. . In this figure, it is clear that the charge-ordering pattern is not inversion symmetry and is ferroelectric. Another possibility mechanism is when the bonds are inequivalent because of the structure of the material, the site-centered charge order appearing on top of that. This is the case in an organic ferroelectric $(\text{TMTTF})_2\text{X}$ (Monceau et al., 2001), and also in the multiferroic LuFe_2O_4 (Ikeda et al., 2005).

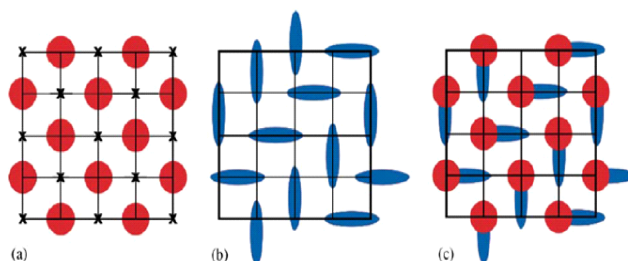


FIGURE 1.14: (a) Site-centered charge ordering in half-doped manganites (b) bond-centred ordering, and (c) combined ordering, giving ferroelectricity. (Ikeda et al., 2005)

1.3.3 Ferroelectricity due to lone pairs

In BiFeO_3 , BiMnO_3 and PbVO_3 , Bi^{3+} and Pb^{2+} play the major role at the origin of ferroelectricity. (Cohen, 1992) In these ions, there are two outer 6s electrons that do not participate in chemical bonds. They are called lone pairs. The lone pairs state is unstable leading to break the inversion symmetry. They have a strong polarizability, the condition required for ferroelectricity in the classical description. (Picozzi & Ederer, 2009) The microscopical origin of ferroelectricity is the ordering of these lone pairs in one direction [Fig. 1.15].

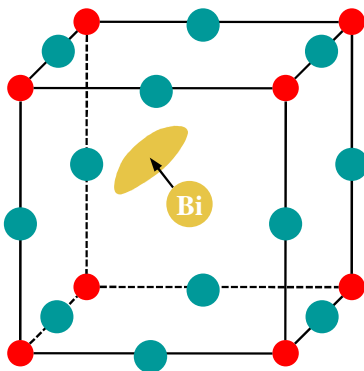


FIGURE 1.15: Material containing Bi^{3+} ion with isolated pairs line in one direction creating ferroelectricity.

1.3.4 “Geometric” ferroelectricity

Finally, we consider the geometric ferroelectricity, a case realized in, for example, YMnO_3 . Ferroelectricity in YMnO_3 is caused by the tilting of the practically rigid MnO_5 block. This tilting occurs just to provide closer packing, and as a result the oxygen ions move closer to the rather small Y ions [Fig. 1.16]. The detail will be discussed in the chapter of hexagonal RMnO_3 .

1.4 The type I multiferroic : BiFeO_3

Multiferroic BiFeO_3 is the most known and studied type I multiferroic. Indeed, it is the only one that presents ferroelectric and magnetic order above room temperature, which makes it one of the best candidates for applications in spin electronics or storage information despite its low magnetoelectric coupling.

1.4.1 Bulk BiFeO_3

1.4.1.1 Structure

BiFeO_3 has three different phases. Above 1205K, BiFeO_3 is in the γ phase with cubic structure. Between 1205K and 1089K, BiFeO_3 presents a β phase. The structure

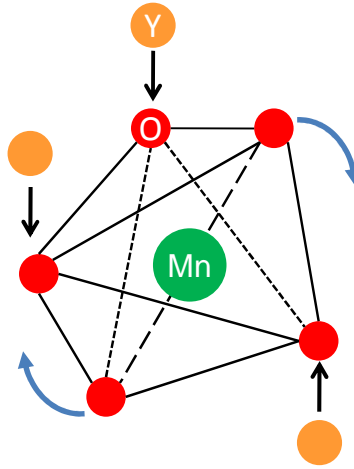


FIGURE 1.16: The ferroelectricity of YMnO_3 is due to the Y-O displacement caused by the tilt of MnO_5 . This compound becomes multiferroic when Mn arrange themselves at a lower temperature, showing the magnetic order.

has not been determined yet, it could be orthorhombic ($P2mm$) (Palai et al., 2008), rhombohedral (R_3m) (Selbach et al., 2008) or monoclinic ($P2_1/m$) (Haumont et al., 2008)

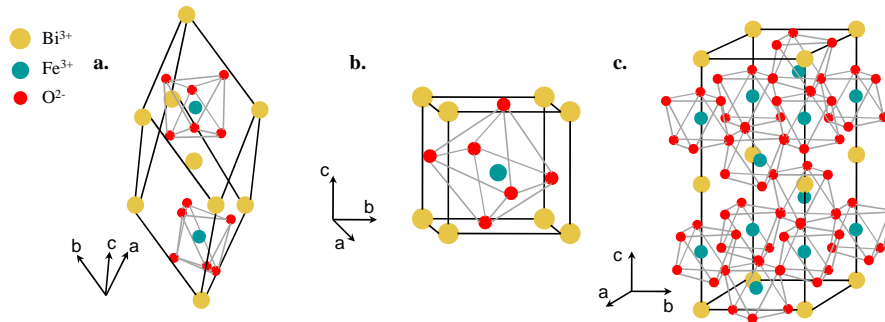


FIGURE 1.17: BiFeO_3 crystal structure : **a** double rhombohedral structure **b** pseudocubic and **c** hexagonal.

Below 1089K, BiFeO_3 is classified as α phase with rhombohedral R_3m structure. (Moreau et al., 1971) This structure is perovskite type with a 0.65% misfit due to the Bi^{3+} polarization. The rhombohedrally distorted perovskite structure can be indexed with $a_{rh} = 5.63\text{\AA}$ and $\alpha_{rh} = 59.35^\circ$, owing to the shift of Bi ions (Fig. 1.17 a.), which can also presents as pseudo-cubic structure with $a = 3.96\text{\AA}$ and $\alpha = 89.47^\circ$ as shown in Fig. 1.17 b. . This structure can also be classified as a distorted hexagonal with parameter of $a_{hex} = 5.58\text{\AA}$ and $c_{hex} = 13.87\text{\AA}$ (Fig. 1.17 c.) (Lebeugle et al., 2007)

1.4.1.2 Ferroelectricity

In bulk BiFeO_3 , without external electric field, the spontaneous polarization is due to the displacement of Bi^{3+} along $[111]$ direction as shown in Fig. 1.18. This displacement induces a deformation of the perovskite BiFeO_3 : 54 pm for Bi^{3+} and 13 pm for Fe^{3+} from their original positions. Therefore, the centers of negative and positive charges are no longer coincided and spontaneous polarization appears along $[111]$ direction.

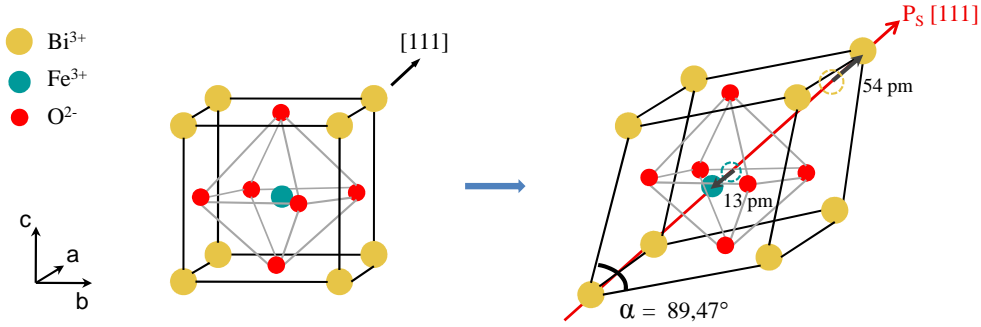


FIGURE 1.18: Distortion of the pseudo-cubic lattice along the $[111]$ direction at the transition temperature T_C .

Figure 1.19 shows a polarization loop of BiFeO_3 single crystal at room temperature obtained by measuring currents from the reversal of the polarization according to the applied voltage (Lebeugle et al., 2007). From this hysteresis loop, we can obtain the coercive field values $E_c = 12 \text{ kV/cm}$ and the remanent polarization $P_r = 60 \mu\text{C/cm}^2$ in the applied electric field along $[010]$. During this cycle of polarization (Fig. 1.19) the polarization direction switches from one direction to another. There are eight polarization equivalent directions and the polarization direction can be switched by 180° , 109° , 71° according to positive and negative orientation along the four diagonals as shown in Fig. 1.20 (Zhao et al., 2006). Switching of the polarization by either 109° or 71° changes the rhombohedral axis and is therefore associated with a switching of the ferroelastic domain state. In BiFeO_3 single crystal, the $[111]$ direction is favorable.

1.4.1.3 Magnetic properties

The magnetic Néel temperature of BiFeO_3 is 643K. The local short-range magnetic ordering of BiFeO_3 is G-type antiferromagnet. Each Fe^{3+} spin is surrounded by six antiparallel spins on the nearest Fe neighbors. The spins are in fact not perfectly antiparallel, as there is a weak canting moment caused by the local magnetoelectric coupling to the polarization, which originates from the Dzyaloshinskii-Moriya interaction. (Lebeugle et al., 2008; Sosnowska et al., 1982) The magnetic order is subjected to long-range modulation associated with a cycloidal spiral with a period length of approximately 62 nm. (Fig. 1.21). The details are presented in next section.

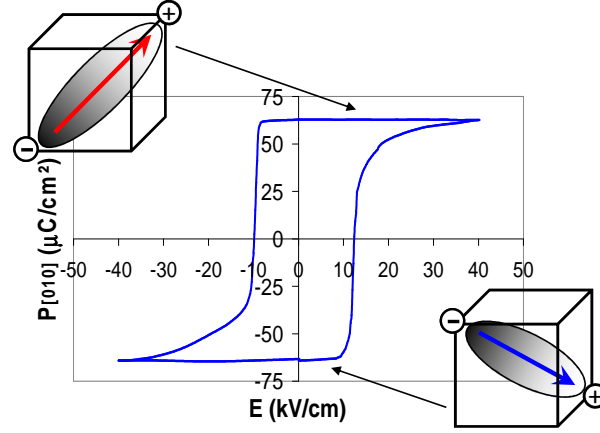


FIGURE 1.19: Polarization cycle of BiFeO_3 single crystal at room temperature, the polarization direction varies with the applied electric field. (Lebeugle et al., 2007)

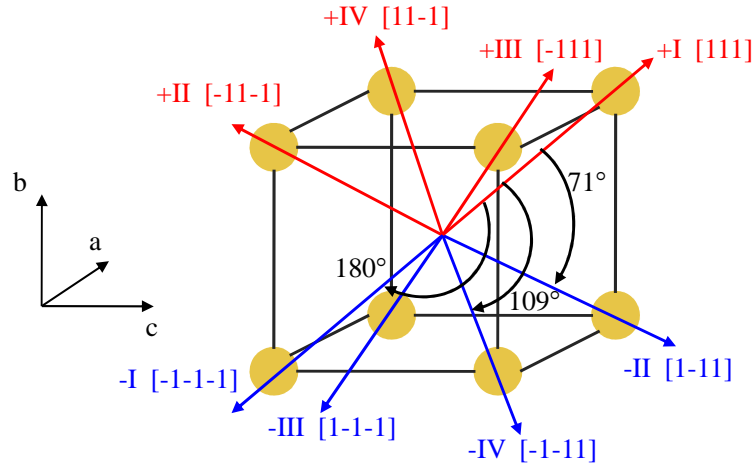


FIGURE 1.20: Diagram of the eight directions of the electric polarization in the pseudo-cubic lattice of BiFeO_3 .

The cycloid is described by a propagation vector q directed into one of the three directions equivalent $[0-11]$, $[10-1]$ and $[-110]$, respectively contained in the $(-1-12)$, $(-12-1)$ and (-211) planes. Samples of BiFeO_3 synthesized by D. Lebeugle et al. are single crystals monodomain and the magnetic cycloid only propagates along the $[10-1]$ direction and is contained in (-121) plane. (Lebeugle et al., 2008)

Measurements at room temperature of magnetization as a function of magnetic field applied to a powder of BiFeO_3 shows a linear variation of the magnetization as a function of the field (Fig.1.22 a.). (Zhang et al., 2005) This linear variation is characteristic of an antiferromagnetic arrangement of the magnetic moments of Fe^{3+} . (Lebeugle et al., 2007)

Several magnetization measurements as a function of magnetic field at low temperature on thin films (Naganuma & Okamura, 2007), ceramics (Zhang et al., 2005) and single crystals (Catalan & Scott, 2009) show a hysteresis cycle highlighting the presence

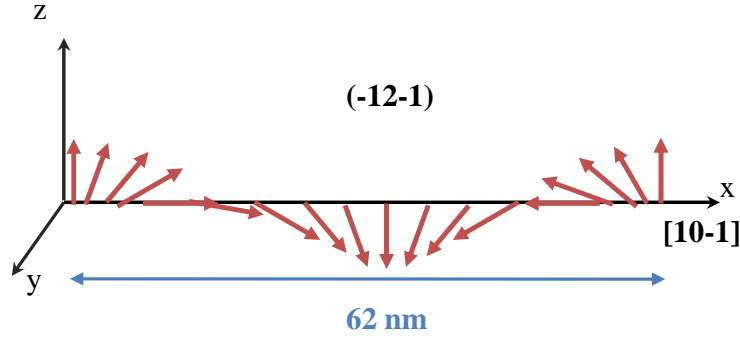


FIGURE 1.21: Antiferromagnetic cycloid spiral with a period of 62 nm propagating in the $[10-1]$ direction and contained in the $(-12-1)$ plane.

of a small ferromagnetic component (Fig. 1.22 b). This low moment is induced by the rotation of oxygen octahedral.

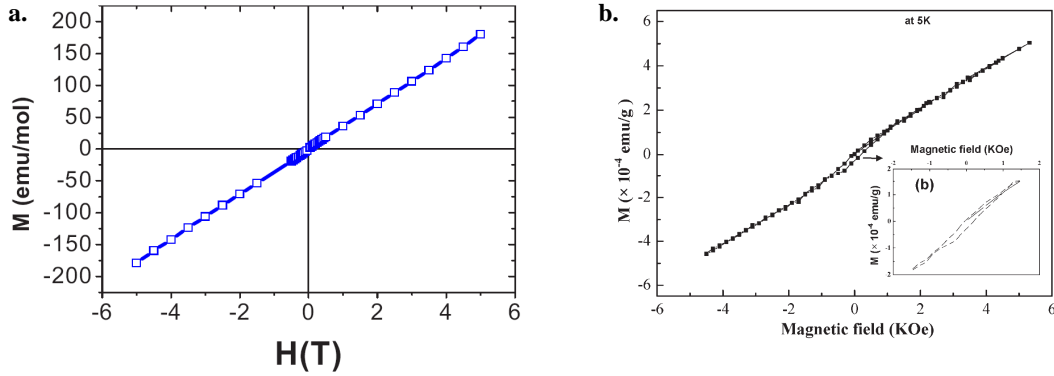


FIGURE 1.22: **a.** Magnetization curve as a function of magnetic field at room temperature for BiFeO_3 powder (Lebeugle et al., 2007). **b.** Hysteresis loop of magnetization as a function of magnetic field at low temperature (5 K) for BiFeO_3 single crystal.

1.4.1.4 Magnetolectric coupling

The magnetolectric effect corresponds to the coupling between magnetic and ferroelectric orders. The existence of a spin cycloid averages out any linear ME coupling between polarization and magnetization. Y. F. Popov et al. showed a quadratic magnetolectric coupling when the magnetic cycloid is present. The application of a magnetic field above 20 T removed the cycloid and shows a linear magnetolectric effect. (Popov et al., 1993, 2001)

The theory behind these effects is subtle. Above T_C , BiFeO_3 is a paraelectric structure, the magnetic structure of BiFeO_3 would be a perfect G-type antiferromagnetic with no net magnetic moment. However, below T_C , the ferroelectric polarization breaks the center of symmetry and induces a small canting of the spins via the Dzyaloshinskii-Moriya Interaction. (Catalan & Scott, 2009) This canting results in the very small ma-

gnetization. (Kadomtseva et al., 2004; Fennie, 2008) In addition to this canting, there is also a ferroelectricity induced by the spin cycloid that averages out the local canted magnetism. High magnetic field can destroy the cycloid, thereby recovering the canted state and its associated remnant magnetization. In this state, the linear magnetoelectric is allowed.

In 2008, neutron measurements on single crystals of BiFeO_3 showed that the (-12-1) plane contains not only the spin cycloid but also the macroscopic polarization vector (Fig.1.23 a.). Moreover, this work showed that the application of an electric field polarization not only switch the polarization but also switch the cycloid plane. The polarization and the cycloid remaining in the same plane (Fig. 1.23 b.). (Lebeugle et al., 2008) If the spin cycloid is included into the free energy, the lowest energy state is always achieved when the cycloid wavevector \mathbf{q} is perpendicular to \mathbf{P} . Hence the spins are pinned to the plane formed by \mathbf{P} and \mathbf{q} (Chu & Ramesh, 2008).

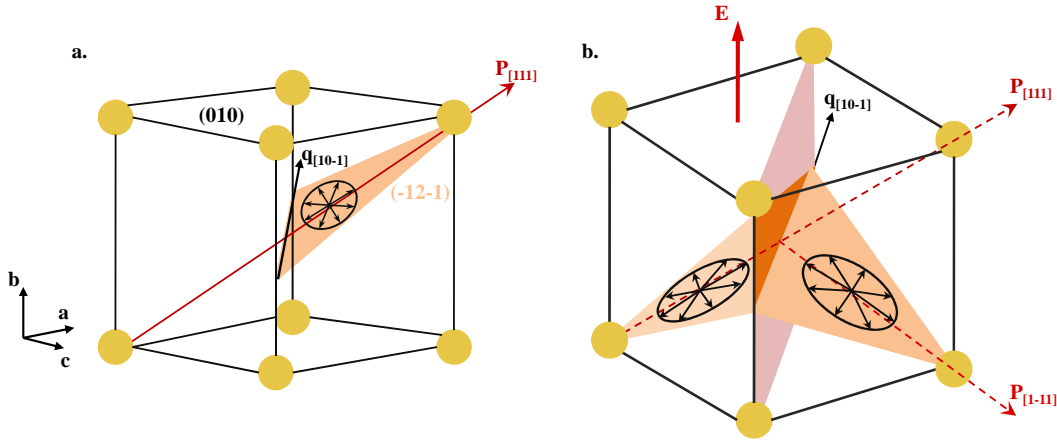


FIGURE 1.23: **a.** The spin cycloid is in the (-12-1) plane with a wavevector along [10-1] direction. **b.** Switching the polarization direction from [10-1] to [1-11] induced the tilting of the spiral plane.

Recently, Rovillian et al.'s experiment clearly shows that the application of an external electric-field (\mathbf{E}) to BiFeO_3 bulk can result in a giant shift of magnon frequencies that was linear in \mathbf{E} and 10^5 larger than any other known \mathbf{E} -field effect on magnon spectra. This work suggests that DM interaction is not the only Linear Magnetoelectric effect in BiFeO_3 (Rovillain et al., 2010) The following theoretical work shows that the spin-orbit coupling at the bismuth ion sites could result in a special kind of magnetic anisotropy that is linear in the applied \mathbf{E} -field, and this interaction is capable of disrupting the magnetic cycloid state of BiFeO_3 , leading to a remarkable level of \mathbf{E} -field control of magnetism. (de Sousa et al., 2012)

1.4.1.5 Spin modes

Below the Néel temperature, the spins of Fe^{3+} ions form an incommensurate cycloid. The corresponding spin wave modes (magnon) were firstly optically observed by Cazayous(Cazayous et al., 2008) and Singh(Singh et al., 2008).

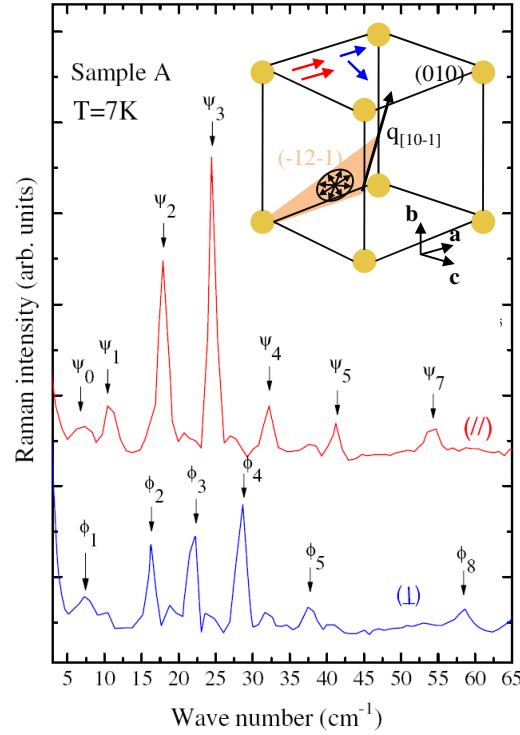


FIGURE 1.24: Raman spectra of spin excitations in BiFeO_3 low temperature (7 K) and inside figure shows the laser polarization directions and the crystal structure of BiFeO_3 . (Cazayous et al., 2008)

Cazayous et al. show two different types of peaks at low energies using two different polarizations (Fig. 1.24). (Cazayous et al., 2008) They observe the first type of peaks using the polarization of the electric field of the incident and scattered light parallel to the propagation vector q of the cycloid. These peaks are named ϕ . The second type of peaks is observed using a polarization of the scattered light perpendicular to that of the incident light and the propagation vector. These modes are appointed ψ . These peaks at low energies are associated with spin excitations. Cazayous et al. have associated these peaks to the spin oscillations in (ϕ) and out (ψ) the cycloidal plane based on a phenomenological Ginzburg Landau theory.

This theory developed by R. de Sousa and J. E. Moore is based on the phenomenological description of antiferromagnetism by Landau in 1937 and ferroelectricity by Ginzburg in 1949. (de Sousa & Moore, 2008b) To take account of the incommensurate cycloid spin, the Lifshitz term is introduced :

$$F = -\alpha \mathbf{P} \cdot [\mathbf{L}(\nabla \cdot \mathbf{L}) + \mathbf{L} \times (\nabla \times \mathbf{L})] \quad (1.20)$$

The ground state of the cycloid :

$$\mathbf{L}_0(x) = L_0[\cos(Qx)\mathbf{z} + \sin(Qx)\mathbf{x}] \quad (1.21)$$

where $Q = \alpha/c$:the propagation vector of the cycloid and $L_0 = (-a + cQ^2)/u$. α is nonhomogeneous relativistic exchange constant, a is exchange stiffness and c is magnetic anisotropy constant. The direction of the cycloid is along x . Antiferromagnetic spin moments are in the plane containing z .

Firstly a phase change based on the transformation $qx \rightarrow qx + \Phi/L_0$ gives : $\mathbf{L} = \Phi[\cos(qx)\mathbf{x} - \sin(qx)\mathbf{z}] = \Phi\mathbf{D}$ with \mathbf{D} the tangent vector to the direction of spin . The second transformation is a rotation of the cycloid in the xy plane such that $qx \rightarrow q(x + \eta y)$ gives : $\mathbf{L} = \eta L_0 q y \mathbf{D}(x) + \eta L_0 \sin(qx)\mathbf{y} = \phi\mathbf{D} + \psi\mathbf{y}$. We can decompose the mode of propagation of cycloid mode into two components. The ϕ mode corresponds to the oscillation of the spins in the cycloid plane(xz), it is called cyclon mode. The ψ mode corresponds to the oscillation of the spins out of the cycloid plane and is called extra-cyclon as shown in Fig. 1.25.

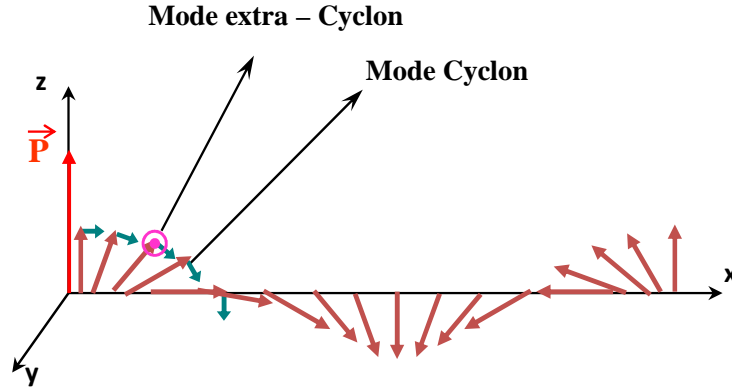


FIGURE 1.25: Decomposition of the cyclon (ϕ) mode and extra-Cyclon (ψ) mode.

Finally, we obtain the expression of the free energy of BiFeO₃ under this phenomenological Ginzburg-Landau model :

$$\begin{aligned} F = & \frac{a}{2}M^2 + \frac{r}{2}L^2 + \frac{u}{4}L^4 + \frac{c}{2} \sum_{i=x,y,z} (\nabla L_i)^2 \\ & - \alpha \mathbf{P} \cdot [\mathbf{L}(\nabla \cdot \mathbf{L}) + \mathbf{L} \times (\nabla \times \mathbf{L})] \\ & + \frac{\alpha}{2}P^2 + \frac{\gamma}{4}P^4 + \frac{\delta}{6}P^6 - \mathbf{E} \cdot \mathbf{P} \end{aligned} \quad (1.22)$$

To obtain the energy spectrum of spin waves (Fig. 1.26) the equations are linearized as a function of ferroelectric and antiferromagnetic order. The dispersion curves of propagation are shown in Fig. 1.26. The two initial dispersion curves ϕ and ψ modes are folded at the center of the Brillouin zone due to the incommensurability of the cycloid. The edge of Brillouin zone is not at π/a but at π/λ (λ is the period of incommensurate cycloid). Therefore, we can observe these spin wave modes at zero wavevector by Raman

spectroscopy.

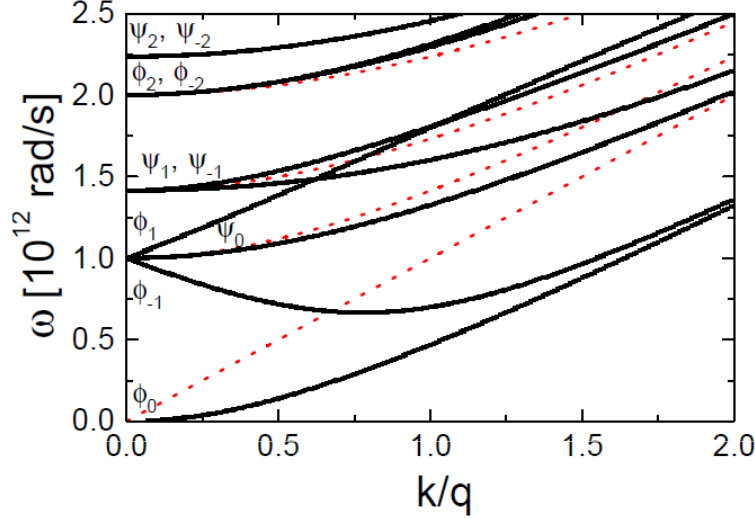


FIGURE 1.26: Dispersion curves of the propagation modes of the cycloid : Cyclon ϕ and extra-Cyclon ψ (de Sousa & Moore, 2008b)

For a zero wave vector ($\mathbf{k}/\mathbf{q} = 0$), the energy of the cyclon (E_c) and extra-cyclon (E_{exc}) modes can be written in a simplified relation :

$$E_c(n) = \epsilon_c(q)n \quad (1.23)$$

$$E_{exc}(n) = \epsilon_c(q)(n^2 + 1)^{\frac{1}{2}} \quad (1.24)$$

where $\epsilon_c(q)$ is the cyclon energy at wavevector q . The calculated value is 5.3cm^{-1} .

From these expressions and Figure 1.27, it can be noted that the main difference between the modes of extra-Cyclon and Cyclon is the zero order mode. The energy of the ψ_0 is 5.3 cm^{-1} while that of ϕ_0 is 0 cm^{-1} . This difference is due to the coupling between the spin wave mode and a phonon. The energy gap of ψ_0 mode indicates a coupling between the cycloid magnetic order and electrical polarization which can be also interpreted as electromagnon.

Figure 1.27 presents the comparison of the measured energies of two modes from Fig. 1.24 with the calculated energies of cyclon and extra-cyclon at the zone center (Fig. 1.26). A good agreement between the experimental data and the calculated results is obtained by adjusting $\epsilon_c = 7.5 \pm 0.2\text{cm}^{-1}$.

Recently, Talbayev et al. measured THz transmission spectra of BiFeO_3 at various temperatures with two polarization and found four modes at $18.4, 20.5, 22.5$ and 27cm^{-1} , and the splitting between the ψ_{+1} and ψ_{-1} modes. (Talbayev et al., 2011) However, in the description of de Sousa and Moore (de Sousa & Moore, 2008b), these two modes are degenerate and possess the same resonance frequency. To understand this observation, Fishman et al. built up a new model which takes into account of easy-axis anisotropy and the Dzyaloshinski-Moriya interaction. (Fishman et al., 2012) According

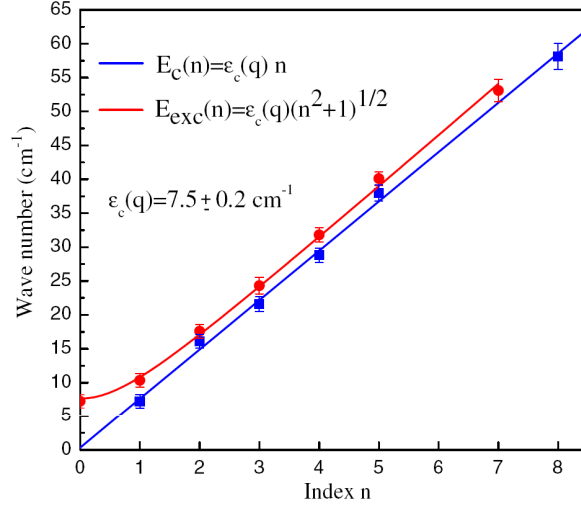


FIGURE 1.27: Experimental frequencies of the modes ϕ (blue squares) and modes ψ (red circles) as a function of the mode index n . The expressions for the calculated energies $E_c(n)$ and $E_{exc}(n)$ perfectly fit of experimental data using a cyclon energy $\epsilon_c = 7.5 \pm 0.2 \text{ cm}^{-1}$. (Cazayous et al., 2008)

to this model, there is an excellent agreement for three of the four experimental peaks and the anisotropy splits the $\psi_{\pm 1}$ mode into peaks at 20 and 21.5 cm^{-1} by distorting the cycloidal spin state. The upper $\psi_{\pm 1}$ mode at 21.5 cm^{-1} is identified as electromagnon as shown in Figure 1.28

1.4.2 Thin film BiFeO₃

1.4.2.1 Structure

In 2003, Ramesh's group reported the enhancement of polarization (P_r , 50 to 60 $\mu\text{C}/\text{cm}^2$) in heteroepitaxially constrained thin films of BiFeO₃. (Wang et al., 2003) The large ferroelectric polarization attracts a lot of attention to the BiFeO₃ thin film research. The phase structure of BiFeO₃ thin film is strongly related to the strain value. According to the recent experimental and computational works, the stress-induced phase transition follows the path of rhombohedral (R) to monoclinic (M_A) to monoclinic (M_C) to tetragonal (T). (Christen et al., 2011) When the rhombohedral perovskite BiFeO₃ is grown on a substrate having a square in-plane lattice, its symmetry is lowered to a monoclinic phase, except in free standing membranes or very thick films that remain rhombohedral. From tensile to moderate compressive strain, the BiFeO₃ thin film structure is monoclinic which loosely resembles the rhombohedral structure, so we refer to it as the "R-like" structure with R3c symmetry. When compressive strains exceed -4.5%, the strong strains result in a strongly increased out-plane lattice parameter c_{pc} , leading to a c_{pc}/a_{pc} ratio of 1.25 (where a_{pc} is the in-plane lattice parameter and the subscript pc refers to the pseudocubic notation) and an abrupt change of Fe coordination. This monoclinic phase resembles tetragonal structure, and therefore we refer

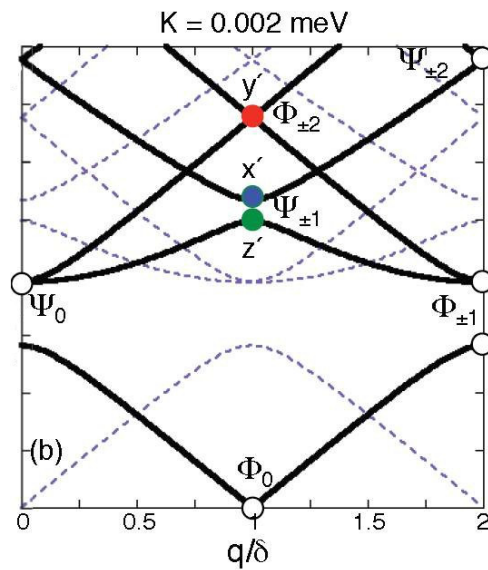


FIGURE 1.28: The spin wave modes of BiFeO_3 versus q/δ . Dashed lines show all possible excitations and the solid lines show only those modes with non-zero intensity. K is the easy-axis anisotropy constant which equal 0.002meV in this case. The $\psi_{\pm 1}$ mode splits and the lower $\phi_{\pm 2}$ mode is activated. The upper $\psi_{\pm 1}$ mode corresponds to electromagnon. (Fishman et al., 2012)

to is as “T-like” structure with $P4mm$ symmetry. The “R-like” and “T-like” structures are shown in Fig. 1.29.

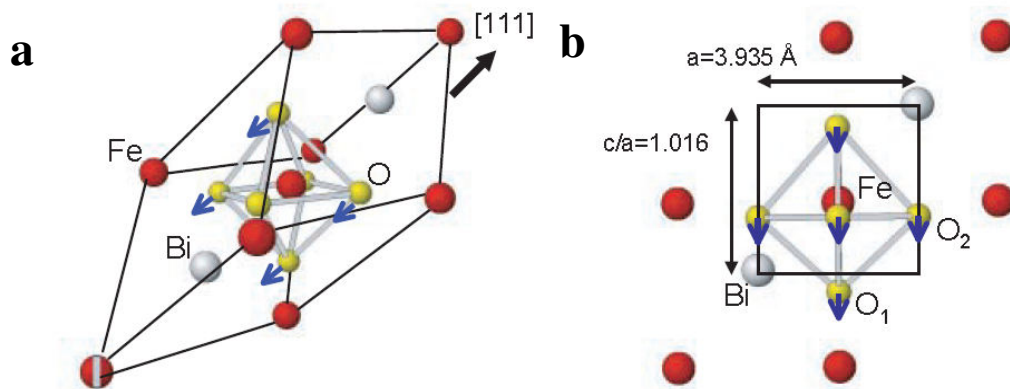


FIGURE 1.29: Schematic of the prototypical **a.** “R-like” structure and **b.** “T-like” structure BiFeO_3 unit cells. (Wang et al., 2003)

1.4.2.2 Ferroelectric properties

Both “R-like” and “T-like” phases are ferroelectric. In “R-like” phase, the polarization P points approximately along the $[111]_p c$ direction and rotates towards the $[001]_p c$ direction with increasing compressive strain as shown in Fig. 1.30, due to the strong coupling between polar displacements and oxygen octahedral tilt. (Jang et al., 2008; Dupe et al., 2010; Choi et al., 2011) For T-like phase, in 2005, by first principle calculation, Ederer and Spladin showed that the existence of a very large polarization of $151 \mu\text{C}/\text{cm}^2$ is due to the strong distorted of P4mm T-like structure (Ederer & Spladin, 2005). A very large of projection of P onto the $[001]_p c$ direction was measured in agreement with theoretical predictions.(Bea et al., 2009)

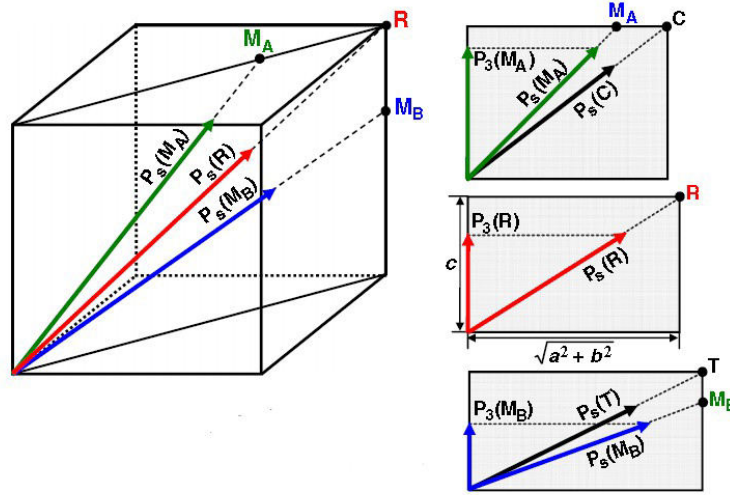


FIGURE 1.30: The spontaneous polarization directions of the rhombohedral (R) and monoclinic (M_A and M_B) phases of BiFeO_3 . The monoclinic M_A and M_B phases occur for biaxial compressive and tensile strains, respectively. In-plane strains induce the rotation of the spontaneous polarization in the $(110)_p$ plane. For M_A and M_B phases, the rotation of P_s is much more pronounced than the simple rotation of P_s by the change in the $c=a$ ratio (denoted by C and T).(Jang et al., 2008)

Recently, by using the aberration-corrected high-angle annular dark-field scanning transmission electron microscopy (HAADF-STEM) and electron energy-loss spectroscopy (EELS), Rossell et al. provided direct experimental evidence for the square-pyramidal oxygen coordination of the iron atoms in the high-strain phase and confirm that the iron and equatorial oxygen columns are significantly displaced along the c -direction as shown in Fig. 1.31. The results clarify the microscopic origin of the giant ferroelectric polarization measured in high-strain BiFeO_3 thin films. (Rossell et al., 2012)

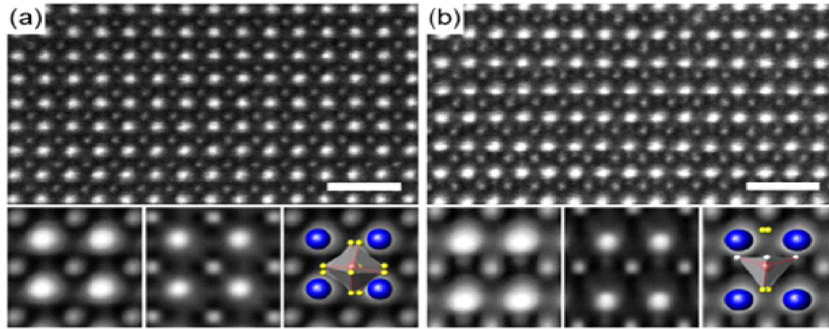


FIGURE 1.31: **a.,b.** Atomic-resolution HAADFSTEM images of the R and T phase, respectively. Insets below, from left to right : Averaged structure images ; simulated STEM images for a 50-nm-thick crystal ; and averaged structure images with overlaid structure models. Blue, red, and yellow spheres represent Bi, Fe, and oxygen atoms, respectively. For the T-phase model, the equatorial O(2) oxygen atoms are shown in white to differentiate them from the yellow apical O(1) oxygen atoms. The scale bars are 1 nm.(Rossell et al., 2012)

1.4.2.3 Magnetic properties

Meanwhile, many researches are focused on the relationship between the structure and magnetic properties of BiFeO_3 thin films. In Wang's work, it is observed that the magnetization depends on the thickness of sample showing the effect of the mismatch strain on the magnetic response.(Wang et al., 2003) However, Erenstein et al. did not observe any thickness dependence of magnetic properties in the films deposited on the same substrate STO.(Eerenstein et al., 2005) The subsequent studies attributed the occurrence of a ferromagnetic like moment and thickness dependent magnetic properties to two extrinsic factors : the oxygen deficiencies(Wang et al., 2005) and the presence of a parasitic magnetic phase(Bea et al., 2005).

Neutron diffraction measurements reveal that G-type antiferromagnetic order is observed in the BiFeO_3 thick film (240 nm) on STO but the incommensurate cycloid present in the bulk is absent. The similar magnetic moments were observed in BiFeO_3 thin film on LSAT (thicker than 110 nm) by high-resolution x-ray diffraction studies but a weak enhanced magnetic moment is observed in full strained films(thinner than 75 nm).(Rana et al., 2007) In 2005, Bai et al. observed that the strain can release of latent magnetization due to the destruction of spin cycloid and predicted that 0.5% strain is big enough to break the spin cycloid.(Bai et al., 2005) Recently, MacDougall et al. observed antiferromagnetism with largely G-type character at lower Neel temperature (324K) in T-like phase in BiFeO_3 thin films with high compressive strain. Evidence for a second transition, possibly a minority magnetic phase with C-type character, with $T_N=260\text{K}$ is also observed(MacDougall et al., 2012).

Recently, Infante et al. reported the Néel temperature of BiFeO_3 thin films on different substrates is virtually independent of strain, while the Curie temperature strongly decreases under compressive strain as shown in Fig. 1.32 (in contrast with conventional ferroelectric thin film). This unexpected result is supposed to arise from

a competition between polar displacement and oxygen octahedral tilt. The effect of strain on the magnetic structure is unclear. (Infante et al., 2010) These results show that strain is an efficient method to adjust the Curie temperature. Nevertheless, the effect of strain on the magnetic order and properties of BiFeO_3 thin films need to be highlighted.

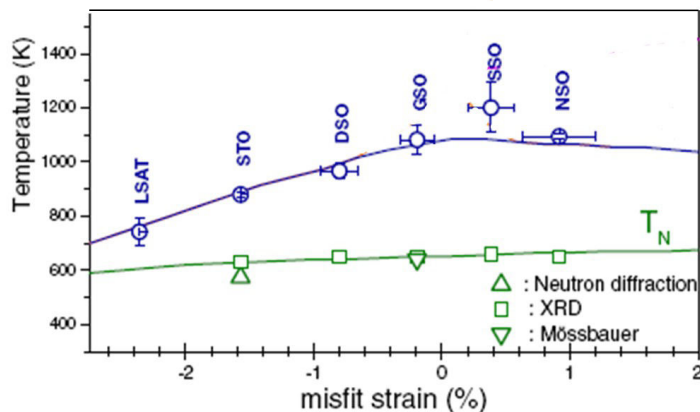


FIGURE 1.32: Theoretical results based on the effective Hamiltonian of BFO film transition temperatures (T_C , blue line, and T_N , green line) as a function of misfit strain and experimental T_C (circles) and T_N (squares and triangles) values. (Infante et al., 2010)

1.4.2.4 Magnetolectric coupling

The magnetolectric coupling is also reported in BiFeO_3 thin films. In 2006, Zhao et al. observed a coupling between ferroelectric and antiferromagnetism in BiFeO_3 thin film due to the coupling of both antiferromagnetic and ferroelectric domains to the underlying ferroelastic domain structure. (Zhao et al., 2006) The first principles calculations of the magnetocrystalline anisotropy energy showed that the preferred orientation of the individual spins, in the absence of the spiral, is perpendicular to the rhombohedral axis. The orientation of the antiferromagnetic sublattice magnetization therefore seems to be coupled to the ferroelastic strain state of the system and should always be perpendicular to the ferroelectric polarization. As a result, polarization switching by either 71° or 109° should change the orientation of the easy magnetization plane. For example, if the polarization is switched by 109° from the $[111]$ into the $[1-1-1]$ direction, the easy magnetization plane should change as indicated in Fig. 1.33 c. (Fig. 1.33 d. shows the analogous case of 71° switching.)

In 2008, Gatalan et al. show that the ferroelectric domains in the very thin BiFeO_3 film (thinner than 35 nm) have irregular domain walls and the domains are significantly larger than those of other ferroelectrics of the same thickness, and closer in size to those of magnetic materials, which is consistent with a strong magnetolectric coupling at the walls. Palai et al. observed anomaly in the phonon frequency and line width in the

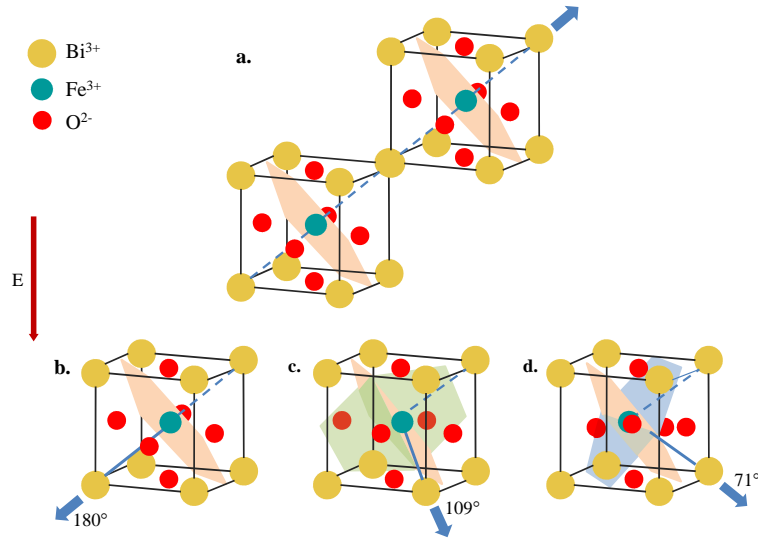


FIGURE 1.33: **a.** Orientation of the polarization relative to the antiferromagnetic plane in BiFeO₃ thin film of (001) orientation. **b.** The reversal of the polarization at 180° electric field does not change the orientation of the plane antiferromagnetic. **c.** and **d.** The reversal of the polarization at 109° and 71° causes the shift of antiferromagnetic plane, which then remains perpendicular to the polarization.(Zhao et al., 2006)

AFM-PM phase transition at around 643K, which indicates magnetoelectric coupling in the BiFeO₃ thin film. (Catalan et al., 2008)

Zeches et al. observed strong structure softness in the mixed T-R phase of BiFeO₃ thin film (Zeches et al., 2009) Then Wojdel et al. introduce structural softness terms into the regular magnetoelectric multiferroics free energy and show that structural softness results in a large enhancement of the ME response of BiFeO₃ thin film. (Wojdel & Iniguez, 2010) The further work presents that the enhancements of the linear and quadratic ME coefficients have the same macroscopic origin, namely an increase in the dielectric permittivity. (Prosandeev et al., 2011) Lately, Chen et al. succeeded in manipulating of both ferroelectric and ferroelastic orders at the T-R phase boundary of BiFeO₃ thin film and show that spontaneous magnetic moments are correlated with the local ordering parameters, which provide the possibility of electrically controlling the magnetic orientations at room temperature (Chen et al., 2012).

1.5 The type I multiferroic : Hexagonal RMnO₃

The hexagonal manganites RMnO₃ with small rare-earth ions R = Sc, Y, In, Ho-Lu are a group of materials with unusual combination of electric, magnetic and optical properties.

1.5.1 Structure

We take hexagonal YMnO_3 (h- YMnO_3) as an example, which is a well-known multiferroic compound with Curie temperature 950K and Neel temperature $T_N = 77$ K. The hexagonal structure adopted by YMnO_3 and other manganites with small R ions consists of non-connected layers of MnO_5 trigonal bipyramids corner-linked by in-plane oxygen ions (O_P), with apical oxygen ions (O_T) which form close-packed planes separated by a layer of Y^{3+} ions. Schematic views of the crystal structure are given in Fig. 1.34. (Aken & Palstra, 2001)

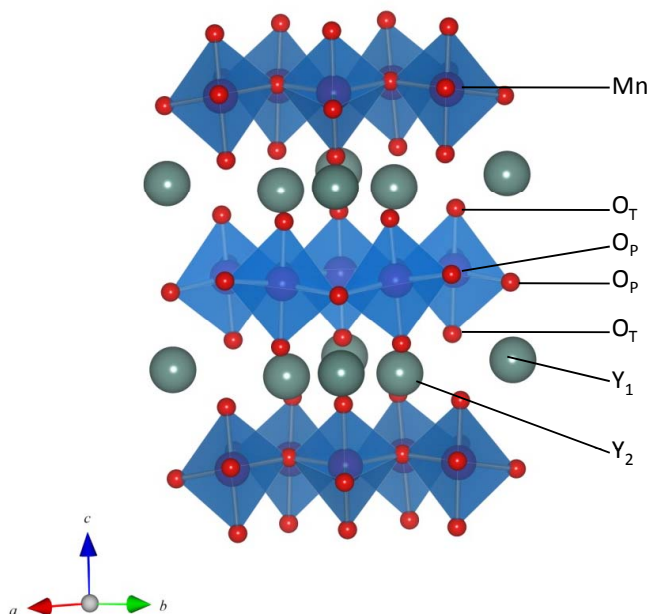


FIGURE 1.34: The crystal structure of YMnO_3 . The hexagonal structure consists of non-connected layers of MnO_5 trigonal bipyramids corner-linked by in-plane oxygen ions (O_P), with apical oxygen ions (O_T) which form close-packed planes separated by a layer of Y^{3+} ion

In contrast to conventional perovskites, h- YMnO_3 has its Mn^{3+} ions not inside the O_6 octahedra but coordinated by a five-fold symmetry (i.e. in the centre of O_5 trigonal bipyramid). Similarly, R-ions (e.g. Y ions) are not in a 12-fold but a 7-fold coordination. Consequently, the crystal field level scheme of Mn ions in these compounds is different from the usual scheme in an octahedral coordination. The d-levels are split into two doublets and an upper singlet, instead of a triplet t_{2g} and a doublet e_g in orthorhombic perovskites (Fig. 1.35). Therefore, the four d electrons of Mn^{3+} ions occupy the two lowest doublets, leaving no orbital degeneracy. Consequently, Mn^{3+} ions in these compounds are not Jahn–Teller active.

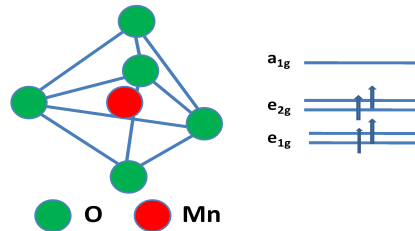


FIGURE 1.35: The structure of MnO_5 and crystal field level scheme of Mn ion, the d-levels are split into two doublets and an upper singlet.

1.5.2 Ferroelectricity properties

Early works in the 1960s established that YMnO_3 is ferroelectric with space group $\text{P6}_3\text{cm}$ below Curie temperature. (Bertaut & Mercier, 1963; E.F Bertaut, 1967) The ferroelectric polarization arises from an off-centre distortion of Mn ions towards one of the apical oxygen ions. However, careful structural analysis revealed that Mn ions remain very close to the center of the oxygen bipyramids and, thus, are definitely not the origin of ferroelectricity. First principle calculation also predicts that the off-centre distortion of Mn ions is energetically unfavourable. The main difference between the paraelectric (PE) $\text{P6}_3/\text{mmc}$ structure and ferroelectric $\text{P6}_3\text{cm}$ structure is that all ions in the PE phase are restricted within the planes parallel to the ab plane, whereas in the ferroelectric phase, the mirror planes perpendicular to the hexagonal c -axis are lost. (Aken & Palstra, 2001) The structural transition from the centrosymmetric $\text{P6}_3/\text{mmc}$ to the ferroelectric $\text{P6}_3\text{cm}$ is mainly facilitated by two types of atomic displacements. First, the MnO_5 bipyramids buckle, resulting in a shorter c -axis and the O_T in-plane ions are shifted towards the two longer Y-O_P bonds. Second, the Y ions vertically shift away from the high-temperature mirror plane, keeping the constant distance to O_T ions. Consequently, one of the two 2.8\AA Y-O_P bond length is reduced down to 2.3\AA , and the other is elongated to 3.4\AA , leading to a net electric polarization as shown in Fig. 1.36. The polarization dependent X-ray absorption spectroscopy (XAS) demonstrated that the Y_{4d} states are strongly hybridized with the O_{2p} state. (Cho et al., 2007) Neutron powder diffraction measurements also recognized the asymmetric environment of Y ions. (Munoz et al., 2000; Katsufuji et al., 2002) The above picture suggests that the main dipole moments are contributed by the Y-O pairs instead of the Mn-O pairs. This is an additional example for the A-site ions-induced ferroelectricity.

1.5.3 Magnetic structure

The spin configuration of hexagonal RMnO_3 is complex due to the two magnetic ions R^{3+} and Mn^{3+} (except Y ion). Because of these two ions, there are intraplane Mn-Mn interaction, interplane Mn-Mn interaction, R-Mn interaction, and magnetoelastic

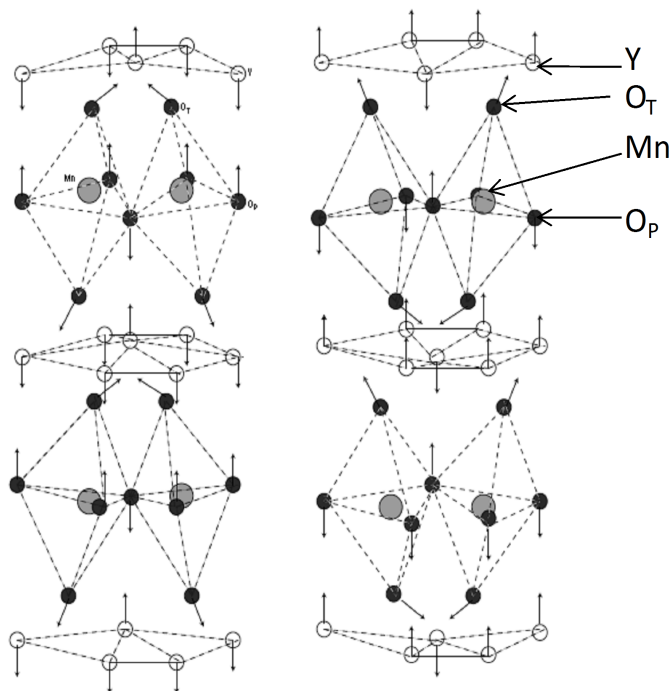


FIGURE 1.36: The crystal structure of ferroelectric YMnO_3 and the movement of Y, Mn, O ions.

coupling in hexagonal RMnO_3 with magnetic R ions which affect the magnetic order and spin excitations.

The easy plane anisotropy of Mn spins restricts the moments in the ab plane. An antiferromagnetic (AFM) order of the Mn^{3+} spins occur below the Néel temperature. The Néel temperature is in the range between 70 and 87K for $R = \text{Y, Ho, Er, Tm, Yb}$ and Lu. (Zhou et al., 2006) The neighboring spins of the close-packed Mn^{3+} ions are AFM coupled via the oxygen ions by superexchange interaction, which gives rise to frustration effects of an ideal 120° structure with space group $\text{P6}_3\text{cm}$. There are six Mn ions irreducible representations predicted by a symmetry analysis that correspond to the different magnetic structures as shown in Fig. 1.37 (Brown & Chatterji, 2006). The Mn^{3+} spins are ordered perpendicular to the c -axis, while at low temperature magnetic R^{3+} ion spins are oriented along c -axis. R^{3+} ion spins can interact among themselves and with Mn^{3+} spins. Among all hexagonal RMnO_3 compounds with $S_R \neq 0$, HoMnO_3 is the most studied material. Its magnetic structure is interesting since it shows two additional phase transition below T_N . Mn^{3+} reorientation at $T_{SR}=40\text{K}$ and AFM ordering of Ho^{3+} spins at $T_R=5\text{K}$ are observed in neutron scattering (Munoz et al., 2001a; Lonkai et al., 2002) and second harmonic generation optical experiments (Fiebig et al., 2000a,b, 2002a). The further work presents that the origin of Mn^{3+} reorientation at T_{SR} is the displacement of Mn^{3+} position in the ab plane by elastic and inelastic neutron

measurements (Fabreges et al., 2009). Both low-temperature transitions at T_{SR} and T_R are accompanied by a partial or complete ordering of Ho^{3+} ions.

In YbMnO_3 , the magnetic order of Mn^{3+} is $P6'_3c'm'$ or $P6_3c'm'$. $\text{Yb}(2)$ moments order due to the Mn molecular field but $\text{Yb}(1)$ moments order at much lower temperature through Yb-Yb interactions (Fabreges et al., 2008). Recent work observed the magnetic order of R ions ($R=\text{Er}, \text{Tm}, \text{Yb}$) at low temperature $T < 3.5\text{K}$ and in strong external magnetic field (Standard et al., 2012).

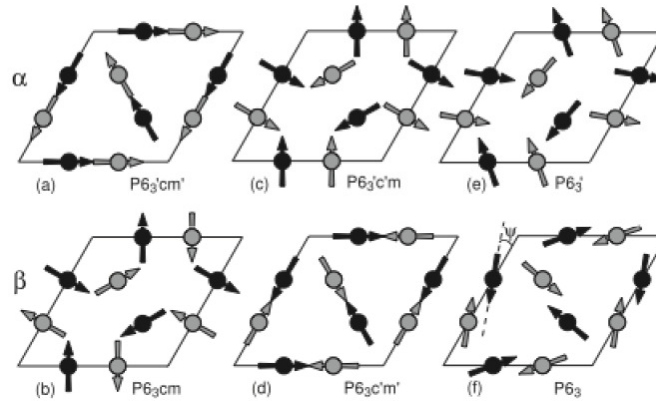


FIGURE 1.37: Six different types of magnetic ordering in hexagonal RMnO_3 . (Brown & Chatterji, 2006)

1.5.4 Spin-lattice coupling

Because the Curie temperature (around 900K) of hexagonal RMnO_3 appears far above the Néel temperature (about 80K), magnetic and dipole orders seem weakly coupled and the hexagonal RMnO_3 seems to have little magnetoelectric effect. However, evidence for a strong interplay between magnetic and ferroelectric order has been observed by dielectric constant measurements, showing anomalies at T_N . (Huang et al., 1997; Yen et al., 2005) Moreover, the thermal expansion (dela Cruz et al., 2005) and thermal conductivity measurements (Sharma et al., 2004) have also pointed out the existence of a strong spin-lattice coupling. In 2004, Litvinchuk et al. observed Raman and Infrared-active phonons in HoMnO_3 and reported one phonon mode, which modulate the Mn-Mn interaction, exhibits pronounced anomalies near the Néel temperature as shown in Fig. 1.38 suggesting the coupling of spins to lattices (Litvinchuk et al., 2004). The similar anomaly point in the phonon mode of YbMnO_3 bulk and thin film near the Néel temperature is also observed. Moreover, extensive elementary excitations researches are also conducted in YMnO_3 . Vermette et al. and Fukumura et al. observed that some phonon modes showed anomalous temperature variation at the Néel temperature, suggesting a coupling between the spin and phonon systems below

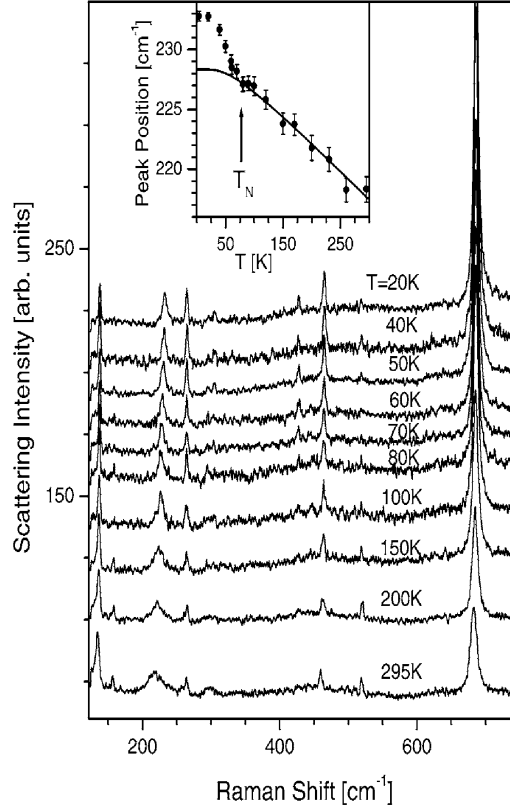


FIGURE 1.38: Raman scattering spectra of HoMnO₃ in $z(xx)\bar{z}$ polarization for various temperatures between 20 and 295 K ($\lambda_{exc} = 514.5$ nm). The inset displays the position of one of the E_2 symmetry modes versus temperature. The full curve shows the peak position expected for a standard anharmonicity-related phonon decay. T_N marks the Néel temperature. (Litvinchuk et al., 2004)

T_N . (Fukumura et al., 2007; Vermette et al., 2010)

In 2000, Fiebig et al. introduced the second harmonic generation spectroscopy to determine the magnetic symmetry of hexagonal manganites (Fiebig et al., 2000a) and directly observed coupled antiferromagnetic and ferroelectric domains in bulk YMnO₃ at 6K. (Fiebig et al., 2002b) Moreover, in hexagonal manganite HoMnO₃, Lottermoser et al. observed that, below Neel temperature 75K, ferromagnetic Ho³⁺ ordering is deliberately actived or deactivated by a static electric field, and the ferromagnetic component is controlled by the sign of the electric field (Fig. 1.39) (Lottermoser et al., 2004) The driving mechanism for the phase control are magnetoelectric interaction originating in the interplay of Ho³⁺-Mn³⁺ interaction and ferroelectric distortion.

In 2008, Lee et al. have found that YMnO₃ undergoes an isostructure transition at T_N , simultaneously producing giant atomic displacement for every atom in the unit cell. (Lee et al., 2008) Surprisingly, this happens without either soft-mode degrees of freedom or orbital degrees of freedom. The distortion origin is the displacement

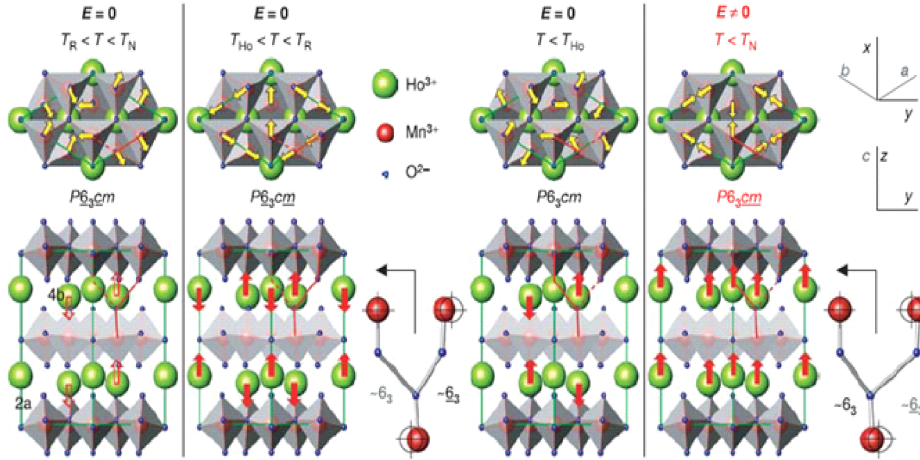


FIGURE 1.39: Magnetic structure of hexagonal HoMnO_3 . Mn^{3+} and Ho^{3+} ordering in the absence and presence of an electric field E . Arrows indicate the magnetic moments of Mn^{3+} (yellow) and Ho^{3+} (red). Open red arrows indicate that the Ho^{3+} moments are disordered, although antiferromagnetic ordering at the 4b site is symmetry allowed. Green lines, unit cell. Red lines and Y-shaped structures, inter-plane Mn^{3+} - Mn^{3+} exchange paths with straight (dashed) lines and black (grey) labels as superior (inferior) path. Cross-wires denote the frustrated $1/3$ positions of Mn^{3+} ions. Note that ferromagnetic Ho^{3+} ordering is observed exclusively when the electric field is applied. (Lottermoser et al., 2004)

of Mn^{3+} . As soon as the Mn moments start ordering below T_N , Mn position shifts drastically away from the ideal position $x=1/3$. This extremely large magneto-elastic coupling, larger by two orders of magnitude than in any magnetic materials, is primary origin of their multiferroic phenomenon.

In summary, the researches above show the existence of strong spin-lattice coupling in hexagonal RMnO_3 .

1.6 The type II multiferroics

The type II multiferroics are a new class of multiferroic, in which ferroelectricity is induced by particular magnetic orders, implying a strong intrinsic magnetoelectric coupling. However, the polarization in these materials is usually small ($10^{-2} \mu\text{C}/\text{cm}^2$). Among various type II multiferroics, perovskite manganites are the most important. For example, the type-II multiferroics with the largest polarization always belong to perovskite manganites so far, although this record has been updated year by year. In addition, almost all known physical mechanisms involved in the type-II multiferroicity, exist in perovskite manganites. In fact, most of these mechanisms were firstly revealed in perovskite manganites. Therefore, in this section, we introduce the perovskite manganites multiferroics.

1.6.1 Magnetism

In perovskite manganites RMnO_3 , there are many competing phases. When R is large (La and Pr) the magnetic ground state is A-type antiferromagnetic phase. (Wollan & Koehler, 1955) When R is very small (e.g. Ho and Tm) it becomes E-type antiferromagnetic order. (Munoz et al., 2001b) In the middle region (Tb and Dy) between the A-type and E-type antiferromagnets, the ground state is the spiral spin order, as shown in Fig. 1.40. (Goto et al., 2004)

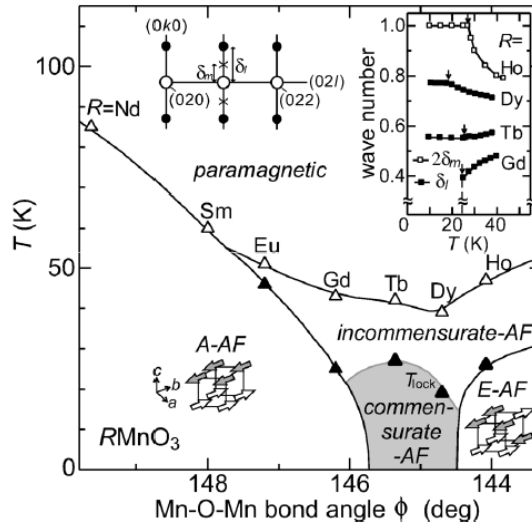


FIGURE 1.40: Experimental magnetic phase diagram of RMnO_3 . The horizontal axis stands for the decreasing Mn-O-Mn bond angle (increasing oxygen octahedra distortions) or namely the decreasing size of R. The Neel and lock-in transition temperatures are marked as open and closed triangles, respectively. Upper inset : Temperature dependencies of the wave numbers of lattice or magnetic modulation. The A-type and E-type antiferromagnetic structures are shown in their regions. The gray area is the spiral spin order state. (Goto et al., 2004)

By using the neutron diffraction technic, Kenzelmann et al. discovered that the Mn^{3+} magnetic structure of TbMnO_3 below 28 K is a transverse incommensurate spiral order, which breaks partial inversion symmetry and induces magnetoelectricity. (Kenzelmann et al., 2005) Soon after, Arima et al. confirmed the spiral order in $\text{Tb}_{1-x}\text{Dy}_x\text{MnO}_3$, which's spiral period shrinks with x as shown in Fig. 1.41. (Arima et al., 2006)

In 2003, Kimura et al. studied a two dimensional frustrated classical spin Heisenberg model with ferromagnetic nearest-neighbor exchange (J_1), ferromagnetic/antiferromagnetic next-nearest-neighbor exchange (J_3/J_2) along the a/b axis respectively. With increasing the antiferromagnetic next-nearest-neighbor exchange (J_2), the magnetic transition occurs from A-type to E-type antiferromagnet through the incommensurate structure (Kimura et al., 2003b). However, the model needs a strong J_2 to stabilize the spiral spin order and E-type antiferromagnets. Mochizuki and Furukawa extended

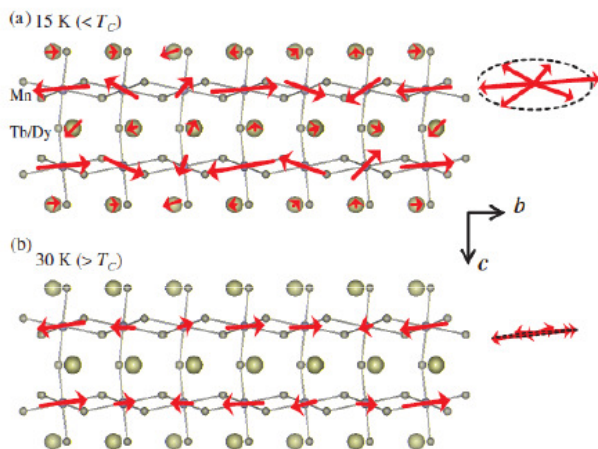


FIGURE 1.41: Schematic drawing of the magnetic moments in $\text{Tb}_{0.41}\text{Dy}_{0.59}\text{MnO}_3$ projected onto the bc plane at (a) 15 and (b) 30 K. The trajectories of the Mn spins are also shown. (Arima et al., 2006)

the frustrated classical spin Heisenberg model to three dimensional lattice, including more interaction such as the single-ion anisotropy, Dzyaloshinskii-Moriya interaction and cubic anisotropy. (Mochizuki & Furukawa, 2009) The result agrees with experiment phase diagram very well. They found that the next-nearest-neighbor spin exchanges enhanced by the orthorhombic lattice distortion induce the spiral spin order, while the spiral plane (ab vs. bc) is controlled by tuning the competition between the single-ion anisotropy and Dzyaloshinskii-Moriya interaction.

1.6.2 Ferroelectric induced by the spiral spin order

In the beginning, Kimura et al. noticed that the ferroelectric polarization in TbMnO_3 is related to the incommensurate-commensurate (lock-in) transition at 28 K, below which the magnetic modulation wave vector of Mn is locked at a constant value. (Kimura et al., 2003a)

Theoretically, Katsura, Nagaosa and Balatsky (KNB) first proposed a theory based on the spin supercurrent to explain the magnetoelectric effect in noncollinear magnets. (Katsura et al., 2005) Later, Sergienko and Dagotto proposed that the inverse Dzyaloshinskii-Moriya interaction is responsible for the polarization in RMnO_3 ($R=\text{Tb}$ or Dy). (Sergienko et al., 2006; Dzyaloshinsky, 1958; Moriya, 1960) Because of this interaction, the neighboring non-collinear spins break the inversion symmetry of the system.

However, in the KNB theory the polarization is purely electronic, while the polarization due to inverse Dzyaloshinskii-Moriya interaction is from ionic displacement. The density functional theory calculation on TbMnO_3 by Malashevich and Vanderbilt found that the polarization from electronic contribution was very weak and with oppo-

site sign against the KNB equation.(Malashevich & Vanderbilt, 2008) In 2011, Walker et al. measured the ionic displacements in TbMnO_3 and obtained high precision values on the oxygen displacement that decisively supported the microscopic model based on the DM inteaction.(Walker et al., 2011)

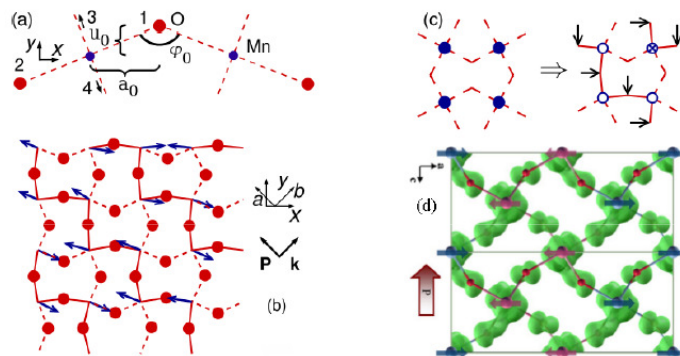


FIGURE 1.42: Ferroelectric polarization in HoMnO_3 . (a) The original (nonpolar) configuration of a Mn-O-Mn bond. (b) A Monte Carlo snapshot of the E-type antiferromagnetic phase. The ferromagnetic zigzag chain links are shown as solid lines. The displacements of the oxygen atoms are also exaggerated. (c) The local arrangement of the Mn-O bonds. Left : without any magnetic order ; Right : with the E-type antiferromagnetic order(Sergienko et al., 2006). (d) A typical charge density isosurface plot of the MnO_2 plane. Arrows denote the direction of spins. (Picozzi et al., 2007)

1.6.3 Ferroelectric induced by E-type antiferromagnet

In 2006, Sergienko, Sen and Dagotto predicted a large ferroelectric polarization driven by the spin zigzag chain in E-type antiferromagnets(Sergienko et al., 2006). In these systems, the mechanism for ferroelectricity is the exchange striction effect as shown in Fig. 1.42. Therefore, the induced polarization in orthorhombic HoMnO_3 can be greatly enhanced comparing with those spiral magnetic multiferroics. The theoretical value of polarization was estimated to be $2\mu\text{C}/\text{cm}^2$ in orthorhombic HoMnO_3 , 30 times more than TbMnO_3 . (Sergienko et al., 2006) The following density functional theory calculations further confirmed the giant ferroelectric polarization (up to $6\mu\text{C}/\text{cm}^2$) in HoMnO_3 .(Picozzi et al., 2007; Yamauchi et al., 2008). The giant ferroelectric polarization in HoMnO_3 shows dual nature : a large portion arises due to quantum mechanical effects of electron orbital polarization, in addition to the conventional polar atomic displacements. However, the experimental measurements of polarization of orthorhombic bulk RMnO_3 are much lower than the calculated result. (Lorenz et al., 2007; Ishiwata et al., 2010, 2011) A possible reason is that the electric coercive forces of E-type antiferromagnetic multiferroics are very large, which require higher poling electric fields to obtain the saturated polarizations. Moreover, Lee et al. found out that the polarization along c axis is induced by Ho-Mn exchange striction instead of Mn-Mn striction. (Lee

et al., 2011) The Ho-Mn exchange striction is supposed to be smaller than that of Mn-Mn, which could also be the reason that the experimental measurements of polarization of orthorhombic bulk HoMnO_3 are much lower than the calculated result.

Chapitre 2

Raman light scattering and samples

The Raman effect is the inelastic scattering of light. It was discovered by Sir Chandrasekhara Venkata Raman and Kariamanickam Srinivasa Krishnan in liquids and by Grigory Landsberg and Leonid Mandelstam in crystals.(Landsberg & Mandelstam, 1928; Smekal, 1923; Singh, 2002) The Raman spectrum shows characteristics of material, such as the crystal structure as well as the lattice and magnetic excitations.

2.1 The principle

When monochromatic light illuminates medium (gas, liquid, solid), the incident light can be transmitted, absorbed, reflected or scattered by the medium. There are two types of scattered light. The first type is elastic scattering light or Rayleigh scattering. In this case, the frequency of the scattered light is equal to that of the incident light. The second type is the inelastic scattering of light or Raman scattering, for which the frequencies of the incident and scattered light are different. The frequency difference is due to an exchange of energy and wavevector between radiation and matter. The energy exchange resulting in absorption (anti-Stokes process) or creation (Stokes process) of elementary excitations individual or collective (phonon, magnon, electron-hole pair etc.) in the medium.

Figure 2.1 shows a scattering spectrum (Raman intensity as a function of wave number $\omega=1/\lambda=n/c$). Elastic scattering results in a peak at $\omega= 0$. Raman scattering results in the shift of peak towards positive frequencies (Stokes) or to negative frequencies (anti-Stokes).

In this work, we are particularly interested in the vibration (phonons) and spin waves (magnon) in the Stokes Raman scattering process. Rayleigh scattering is much larger than the Raman scattering, the observation of excitations at low wavenumber then requires the use of an optical spectrometer with a high rejection. The detail of Raman spectroscopy is discussed in the following sections.

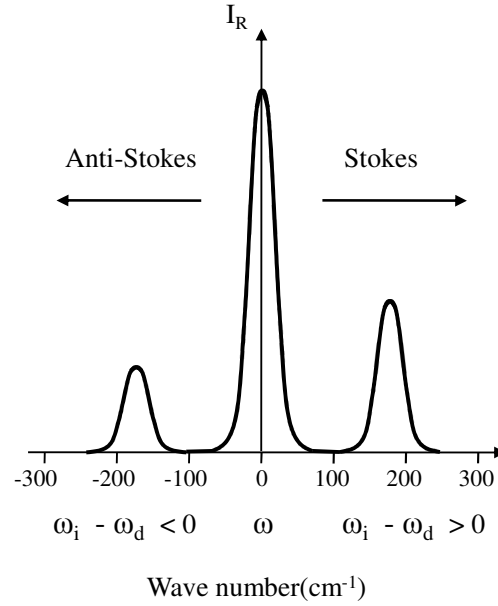


FIGURE 2.1: A Raman spectrum diagram showing the Stokes, anti-Stokes side and the elastic line (Rayleigh).

2.2 The macroscopic theory of scattering by phonon

From a macroscopic point of view, Raman scattering is observed when a crystal is excited with the electric field of light (laser beam). The electric field polarizes the medium and leads to a distortion of the electron clouds of atoms creating an electronic dipole moment. Within weak electric field, the polarization \mathbf{P} induced by the dipole moment is linearly proportional to the electric field \mathbf{E} through the susceptibility tensor χ which represents the ability of the electron cloud to be deform (Yu et al., 1997)

$$\mathbf{P} = \epsilon_0 \chi \mathbf{E} \quad (2.1)$$

The electric field of incident light and the induced polarization can be expressed in the form of plane waves :

$$\begin{aligned} \mathbf{E} &= \mathbf{E}_0 \cos(\mathbf{k} \cdot \mathbf{r} - \omega_i t) \\ \mathbf{P} &= \mathbf{P}_0 \cos(\mathbf{k} \cdot \mathbf{r} - \omega_i t) \end{aligned} \quad (2.2)$$

Electronic polarization depends on the atomic vibrations (phonons) amplitude of the atomic lattice. When this vibration has a low amplitude U , we can express the susceptibility by Taylor expansion :

$$\chi_e = \chi_0 + \left(\frac{\partial \chi}{\partial \mathbf{U}} \right)_0 \mathbf{U} \quad \text{with} \quad \mathbf{U} = \mathbf{U}_0 \cos(\mathbf{q} \cdot \mathbf{r} - \omega_0 t) \quad (2.3)$$

Therefore the induced polarization can be expressed as :

$$\mathbf{P} = \chi_0 \epsilon_0 \mathbf{E}_0 \cos(\mathbf{k} \cdot \mathbf{r} - \omega_i t) + \epsilon_0 \left(\frac{\partial \chi}{\partial \mathbf{U}} \right)_0 \mathbf{U} \cdot \mathbf{E}_0 \cos(\mathbf{k} \cdot \mathbf{r} - \omega_i t) \quad (2.4)$$

Combing these equations, we can obtain the final expression of the induced polarization :

$$\begin{aligned} \mathbf{P} = & \chi_0 \epsilon_0 \mathbf{E}_0 \cos(\mathbf{k} \cdot \mathbf{r} - \omega_i t) \\ & + \frac{1}{2} \epsilon_0 \mathbf{U} \cdot \mathbf{E}_0 \left(\frac{\partial \chi}{\partial \mathbf{U}} \right)_0 \cos[(\mathbf{k} + \mathbf{q}) \cdot \mathbf{r} - (\omega_i + \omega_0)t] \\ & + \frac{1}{2} \epsilon_0 \mathbf{U} \cdot \mathbf{E}_0 \left(\frac{\partial \chi}{\partial \mathbf{U}} \right)_0 \cos[(\mathbf{k} - \mathbf{q}) \cdot \mathbf{r} - (\omega_i - \omega_0)t] \end{aligned} \quad (2.5)$$

The first term of this equation corresponds to the Rayleigh scattering with a frequency equal to the incident light frequency ($\omega_d = \omega_i$). The second and third terms correspond to the anti Stokes scattering and Stokes scattering, respectively. For these two processes, Fig. 2.2 shows how the energy and momentum (wave vector) are conserved.

$$\hbar \omega_d = \hbar \omega_i \pm \hbar \omega_0 \quad \text{and} \quad \mathbf{k}_d = \mathbf{k}_i \pm \mathbf{q} \quad (2.6)$$

where ω_d and \mathbf{k}_d are the frequency and wave vector of the scattered radiation, ω_i and \mathbf{k}_i are those of the incident radiation, ω_0 and \mathbf{q} are those associated with the lattice vibration.



FIGURE 2.2: Conservation laws of the wave vector and the energy.

2.3 Raman tensors and selection rules

The intensity of the Raman scattering radiation can be calculated by the induced polarization mentioned in last section. The intensity depends on the polarization of the incident light (\mathbf{e}_i) and scattered light (\mathbf{e}_d). The calculated scattering light intensity is proportional to

$$I_d \propto |\mathbf{e}_i \cdot \mathcal{R} \cdot \mathbf{e}_d|^2 \quad (2.7)$$

with the Raman tensor : $\mathcal{R} = (\frac{\partial \chi}{\partial \mathbf{U}})_0$.

All the crystal symmetries are present in the tensors which are determined by group theory. The non-zero elements depends on the choice of polarizations \mathbf{e}_i and \mathbf{e}_d according to the crystal orientation. The angular variation of the scattering gives information about the symmetry of the lattice vibration named Raman selection rules. These rules are essential to determine the symmetry of Raman active phonon modes. A phonon cannot participate in the first-order scattering only if its polarization tensor can be irreducible represented. (Loudon, 1970) In this work, we detail two examples of Raman selection rules.

BiFeO₃ has a rhombohedral structure associated to the space group R3c. In this space group, the Raman tensor components can be expressed (Hermet et al., 2007) :

$$\mathcal{R}_{A_{1,z}} = \begin{pmatrix} a & 0 & 0 \\ 0 & a & 0 \\ 0 & 0 & b \end{pmatrix} \quad \mathcal{R}_{E_x} = \begin{pmatrix} c & 0 & d \\ 0 & -c & 0 \\ d & 0 & 0 \end{pmatrix} \quad \mathcal{R}_{E_y} = \begin{pmatrix} 0 & -c & 0 \\ -c & 0 & d \\ 0 & d & 0 \end{pmatrix} \quad (2.8)$$

From these tensors we can determine the selection rules for Raman scattering in BiFeO₃. Because these rules are dependent on the geometry defined by four vectors \mathbf{k}_i and \mathbf{k}_d (wave vectors of the incident and scattered light) and \mathbf{e}_i and \mathbf{e}_d , we use the Porto notation (Porto et al., 1966) to represent different polarization configurations : $\mathbf{k}_i(\mathbf{e}_i, \mathbf{e}_d)\mathbf{k}_d$.

In cross polarization $Z(XY)\bar{Z}$, $X(YZ)\bar{X}$ and $Y(XZ)\bar{Y}$, only E phonon modes are observable. A_1 modes are only obtained within parallel polarization along Z : $X(ZZ)Y$. Other polarization configurations give a mixture of the two mode types (A_1 and E).

For example, we can observe the E mode in the cross polarization $Z(XY)\bar{Z}$

$$I_d \propto |(1\ 0\ 0) \cdot \begin{pmatrix} 0 & -c & 0 \\ -c & 0 & d \\ 0 & d & 0 \end{pmatrix} \cdot \begin{pmatrix} 0 \\ 1 \\ 0 \end{pmatrix}|^2 = c^2 \quad (2.9)$$

In hexagonal structure RMnO₃ with space group P6₃cm, the Raman tensor can be expressed as :

$$\mathcal{R}_{A_{1,z}} = \begin{pmatrix} a & 0 & 0 \\ 0 & a & 0 \\ 0 & 0 & b \end{pmatrix} \quad \mathcal{R}_{E_1} = \begin{pmatrix} 0 & 0 & c \\ 0 & 0 & d \\ c & d & 0 \end{pmatrix} \quad \mathcal{R}_{E_2} = \begin{pmatrix} e & f & 0 \\ f & -e & 0 \\ 0 & 0 & 0 \end{pmatrix} \quad (2.10)$$

The A_1 phonon mode can be observed at parallel polarization $Y(ZZ)\bar{Y}$ and $Z(XX)\bar{Z}$ and E_1 mode is observed at cross polarization $Y(XZ)\bar{Y}$. E_2 are observable both at cross polarization $Z(XY)\bar{Z}$ and $Z(XY)\bar{Z}$.

2.4 The microscopic theory of scattering by phonon

The macroscopic theory does not explain the real physics underlies the process of Raman scattering. In fact, it does not explain the role of electrons in this phenomenon. The photons frequency is two orders of magnitude higher than that of phonons and thus the probability of direct interaction photon-phonon is very low. This interaction takes place thus by means of the electrons.

In the microscopic theory, the Raman scattering process contains three steps : (1) photon (ω_i, \mathbf{k}_i) absorption by the crystal, (2) creation of an optical phonon(ω_0, \mathbf{q}), and (3) emission of a scattered photon (ω_d, \mathbf{k}_d). At the beginning of the process, the crystal is in its initial state with full valence band and empty conduction band. These three stages (Yu & Cardona, 1999) are shown in Fig. 2.3.

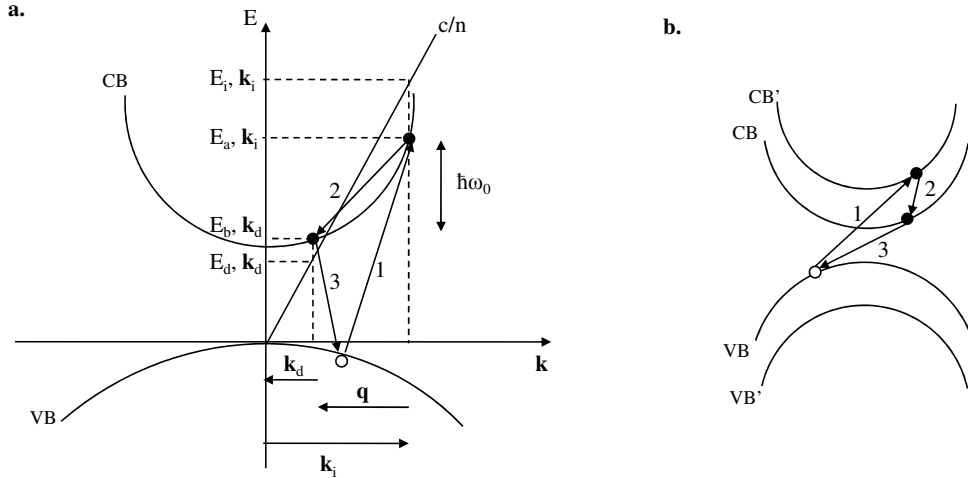


FIGURE 2.3: **a.** Phonon Raman scattering process of Stokes band (two bands process) and **b.** Interband scattering (three bands process).

Step 1 : An incident photon (energy $E_i = \hbar\omega_i$ and wavevector \mathbf{k}_i) interact with an electron to form an electron-hole. During this interaction, the electron excited by the absorbed photon jumps from the valence band to the conduction band (energy E_a and wavevector \mathbf{k}_i). The electron moves from its initial electronic state $|i\rangle$ to excited state $|a\rangle$. In the case of $E_i = E_a$, this step is a resonance Raman scattering.

Step 2 : One member of the created pair is scattered by a phonon (ω_0, \mathbf{q}). It is an intra-band scattering (Fig. 2.3 a) in which the electron (or hole) loses energy through the state $|a\rangle$ to $|b\rangle$ state. It can also be an inter-band scattering (Fig. 2.3 b). The three-bands process also bring the electron (hole) to the state $|a\rangle$.

Step 3 : The electron-hole pair recombined by emitting a photon (energy E_d and wavevector \mathbf{k}_d), where $E_d \neq E_i$. Then the electron (hole) returns to its final state $|f\rangle$.

According to the laws of energy conservation and wave vector, we obtain $E_i - E_d = \hbar\omega_0$ and $\mathbf{k}_i - \mathbf{k}_d = \mathbf{q}$.

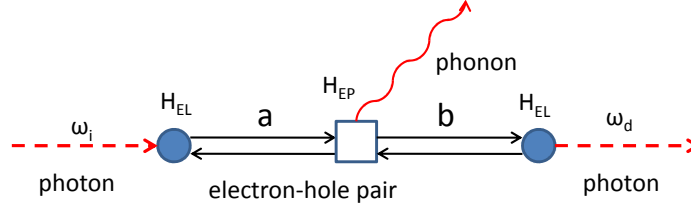


FIGURE 2.4: Feynman diagram for the scattering process that contribute to Stokes Raman scattering.

Then we try to figure out the relationship between the process and the scattering intensity. As shown in the Feynman diagrams of this process (Fig. 2.4), the step 1 and 3 can be interpreted as the electron-light interaction, the Hamiltonian is H_{EL} . The step 2 is the electron-phonon interaction, the Hamiltonian is H_{EP} . In order to solve this problem in quantitative model, adiabatic approximation is applied, which means the electron movement can immediately follow the ion movement. Therefore, the electron movement depends on the ion position and the electron equation can be reduced to a time-dependent Schrodinger equation. Nevertheless, the ion vibration around the equilibrium position instantly changes the electron energy which introduces one time-dependent component into this equation. (Ridley, 1993) This component is called the adiabatic electron-phonon interaction. However this term is so small that we can ignore it in the perturbation term. As long as all the interactions mentioned before in the Raman scattering process are weak, the scattering probability can be calculated with three order perturbation theory. The probability of the Raman scattering from initial state to the final state can be derived via the Fermi Golden Rule :

$$A_{i \rightarrow f} = \sum_{a,b} R_a R_b \langle f | \mathcal{H}_{EL} | b \rangle \langle b | \mathcal{H}_{EP} | a \rangle \langle a | \mathcal{H}_{EL} | i \rangle \quad (2.11)$$

where

$$R_a = \frac{1}{E_i - E_a + i\Gamma_a} R_b = \frac{1}{E_d - E_b - i\Gamma_b} \quad (2.12)$$

$|i\rangle$ and $|f\rangle$ are the initial and final state of energy E_i and E_f respectively. $|a\rangle$ and $|b\rangle$ represent two intermediate state with energy of E_a and E_b respectively. Γ_a and Γ_b are the damping constant.

The electron-phonon interaction Hamiltonian can be represented by the annihilation operator b_q and creation operator b_q^+ :

$$\mathcal{H}_{EP} = \sum_q [\mathcal{H}_{ep}(q)b_q + H_{ep}^*(q)b_q^*] \quad (2.13)$$

The Hamiltonian \mathcal{H}_{ep} and \mathcal{H}_{ep}^* act on the electronic part of the intermediate state $|a\rangle$ and $|b\rangle$. The operators b_q and b_q^* are applied to the vibration part of these two states and correspond to the anti-stoke and stoke process respectively. The total phonon number of the system is unstable because of the creation or annihilation of phonon. The number fluctuates over time around its average value at thermodynamic equilibrium state. The average value can be presented as $n(\omega_q)$ in the form of the Bose-Einstein probability distribution :

$$n(\omega_q) = \frac{1}{\exp(\frac{\hbar\omega_q}{k_B T}) - 1} \quad (2.14)$$

Then the electron-phonon matrix can be denoted as :

$$\langle b | \mathcal{H}_{EP} | a \rangle = \sum_a [\sqrt{n(\omega_q)} \langle b | \mathcal{H}_{ep} | a \rangle + \sqrt{n(\omega_q) + 1} \langle b | \mathcal{H}_{ep}^* | a \rangle] \quad (2.15)$$

The probability of scattering process by a phonon is obtained by summing the probability of all possible paths from the initial state $|i\rangle$ to the final state $|f\rangle$. Therefore the Raman intensity can be presented as :

$$I(\omega) \propto \sum_{q/\omega_q=|\omega|} |A_{i \rightarrow f}|^2 \quad (2.16)$$

In the stokes process, the intensity is :

$$I_s(\omega) = (n(\omega) + 1) \sum_{q/\omega_q=|\omega|} \left| \sum_{a,b} R_a R_b \langle f | \mathcal{H}_{EL} | b \rangle \langle b | \mathcal{H}_{ep}^* | a \rangle \langle a | \mathcal{H}_{EL} | i \rangle \right|^2 \quad (2.17)$$

The electron-phonon interaction Hamiltonian is :

$$\langle b | \mathcal{H}_{ep}^* | a \rangle = \int \psi_b^*(\mathbf{r})(\nabla \cdot \mathbf{U})(\mathbf{r})\psi_a(\mathbf{r})d^3r \quad (2.18)$$

with

$$\mathbf{U}(\mathbf{r}) = \sum_q \sqrt{\frac{\hbar}{2MN\omega(q)}} \nu_q(\mathbf{r}) b_q \quad (2.19)$$

where M is the total atom mass in unit cell, N is the number of unit cell in the crystal, $\nu_q(\mathbf{r})$ is the displacement field and ψ is the wave function.

2.5 The theory of scattering by magnon

Raman scattering can also probe the spin waves (magnons). Magnon is the collective excitation of the electron spin in the crystal lattice. These excitations appeared below the magnetic transition temperature. These excitations usually have smaller scattering cross section than that of phonons, and appear at lower energy. In 1966, the first Raman scattering of magnetic excitations was measured in FeF_2 . (Fleury & Porto, 1968)

The coupling of the incident light and the magnon takes place via virtual excitation of electronic states as in the phonon scattering. The two magnon light scattering is due to the exchange-scattering mechanism. (Hayes & Loudon, 1978) In this section I will describe the spin wave excitation in ferromagnets and antiferromagnets.

2.5.1 The scattering by ferromagnets

The spin angular momentum of each ion generates a magnetic moment $g\mu_B \mathbf{S}$. The Hamiltonian of ferromagnetic crystal in an applied field can be expressed as :

$$\mathcal{H} = -J \sum_{\mu, \nu} \mathbf{S}_\mu \mathbf{S}_\nu + g\mu_B B_0 \sum_{\mu} \mathbf{S}_\mu \quad (2.20)$$

where μ and ν label the magnetic ions and J is the exchange coupling for nearest-neighbor spins.

The Hamiltonian is diagonalized from spin to magnon operators and the diagonalized Hamiltonian is

$$\mathcal{H} = \sum_q \hbar \omega_q b_q b_q^\dagger \quad (2.21)$$

where b_q^\dagger is the creation operator for a magnon of wavevector q , b_q is the destruction operator. ω_q is the magnon frequency.

For one magnon process, the main mechanism for light scattering by magnons is electric-dipole coupling of light to the matter, and relies on the coupling of spin and orbital motions of the magnetic ions. As shown in Fig.2.5, the ionic ground state of spin S and zero orbital momentum L is split into $2S+1$ components by the applied field B_0 . The ion is assumed to possess an excited orbital P state with $L=1$ and the same spin S as the ground state. Spin-orbit interaction of the usual form $\lambda \mathbf{L} \mathbf{S}$ splits the excited states into three components.

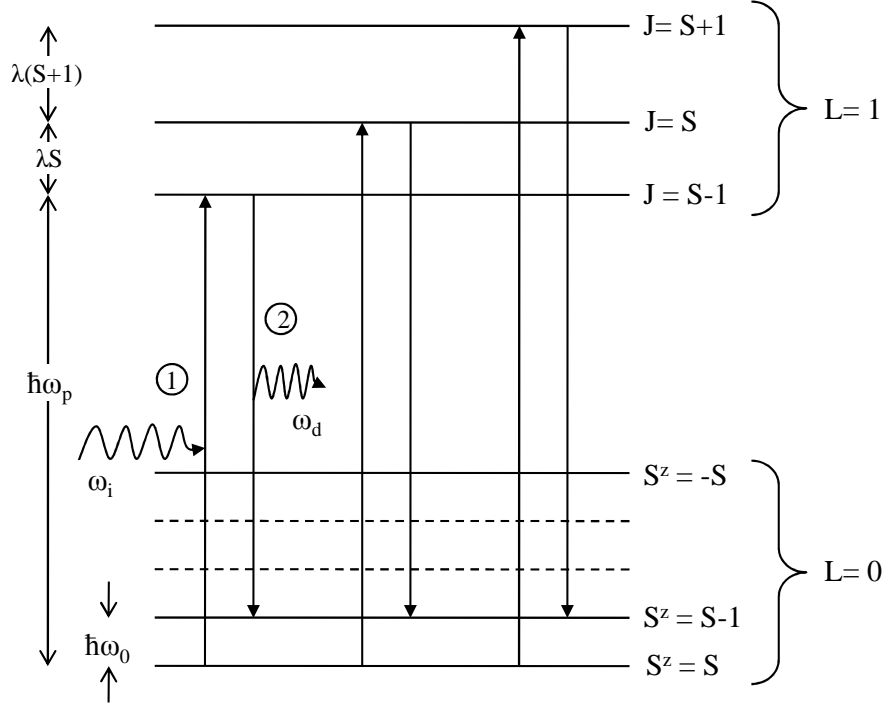


FIGURE 2.5: Electronic energy levels of a ferromagnetic crystal which shows the transition for Stokes Raman scattering

We consider the light scattering by a spin transition of a single ion from the $S^z=S$ to the $S^z=S-1$ in the ground state. The transition can proceed by the pairs of allowed electric-dipole transitions shown in Fig.2.5, where each of the three spin-orbit split excited states can act as the virtual intermediate state. An incident photon is absorbed in one transition and a scatter photon is emitted.

The total matrix element for the transition between the single-ion spin states can be represented by means of a spin Hamiltonian :

$$\mathcal{H}_{spin} = \epsilon_0 g \mu_B G \epsilon_s \times \epsilon_i \mathbf{S} \quad (2.22)$$

where ϵ_s and ϵ_i are the unit vector of electric part of the incident and scattered light respectively. G is expressed as :

$$G^2 = \frac{e^4 \lambda^2}{2\epsilon_0^2 \hbar^4 g^2 \mu_B^2} |\langle 0, 0 | \mathbf{D}^z | 1, 0 \rangle \langle 1, -1 | \mathbf{D}^- | 0, 0 \rangle|^2 \quad (2.23)$$

$$\times \left[\frac{1}{(\omega_p - \omega_i)^2} - \frac{1}{(\omega_p + \omega_s)^2} \right]^2 \quad (2.24)$$

Where \mathbf{D} is the total electric dipole moment of the atom, λ is the spin-orbit coupling parameter and $\hbar\omega_q$ is the excitation energy of the virtual intermediate states.

Therefore, the total matrix element is equal to

$$\langle S, S - 1 | \mathcal{H}_{spin} | S, S \rangle \quad (2.25)$$

The above information concerns the scattering by a spin transition on a single ion, now we discuss the scattering of a magnon. We should involve the thermal factor $N(\omega_0)+1$ and volume factor σ/V . Then we get

$$I(\omega)_s \propto (N(\omega_0) + 1) \sum_{q/\omega_q=|\omega|} |\langle S, S - 1 | \mathcal{H}_{spin} | S, S \rangle|^2 \sigma/V \quad (2.26)$$

2.5.2 The scattering by antiferromagnets

The antiferromagnetic Hamiltonian is

$$\mathcal{H}_{AM} = 2J \sum_{\mu, \nu} \mathbf{S}_\mu \mathbf{S}_\nu - g\mu_B B_A \left(\sum_{\mu} \mathbf{S}_\mu^z - \sum_{\nu} \mathbf{S}_\nu^z \right) - g\mu_B B_0 \left(\sum_{\mu} \mathbf{S}_\mu^z + \sum_{\nu} \mathbf{S}_\nu^z \right) \quad (2.27)$$

The first term is the exchange interaction between nearest neighbor spins and its positive sign is because of the spin order of two sublattices. The spins on one sublattice (label μ) point parallel to z , whereas the spins on the other sublattice (label ν) point antiparallel to z . The second term represents the effect of crystal-field and dipole-dipole forces by an anisotropy field B_A . The final term is the energy of the spins in an applied field B_0 parallel to z .

The Hamiltonian is diagonalized from spin to magnon operators and the result is :

$$\mathcal{H}_{AM} = \sum_q (E_{\uparrow q} b_{\uparrow q} b_{\uparrow q}^+ + E_{\downarrow q} b_{\downarrow q}^+ b_{\downarrow q}) \quad (2.28)$$

where

$$\begin{aligned} E_{\downarrow q} &= E_q + g\mu_B B_0 \\ E_{\uparrow q} &= E_q - g\mu_B B_0 \end{aligned} \quad (2.29)$$

$$(2.30)$$

$$E_q = \hbar\omega_k = g\mu_B B_E [(1 + B_A/B_E)^2 - \gamma_q^2]^{1/2} \quad (2.31)$$

and

$$\gamma_q = Z^{-1} \sum_j e^{iq(\mathbf{R}_i - \mathbf{R}_j)} \quad (2.32)$$

Z is the the number of nearest-neighbors. $b_{\uparrow q}^+$, $b_{\downarrow q}^+$, $b_{\uparrow q}$ and $b_{\downarrow q}$ are the the creation and destruction operators for the magnon. B_E is the exchange field.

The calculation of the single-ion intensity applies equally to a magnetic ion in a ferromagnet and an antiferromagnet. Moreover, the principle of calculation for a magnon remains the same as the ferromagnet. Therefore, the detail of calculations refers to the last section.

In the next paragraphs, I will describe the experimental devices used to measure the Raman response. By Raman spectroscopy, we can analyze the energy and moments of the matter's excitations. In multiferroics, spin wave excitations have low energies and low intensities excitations. To detect them, it is necessary to use a spectrometer which is capable to reach very low energies. It means that the spectrometer has to effectively remove the elastic scattering (Rayleigh) and keep a good luminance to observe these excitations.

2.6 The optical path

The whole optical setup is shown in Fig. 2.6. Each component is described below.

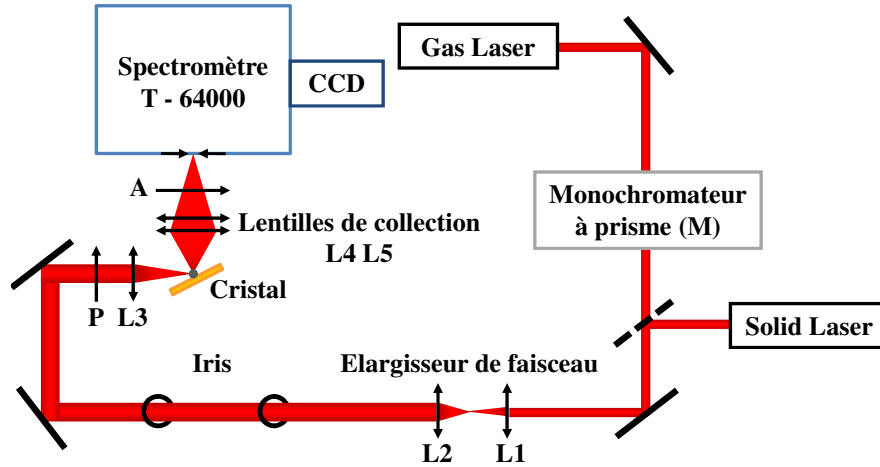


FIGURE 2.6: The optical setup.

The laser and filter

The first laser source is a gas Krypton-Argon laser (Spectra Physics) with discrete lines from blue ($\lambda = 452$ nm) to red ($\lambda = 647.1$ nm). The second laser resource is a solid laser which provide stable $\lambda = 532$ nm line. We choose different laser energy to measure BiFeO_3 (532nm) and hexagonal RMnO_3 (514.5nm, 532nm and 647nm).

The light emitted by the laser firstly passes through a prism monochromator or interference filters to remove spurious plasma produced by the laser cavity.

The focusing and collection lenses

Before being focused on the sample, the incident light passes through a beam expander consisting of two lenses 40 and 80 mm focal lengths (L_1 and L_2). This device allows us to obtain a parallel beam of 6 mm diameter. This step is very important for the good focusing of the incident light on the sample. The laser beam then passes through the two diaphragms (Iris) before reaching the objective lens (L_3). After that, the achromatic lens (L_3) with focal length $f = 100$ mm focuses the beam onto the sample placed in the chamber. The laser spot on the sample has a diameter of about 50-100 μm .

The scattered light is collected and focused on the entrance slit of the spectrometer by a system of two achromatic lenses with 60 and 260 mm focal length (L_4 and L_5).

The polarization

As mentioned before, the observation of different excitation modes requires different polarizations of the incident and scattered light. We are using two polarizers to define the polarization of the incident and scattered light. To optimize the spectrometer's response for a vertical electric field polarization of the scattered light, it is necessary to use analyzer to shift the scattered light's horizontal electric field by postpone $\lambda/2$.

2.7 Spectrometer

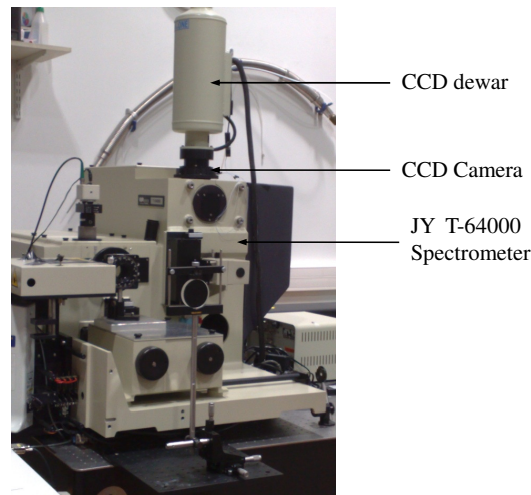


FIGURE 2.7: Jobin-Yvon T-64000 spectrometer and CCD camera.

The scattered light is collected and focused on the first slit of a triple monochromatic spectrometer Jobin-Yvon T-64000 (Fig. 2.7). This spectrometer is used in the

triple subtractive configuration, allowing us to obtain a good energy resolution and detect low-energy excitations. This spectrometer can effectively eliminate most elastic scattering light (Rayleigh) which is about 10^6 times larger than the Raman scattering light. The spectrometer consists of two stages (Fig. 2.8). A premonochromator between slits f_1 and f_3 forms the first stage. The second stage between the slit f_3 and the detector corresponds to the spectrometer. There are several confocal mirrors and three gratings in this spectrometer. Figure 2.8 shows the light path in the spectrometer.

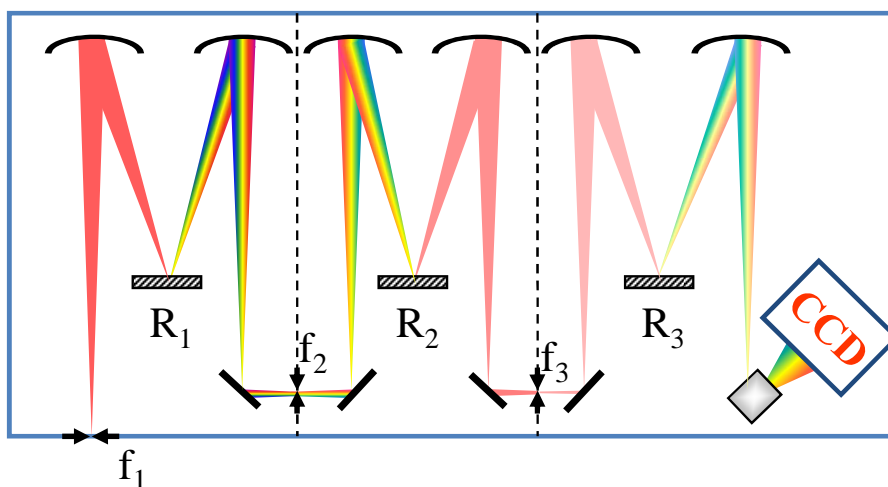


FIGURE 2.8: The optical path for the collected light in the spectrometer JY T-64000 in triple subtractive configuration.

The premonochromator

The main role of premonochromator is to eliminate the elastic light scattering. It consists of four concave spherical mirrors of 0.64m focal length and two holographic gratings. The first grating R_1 spatially separates the different components of the scattered light by law :

$$\sin\theta_d = \sin\theta_i + n\lambda$$

where i and d correspond to the angle of incident and refract light with λ wavelength. The Raman shift $\omega_0 = \omega_d - \omega_i$ (ω_i and ω_d are the frequency of the incident and scattered light). When the laser wavelength is larger ($\lambda_{red} > \lambda_{green} > \lambda_{blue}$), the reflection angle θ_d is bigger thus the spectra range of Raman light is smaller. After the first grating, the beam passes through the slit f_2 . The more this slit is closed, the more the elastic scattering light is rejected. The grating R_2 , the second grating, is used to recompose the beam which is focused on f_3 . This slit is identical to f_1 , but the difference is that the Rayleigh light has already been rejected.

The spectrometer and CCD

The spectrometer is equipped with two holographic gratings, 600 groove/mm and 1800 groove/mm; the grating can be selected according to the demand. The 1800 groove/mm grating has a better energy resolution but the signal received by each detector pixel is less than that by the 600 groove/mm grating. In our measurements, we want to improve the signals' energy resolution using 1800 groove/mm grating because of the narrow width of the excitations. The resolution order is about 0.5 cm^{-1} (0.06 meV). This stage (Fig. 2.8) is to analyze the scattered light after the elastic scattering light is filtered by the premonochromator. Finally the scattered light is collected by the multichannel detector, CCD (Charge-Coupled Device). The CCD camera is a Cryogenic Back Illuminated CCD Detector (2048x512 pixel). It is cooled by liquid nitrogen with a temperature control set to 145 K. It has excellent quantum efficiency in the visible light (close to 95% at 500 nm).

2.8 The sample chamber

To measure the excitations in our samples as a function of temperatures and magnetic field, we are using different cryostats.

2.8.1 The temperature measurements

For the temperature measurements from 10 to 300 K, we are using a helium closed cryostat as shown in Fig 2.9. It is equipped with quartz windows for optical access. The sample is glued using silver lacquer on a cold finger or a copper plate mechanically attached to the cold finger using indium foil to ensure thermal contact. The chamber is pumped to a vacuum of at least 10^{-6} mbar before cooling. The cryostat is a CS2021-DMX-20 produced by Advanced Research System (ARS). The closed circuit is composed of a compressor which exchanges the helium (with a purity of 99.9999%) and a cryocooler based on the refrigeration cycle of Gifford-McMahon. The system can cool the gas down to 4K.

The cryostat is made of a cryocooler (blue in Fig 2.9) wherein is injected pure helium gas cooled by a compressor. The gas is compressed and cooled to 4 K in the head by a piston. The 4 K helium gas cools the piston bottom. This bottom is thermally in contact with the sample carrier via a gas exchange (yellow in Fig 2.9). Indeed, the movement of the piston during the cooling cycle induces strong vibrations and thus cannot be placed in direct contact with the sample carrier. Through the gas exchange, the sample carrier can be cooled without being in mechanical contact with the piston. The temperature at the exchanger can reach 6 K. To further reduce vibration, we add buffer between the piston and chamber as shown in Fig.2.9.

There are two types of sample carrier suitable for the cryostat. One is a fixed sample carrier made of copper, the other one is fixed on a structure containing a piezoelectric motor (Attocube system) allowing it to rotate (Fig 2.10). The latter is not directly in contact with the cold finger. Copper braids (Fig 2.10) are used for connecting the rotatable sample carrier to the cold finger. The cryostat temperature control system

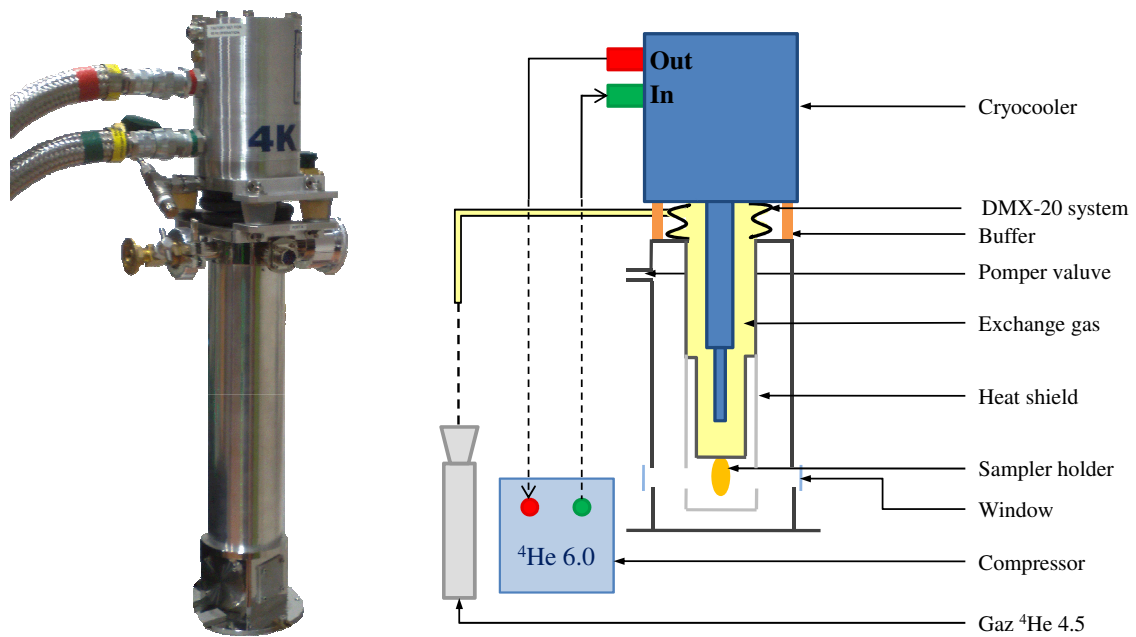


FIGURE 2.9: Photography and sketch of ARS cryostat inner structure. The cryostat is composed of a cryocooler which compressed and liquefied He gas. The cryostat is cooled to 4K through gas exchange by DMX-20 system. The heat shield is used to limit the radiation loss.

contains silicon diodes measuring the temperature and a heating resistor. Silicon diodes are placed at the heat exchanger and the cold finger. A Lakeshore temperature controller is used to ensure good temperature stabilization with an accuracy of 0.05 K.

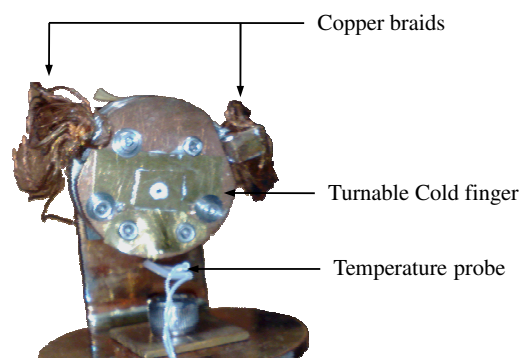


FIGURE 2.10: Automated Attocube system in the cryostat ARS allowing the rotation of samples.

2.8.2 The measurements in magnetic field

For the measurements in a magnetic field, we used a split coil Spectromag Oxford (Fig. 2.11) which can apply a static magnetic field up to 10 T. On each side of the coil there are two quartz windows for the light beam access to the samples : the outer window at room temperature of 40 mm diameter and the internal window at 4 K of a diameter of 10 mm. The coil consists of a liquid helium reservoir with a capacity of 20 L which can cool the magnet down to 4 K. To limit the evaporation of helium, a guard of 24 L of liquid nitrogen tank surrounds the He container. The two liquids are separated from the outside by a vacuum sheet. The rate of evaporation without operation of the coil and without cooling of the sample is 0.18 L/h for helium and 0.5 L/h for nitrogen. Levels of nitrogen and helium are measured and displayed by a Controller ILM211.

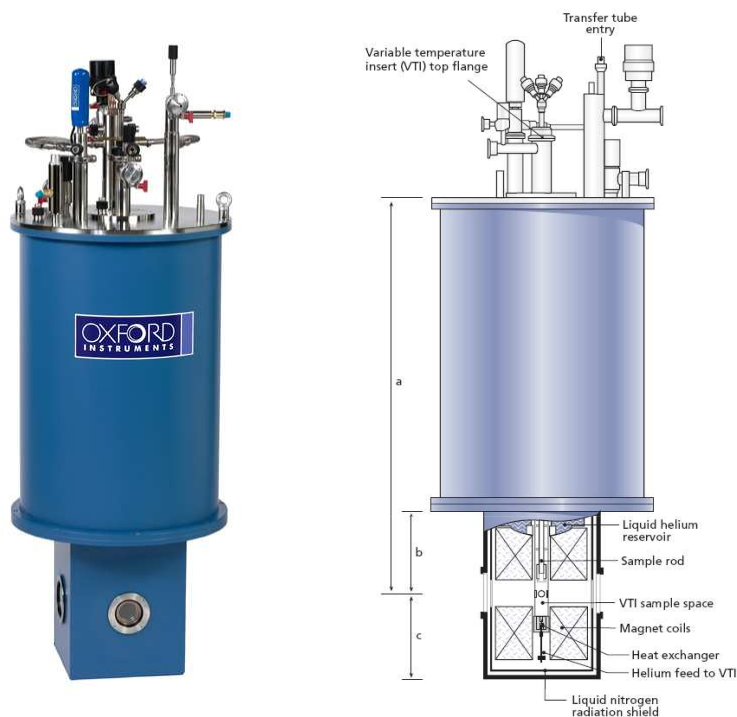


FIGURE 2.11: Photograph and sketch of the magnetic coil Spectromag Oxford.

In the center of the Spectromag Cryostat is sample space of 25 mm in diameter (Fig. 2.11). The sample is fixed on a rod that is inserted from the top of the cryostat. It allows the minimal adjustment of the sample of approximately 10 μm vertically and can turn 90 degree.

The Spectromag cryostat has a strong cooling capacity which can cool the sample down to 1.5 K. The cooling process takes place via pumping helium through a capillary between the sample space and helium container. Helium flow is controlled by a needle valve. The temperature is controlled by an ITC500 temperature controller and heating resistors at the exchanger (capillary) and the cold finger.

The magnetic field is controlled by an IPS120-10 Magnet Power Supply. A 10 T field lines radiate about 2 m from the coil in the field axis direction and 1.5 m in the direction perpendicular to the axis. Therefore, the magnet must be at least 2 m away from the table and optical spectrometer. It is then necessary to use a system to focus the laser on the sample and to collect the scattered light. We are using a 100 mm focal length lens to focus the laser beam on the sample. The collection of the scattered light is via a twin-lens system. The lens close to the coil has a 160 mm focal length. The second lens has a focal length of 600 mm and focuses the scattered beam on the entrance slit of the spectrometer.

2.9 The samples

In this section, the different samples of BiFeO₃ thin film and hexagonal RMnO₃ single crystal used for temperature and magnetic field measurement are introduced.

2.9.1 BiFeO₃ thin film

The thin film samples of BiFeO₃ we used in our work are grown by D. Sando, A. Barthelemy and M. Bibes from Unité Mixte de Physique CNRS / Thales of Université Paris-Sud at Orsay. BiFeO₃ epitaxial thin films were grown by pulsed laser deposition using a frequency tripled Nd-yttrium aluminium garnet laser. The deposition temperature and pressure were 580°C and $6 \cdot 10^{-3}$ mbar. Targets were 15% enriched in Bi.

Pulsed laser deposition is a thin film deposition technique where a high power pulsed laser beam is focused inside a vacuum chamber to a target of the material that is to be deposited. This material is vaporized from the target (in a plasma plume) which deposits it as a thin film on a substrate.

Because of the crystal parameter difference between the substrate and BiFeO₃, there is a strain force for the BiFeO₃ thin film. To gain deeper insight into the influence of strain on the spin structure, series of films on substrates spanning a strain range from -2.6% (compressive) to +1.3% (tensile) : (LaAlO₃)_{0.3}-(Sr₂AlTaO₆)_{0.7} (LSAT) -2.6%, SrTiO₃(STO) -1.6%, DyScO₃(DSO) -0.7%, GdScO₃(GSO) -0.2%, SmScO₃(SSO) +0.4%, NdScO₃(NSO) +0.9% and PrScO₃(PSO) +1.3% have been grown. Their thickness was set to 70 nm to prevent strain relaxation (except for LSAT for which it was 50 nm)

2.9.2 Hexagonal RMnO₃

Hexagonal YbMnO₃ and HoMnO₃ were synthesized by high-temperature flux growth technique by S. W. Cheong group in Rutgers University. Hexagonal YMnO₃ was synthesized by L. Pinsard of Laboratoire de Chimie des Solides in Paris-Sud University with standard floating-zone technique.

In high-temperature flux growth technique, a molten solvent or flux is used to dissolve a material or its constituents in a platinum crucible and crystallization of material is promoted either by slow cooling or by pulling on crystallographically oriented seeds.

For YMnO_3 , the feed rods were prepared by conventional solid-state reactions. Powders of high-purity MnO_2 and Y_2O_3 were mixed into the nominal molar ratio. They were ground in a mortar and calcined at 1200°C for 48 h two times. The resulting powders were compacted in the form of rods under a hydrostatic pressure of 2.5 kbar and were sintered in air at 1350°C for 12 h. Crystal growth was carried out using a floating-zone furnace equipped with double hemiellipsoidal mirrors (NEC, SC-N15HD) in which two halogen lamps were used as heating source.

Chapitre 3

Hexagonal RMnO_3 : Lattice and magnetic excitations

The hexagonal RMnO_3 compounds whose ionic radius of the rare earth is smaller crystallize in a hexagonal structure. These compounds were studied for the first time by Bertaut in the 1960s. (Bertaut & Mercier, 1963; Bertaut, E.F. et al., 1964) These initial studies helped to define precisely the crystallographic structure of this serie of compounds. In this chapter, we focus on three different RMnO_3 compounds : YbMnO_3 , HoMnO_3 and YMnO_3 . They have the same lattice structure but Yb ion radius (1.04 Å) is much smaller than Ho (1.07 Å) and Y (1.08 Å). Because of partially filled 4f shell, both Yb and Ho are magnetic ions, but Y is not magnetic ion due to empty 4f shell. Therefore , the comparison of these compounds can indicate the effect of R ions on the properties of hexagonal RMnO_3 .

3.1 Crystal structure

The space group of hexagonal RMnO_3 is $\text{P6}_3\text{cm}$ and the Wykoff positions of $\text{P6}_3\text{cm}$ space group is shown in Table 3.1. The first site (12d) is the most general and multiplicity in the term of operators numbers associated with symmetry space group ($d = 12$). These 12 positions correspond to the positions generated by the application of symmetry operations on a starting position defined by any three coordinates x , y and z . The other three sites are positioned on crystallographic symmetry elements (mirror, 3 order axis) and their multiplicity is reduced.

If the atom is positioned on an axis of n order, the multiplicity of this position is reduced to d/n . The position (4b) is located on a 3 order axis. The existence of a mirror divides the position multiplicity by 2. In the case of the position (2a), it is located on an 3 order axis coupled with a mirror. The position (6c) is located on a mirror only. In the case of hexagonal RMnO_3 , the positions for the different types of ions are listed in Table 3.2.

The crystal structure of hexagonal RMnO_3 is shown in Fig. 3.1.

RMnO_3 is formed of tilted MnO_5 bipyramids arranged in a layered type structure in the a-b plane with apical (O_1 , O_2) and in-plane (O_3 , O_4) oxygen ions. Between the

TABLE 3.1: Atomic positions associated with Wykoff positions in space group $\text{P6}_3\text{cm}$.

Site			
12d	(x,y,z)	$(\bar{y},x-y,z)$	$(\bar{x}+y,\bar{x},z)$
	$(\bar{x},\bar{y},z+1/2)$	$(y,\bar{x}+y,z+1/2)$	$(x-y,x,z+1/2)$
	(y,x,z)	$(x-y,\bar{y},z)$	$(\bar{x},\bar{x}+y,z)$
	$(\bar{y},\bar{x},z+1/2)$	$(\bar{x}+y,y,z+1/2)$	$(x,x-y,z+1/2)$
6c	$(x,0,z)$	$(0,y,z)$	(\bar{x},\bar{x},z)
	$(\bar{x},0,z+1/2)$	$(0,\bar{x},z+1/2)$	$(x,x,z+1/2)$
4b	$(1/3,2/3,z)$	$(2/3,1/3,z)$	
	$(1/3,2/3,z+1/2)$	$(2/3,1/3,z+1/2)$	
2a	$(0,0,z)$	$(0,0,z+1/2)$	

TABLE 3.2: Positions of different atoms in RMnO_3 .

R(2a)	R(4b)	Mn(6c)	O ₁ (6c)	O ₂ (6c)	O ₃ (2a)	O ₄ (4b)
$(0,0,z)$	$(1/3,2/3,z)$	$(x,0,z)$	$(x,0,z)$	$(x,0,z)$	$(0,0,z)$	$(1/3,2/3,z)$

bipyramid layers, the rare-earth ions layers are stacked along the c axis.

There are two MnO planes at $z = 0$ and $z = 1/2$ and two R planes at $z = 1/4$ and $z = 3/4$ as shown in Fig. 3.1. Rare earth ions are located on two different crystallographic sites ((4b) and (2a)) and are linked to the rest of the structure by the apical oxygen in bipyramids MnO_5 . The O ions form triangular bipyramids around each Mn and the bipyramids are connected by in-plane oxygen.

The Mn ions are arranged on a triangular structure in each plane as shown in Fig. 3.2.

Mn electronic structure

The O configuration around each Mn site has a direct effect on the Mn electronic structure. Mn^{3+} ions are d^4 configuration, and all the d orbitals are degenerate in the case of the free ion.

The addition of O in the structure can be seen as a simple way of adding point charges to atomic positions. These charges induce an electrostatic field on the Mn site. This field will act on the energy levels of different orbital and separate the degeneracy orbitals observed of the free ion. The most common example is the octahedral oxygen configuration around a Mn ion, O ions forming a square-based bipyramid whose center is occupied by Mn. In this case, the splitting of degenerate orbital is mainly dominated by electron Coulomb interaction. The $d_{x^2-y^2}$ orbital and d_{z^2} pointing in the direction of an O atom will be more strongly influenced by the Coulomb interaction than the orbital d_{xy} , d_{yz} and d_{xz} which link two O atoms. Then the orbitals are separated into two energy levels : the lower level t_{2g} involving d_{xy} , d_{yz} and d_{xz} , and the higher level e_g

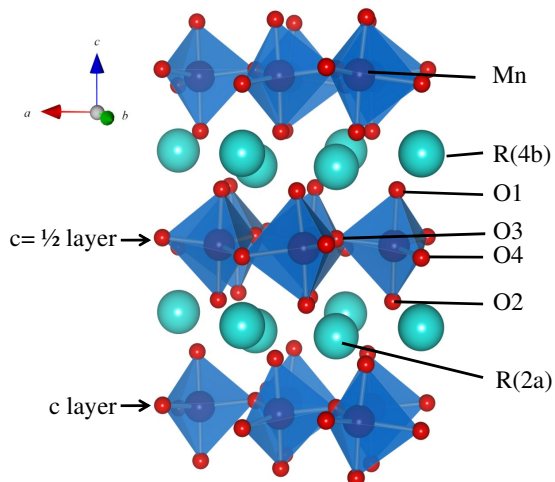
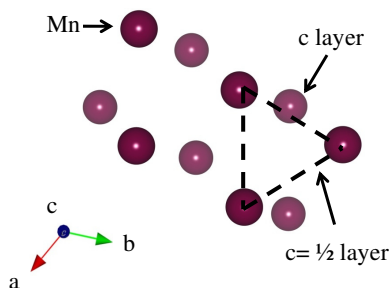
FIGURE 3.1: The structure of RMnO_3 .

FIGURE 3.2: The Mn ion structure in a-b plane.

containing $d_{x^2-y^2}$ and d_{z^2} . The corresponding electronic configuration is well known, and is usually associated with an octahedral distortion (Jahn-Teller distortion) (Jahn & Teller, 1937). This distortion is induced to minimize the system energy.

Jahn-Teller distortion presented in the orthorhombic compounds cannot be observed in hexagonal compounds. Indeed, in the hexagonal compounds, the Mn ions are not in the center of the octahedral but in a triangular bipyramid. The one missing oxygen changes the Mn orbital energy structure in the hexagonal compounds. Thus, the d_{z^2} orbital always points towards the apical O but $d_{x^2-y^2}$ orbital does not point to apical oxygen due to the triangular base. This orbital is of lower energy. The same mechanism can be applied in t_{2g} orbital level and d_{xy} orbital is of higher energy.

Therefore, the electronic structure is composed of two lower energy level, e_{1g} orbitals containing d_{xz} and d_{yz} orbitals and e_{2g} involving $d_{x^2-y^2}$ and d_{xy} , and a higher energy level a_{1g} which contains d_{z^2} orbital. In this case, Jahn-Teller distortion cannot lower the system energy any more.

3.2 Magnetic structure

The magnetic ordering in YMnO_3 , YbMnO_3 and HoMnO_3 has already been intensively investigated using unpolarized neutron powder (Fabreges et al., 2008), single crystal diffraction (Bertaut & Mercier, 1963; Bertaut, E.F. et al., 1964) and second harmonic generation (SHG) (Fiebig et al., 2000a,b). However, due to difficulties associated with similarity between possible antiferromagnetic configurations of Mn and the inability of SHG to distinguish the different magnetic sub-lattices, the magnetic structures of the different phases which occur is still controversial. (Lonkai et al., 2002; Munoz et al., 2001a) The six possible magnetic configurations of Mn moment in hexagonal compounds are shown in Fig. 3.3. For HoMnO_3 , the SHG results suggest that at $T_N=75$ K the Mn moments order to an anti-ferromagnetic arrangement with magnetic space group $P6'_3c'm$. On cooling below T_N there is evidence for two further magnetic phase transitions. Between 45 and 35 K there is a first-order transition in which the Mn spins rotate by 90° as the magnetic symmetry changes to $P6'_3cm'$ (Frohlich et al., 1998), and at $T=5$ K it is suggested that a second phase transition between nearly homometric magnetic structures with space groups $P6_3cm$ and $P6'_3cm'$ which is triggered by Ho ordering. In YMnO_3 with only a single magnetic structure $P6'_3cm'$, the phase diagram is much simpler and a single magnetically ordered phase is stable below the Néel temperature of 65 K. (Solovyev et al., 2012) In the case of YbMnO_3 , without external magnetic field, below the Néel temperature (75 K), there is only one stable magnetic structure $P6'_3c'm$. With external magnetic field, the magnetic structure becomes $P6_3c'm'$. (Fabreges et al., 2008)

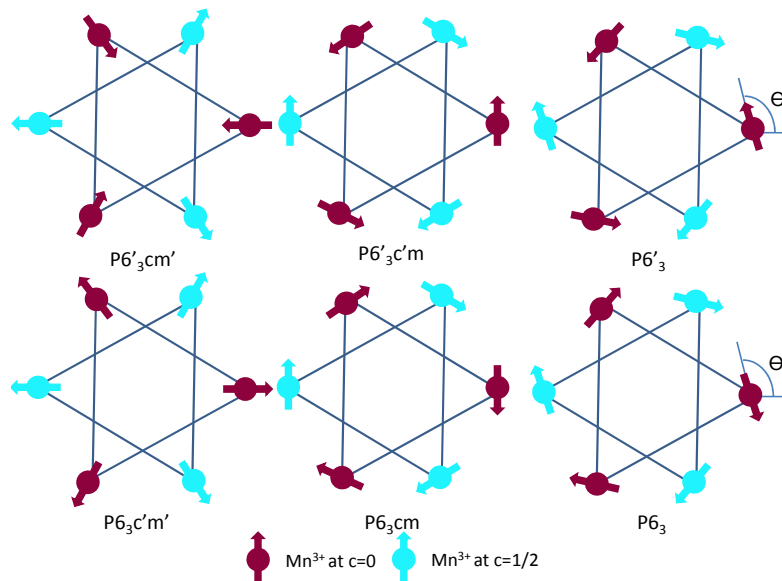


FIGURE 3.3: Six possible magnetic configurations of Mn moment in hexagonal compounds h-RMnO_3 .

The magnetic order of R moments is more intricate and difficult to determinate unambiguously, since two crystallographic 2a and 4b sites order independently. Space group symmetry allows two types of magnetic orders : along c axis or in the ab plane. The coupling between the R ions can be antiferromagnetic or ferromagnetic. The specific properties of Yb and Ho moment will be discussed in the following sections. In the case of YMnO₃, Y does not possess a partially filled 4f shell so there is no long-range ordering of Y³⁺ ions.

3.3 Hexagonal YbMnO₃

3.3.1 Lattice excitations

The phonon modes detected by Raman spectroscopy depend on the crystal symmetry which controls the matrix elements of the Raman tensor and on the incident and scattered light polarizations as mentioned in chapter 3. The irreducible representation for the normal modes in space group P6₃cm gives 60 phonon modes at the Γ point : $10A_1+15A_2+10B_1+5B_2+15E_1+15E_2$ and 38 of these modes are Raman active : $\Gamma_{Raman} = 9A_1+14E_1+15E_2$. Pure E_1 and E_2 modes are obtained in $y(zx)\bar{y}$ and $z(xy)\bar{z}$ configurations respectively. The $y(zz)\bar{y}$ and $z(xx)\bar{z}$ configurations give the $A_1(\text{TO})+E_2$ and $A_1(\text{LO})+E_2$ modes, respectively. A LO-TO splitting is expected for the A_1 and E_1 modes, as these modes may induce a nonzero dipole moment both parallel and perpendicular to the phonon propagation direction.

Figure 3.4 shows the Raman spectra of h-YbMnO₃ single crystal with $y(zx)\bar{y}$, $z(xy)\bar{z}$, $y(zz)\bar{y}$ and $z(xx)\bar{z}$ configurations. Following the Raman selection rules, we have identified 9 A_1 modes, 5 E_1 modes and 11 E_2 modes. To the best of our knowledge, the phonon modes of h-YbMnO₃ have been only reported in thin film and polycrystals. (Fukumura et al., 2007, 2009) The frequencies of the phonon modes at 10K are reported in Tab. 3.3 and compared to the previous experimental results. The attribution of the direction and sign of atomic displacements in this table is based on the previous works on the hexagonal RMnO₃ compounds. (Litvinchuk et al., 2004; Iliev et al., 1997) We have measured a small LO-TO splitting for A_1 mode as expected in this manganite family.

In Fig. 3.4, we can notice that the intensity of the A_1 mode at 678 cm⁻¹ is strong compared with the other modes. It's strong intensity is related to the motion of apical oxygen along the polarization direction and is directly connected to the polarization of YbMnO₃.

In order to analyze the effects of the phase transitions on the phonon modes, we have measured the Raman spectra as a function of temperature. Figure 3.5a shows the temperature dependence of Raman spectra and Fig. 3.5b represents the normalized frequencies over the frequency at 7K of several A_1 and E_2 modes. The phonon mode usually trend to soften due to the dilation of the unit cell when temperature increases. Except for A_1 mode at 678 cm⁻¹, all frequencies are higher in the lower temperatures. In addition to this mode, E_2 mode at 256 cm⁻¹ presents a frequency shift beyond the mean behavior of the other modes.

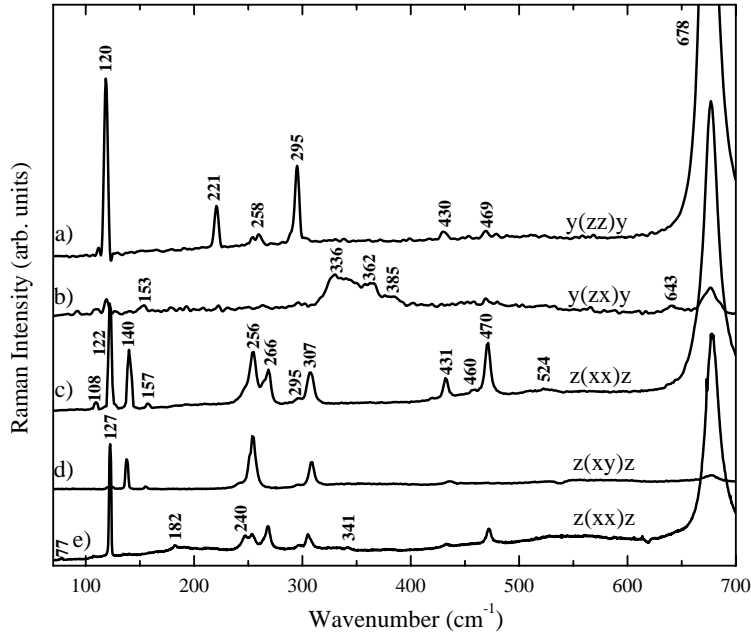


FIGURE 3.4: The Raman spectra of YbMnO_3 in different configurations. The a,b, c, and d spectra have been measured using the 514 nm laser line, and the e spectrum using the 647 nm laser line.

The frequencies of the both modes as a function of temperature are shown in Fig. 3.6. The frequency shift of E_2 mode at 256 cm^{-1} presents an abrupt change of slope around the Néel temperature in Fig. 3.6 a. Similar anomalies have been observed in the thin film and polycrystal samples of YbMnO_3 (Fukumura et al., 2009, 2007) and in the isomorphic compounds ErMnO_3 , LuMnO_3 and YMnO_3 . (Vermette et al., 2008, 2010) This mode is associated to the relative displacement of Mn and O in the a-b plane. It modulates the Mn-O-Mn bond angles in the a-b plane and thus the in-plane Mn-Mn superexchange interaction. Therefore, the hardening of the E_2 mode frequency below 80K characterizes the spin-phonon coupling in the magnetically ordered phase.

The frequency of the A_1 mode at 678 cm^{-1} in Fig. 3.6b presents a softening at the magnetic transition followed by a hardening at lower temperature. This measurement is different from the observations on YbMnO_3 polycrystal samples in which the frequency of this mode is constant down to 150K and after presents a softening down to 10K without relevant changes around T_N . This mode is related to the relative displacement of the apical oxygen ions along the c-axis. It modulates the Mn-O-O-Mn bond angles, and, hence, the Mn-Mn interaction between the adjacent Mn planes. This interaction is due to the super-superexchange paths by the way of the apical oxygen and leads to the three-dimensional magnetic ordering below T_N . Because this mode is related to the displacement of apical oxygen, it also modulate the Yb-Mn interaction along the c-axis by the superexchange path Yb-O-Mn. Therefore, the partial softening of the A_1 mode underlines the structural link between the ferroelectric and magnetic order in this compounds.

The dominant magnetic interaction is the Mn-O-Mn antiferromagnetic superex-

TABLE 3.3: Experimentally observed Raman spectra A₁, E₁ and E₂ modes frequencies (in cm⁻¹) in hexagonal YbMnO₃ and description of the atomic displacements.

Mode	Fukumura	Ours (LO/TO)	Direction of the largest displacement
A ₁		109/-	+Z(Yb ₁), -Z(Yb ₂)
	120	122/120	Rot x,y (MnO ₅)
		191/-	+Z(Yb ₁ , Yb ₂), -Z(Mn)
		247/221	X(Mn), Z(O ₃)
	262	266/258	+Z(O ₃), -Z(O ₄)
			+X, Y(O ₂), -X, Y(O ₁)
	432	432/430	+Z(O ₄ , O ₃), -Z(Mn)
	470	470/469	+X, Y(O ₁ , O ₂), -X, Y(Mn)
	520	524/-	+Z(O ₁ , O ₂), -Z(Mn)
677	678/678	+Z(O ₁), -Z(O ₂)	
E ₁		152	+X, Y(Yb ₁), -X, Y(Yb ₂)
		336	+X, Y(O ₁ , O ₂ , O ₃) -X, Y(O ₄ , Mn)
	360	362	+X, Y(O ₁), -X, Y(O ₂)
		384	+X, Y(O ₁), -X, Y(O ₂)
		643	X, Y(O ₃), -X, Y(O ₄)
E ₂		77.5	X, Y(Yb ₁ , Yb ₂ , Mn)
		127	+X, Y(Mn, O ₄ , O ₃) -X, Y(Yb ₁ , Yb ₂)
	139	140	+X, Y(Yb ₁), -X, Y(Yb ₂)
	156	157	+X, Y(Yb ₂), -X, Y(Yb ₁)
		182	
	252	256	+X, Y(Mn), -X, Y(O ₂ , O ₃)
		296	Z(Mn, O ₁ , O ₂)
	305	307	Z(O ₁ , O ₂), +X, Y(O ₄)
		341	+X, Y(O ₁ , O ₂ , O ₃ , O ₄) -X, Y(Mn)
		419	+X, Y(O ₁ , O ₄), -X, Y(O ₁ , Mn)
	457.5	+X, Y(O ₄), -X, Y(O ₁ , Mn)	

change within the plane, whereas the Mn-O-O-Mn superexchange between neighboring planes is weaker by two orders of magnitude. Nevertheless, the softening of A₁ phonon mode at 678cm⁻¹ corresponding to the movement of O₁ and O₂ ions along c-axis clearly shows that the interplane Mn-Mn and Yb-Mn interactions play an important role in the establishment of the magnetic structure of h-YbMnO₃.

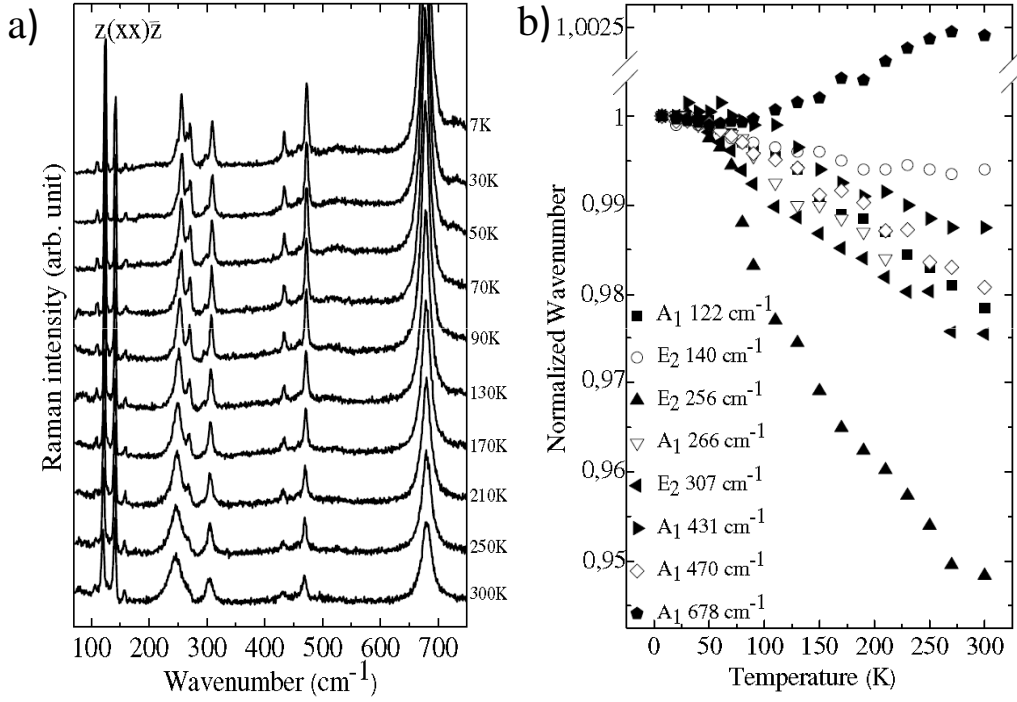


FIGURE 3.5: (a) Raman spectra of h-YbMnO₃ from 7 to 300 K in $z(xx)\bar{z}$ configuration, (b) Normalized wave numbers $[\omega(T)/\omega(7\text{ K})]$ of 5 A₁ and 3 E₂ modes as a function of temperature.

3.3.2 Magnetic excitations

Figure 3.7a shows the low frequency Raman spectra measured on h-YbMnO₃ single crystal at 7 K. Five peaks are detected : $P_1=9.8\text{ cm}^{-1}$, $P_2=23.8\text{ cm}^{-1}$, $P_3=32.8\text{ cm}^{-1}$, $P_4=41\text{ cm}^{-1}$, $P_5=53\text{ cm}^{-1}$. The inset in Fig.3.7a is a zoom in the region of the P_3 , P_4 , and P_5 peaks. No phonon mode is expected below 70 cm^{-1} . Raman scattering can probe the magnetic excitations at the center of brillouin zone (one-magnon process), crystal field excitations or magnetic excitations at zone edge (two-magnon process). Therefore, these peaks can be attributed to magnetic excitations, i. e., magnon modes or to crystal field excitations.

The origin of these excitations is discussed based on the neutron measurements. Figure 3.7b represents the spin excitation dispersions along the $\mathbf{k}=(1, 0, k)$ and $\mathbf{k}=(k, 0, 0)$ axes. (Fabreges et al., 2008) The nondispersive curve at 9.3 cm^{-1} corresponds to the splitting of the fundamental doublet of the Yb(4b) ions crystal field in the molecular field of Mn ions. The Yb(4b) ions have odd number of electrons on their outer layer and thus a double degeneracy of the fundamental state. (Kramers, 1934) The molecular field of the Mn ions creates a small Zeeman splitting and the transition can be observed. The branches starting at 24.8 and 30.6 cm^{-1} at the Γ point are associated to the magnon modes of the Mn³⁺ magnetic structure in the a-b plane. At the Γ point, the both modes correspond to the global in phase and out of phase rotation of the triangle pattern inside the basal plane. The mode at 24.8 cm^{-1} corresponds to

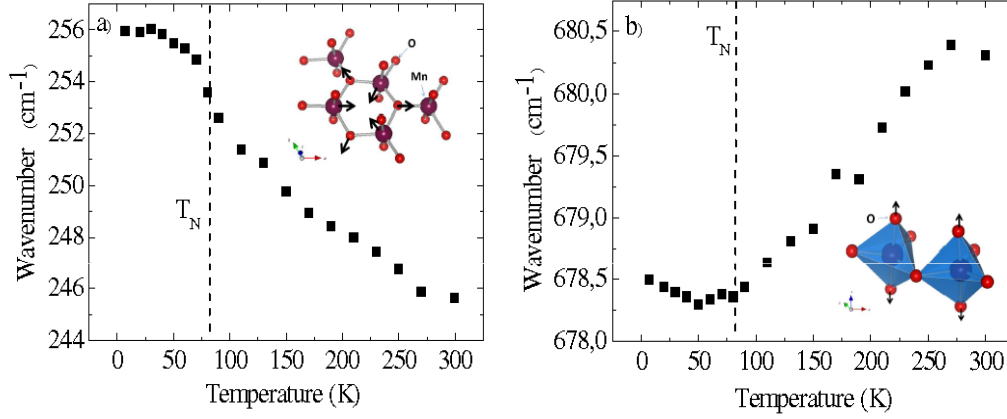


FIGURE 3.6: Wave numbers of the (a) E_2 mode at 256 cm^{-1} and (b) A_1 mode at 678 cm^{-1} as a function of temperature.

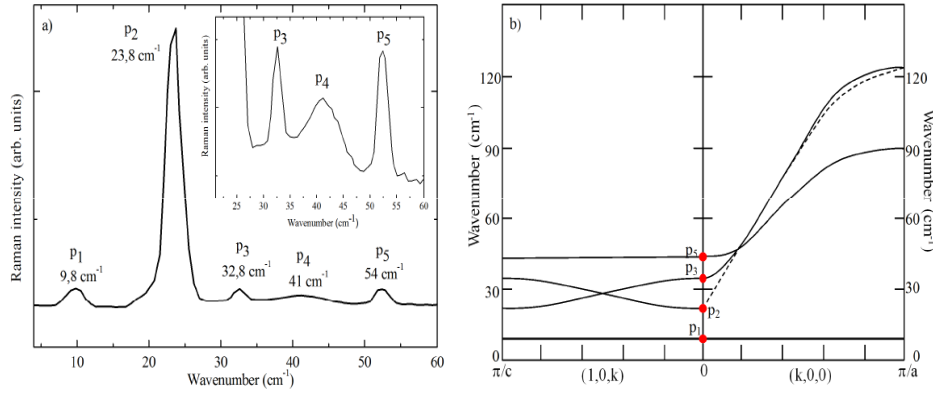


FIGURE 3.7: (a) Raman spectra of low frequency excitations measured at 7 K in $z(xy)\bar{z}$ or $y(zx)\bar{y}$ configuration ; (b) crystal field and magnon dispersions along $\mathbf{k}=(1,0,k)$ and $\mathbf{k}=(k,0,0)$.

the uniaxial anisotropy gap. The mode at 54 cm^{-1} has been associated to the Mn^{3+} spin according to Fabreges work. (Fabreges et al., 2008) This dispersion curve is quadruply degenerated along the c axis. Comparing the Raman and neutron measurements of Fig. 3.7a and Fig. 3.7b, the P_1 peak can be clearly identified to the crystal field excitation at 9.3 cm^{-1} and P_2 , P_3 , and P_5 correspond to one-magnon excitations at the center of the Brillouin zone at 24.8 , 30.6 , and 54 cm^{-1} , respectively.

The temperature dependence of the spin excitations recorded from 7 to 70K in the $z(xy)\bar{z}$ configuration is shown in Fig. 3.8a. The four peaks P_2 , P_3 , P_4 , and P_5 disappear at the Neel temperature (80k) and are thus related to the magnetic phase. The four peaks exhibit a conventional softening as the temperature is decreased. Only the P_4 peak presents a striking behavior. Its frequency is constant decreasing the temperature. This excitation will be discussed later. Fig. 3.8b shows the thermal evolution of the normalized frequency of these peaks compared to that of the Yb and Mn moments

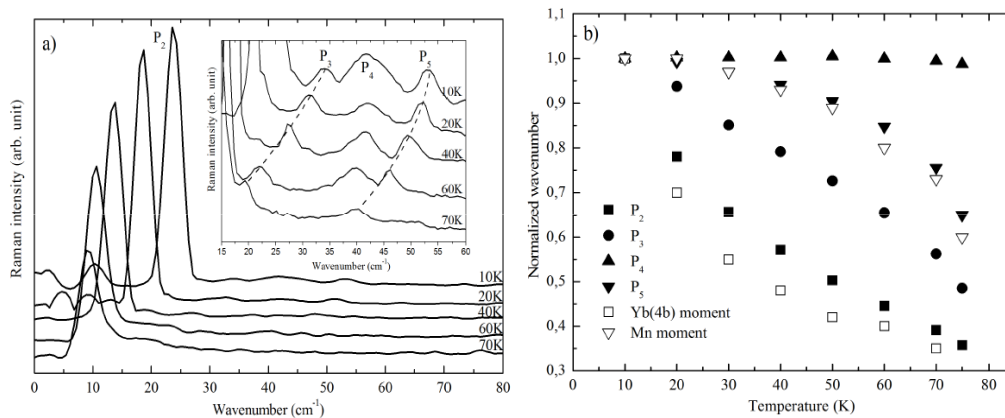


FIGURE 3.8: (a) Temperature-dependent Raman spectra in the low frequency region between 7 and 70 K. (b) Temperature dependence of normalized wave number of magnetic modes compared with the Yb and Mn moments. The Yb and Mn moment datas come from neutron powder diffraction and Mossbauer spectroscopy measurements. (Fabreges et al., 2008)

obtained from previous work. (Fabreges et al., 2008) The frequency shift of the P₅ (53 cm⁻¹) peak agrees well with the variation of the Mn moment. This magnon mode can be thus associated to the spin excitation of Mn³⁺ ions. The P₂ peak frequency shift is close to the behavior of the Yb³⁺(4b) ion moment. Remember that the P₂ peak represents the uniaxial anisotropy gap in the a-b plane. This evidence points out the role of the Yb³⁺(4b) ion and the Yb-Mn interaction on the P₂ spin excitation. The spin excitation P₃ in Fig. 3.8b presents an intermediate temperature behavior between the Yb and Mn moments that reinforce the idea of Yb-Mn coupling. All these measurements clearly show that the Mn spin orientation in the a-b plane is strongly influenced by the Yb-Mn interaction.

To shed some light on the impact of the magnetic structure on the spin excitations, we have investigated the magnetic phase diagram of h-YbMnO₃. Figure 3.9a shows low frequency Raman spectra under an external magnetic field **B** along the c axis. The frequencies of the magnetic excitations are reported as a function of the applied magnetic field in Fig. 3.9b. The degenerate magnon p₅ splits into two branches above 2 T according to its effective g-factors and following the equation : $\omega_M^\pm(B) = \omega_M(2T) \pm 1/2g\mu_B H$ where μ_B is the Bohr magneton. The frequency of the P₂ excitation is constant, whereas the P₃ mode frequency decrease above 2T and presents a crossover with the P₂ mode frequency around 7T. The P₄ peak magnetic excitation disappears at 2T. The P₅ peak splits at 2T, where one component increases in frequency and the other decreases. All these abnormal behaviors indicate that there could be a magnetic phase transition at 2 T.

The second harmonic generation measurements have shown a magnetic transition at 10K with 2T external magnetic field from the spin configuration P6₃c'm to the configuration P6₃c'm'. (Fiebig et al., 2000b) In hexagonal RMnO₃, the magnetic structure is

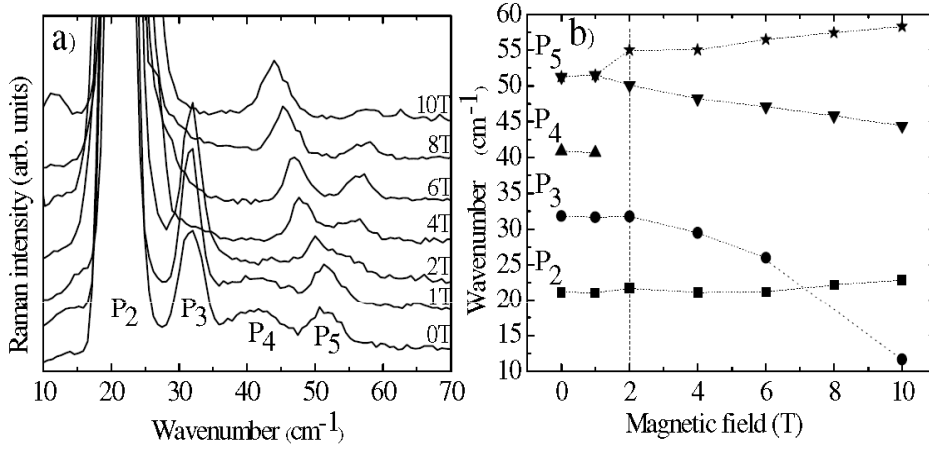


FIGURE 3.9: (a) Raman spectra obtained at 10 K in $z(xy)\bar{z}$ configuration using a magnetic field along the c axis. (b) Wavenumber of P_2 , P_3 , P_4 , P_5 excitations as a function of the magnetic field.

determined by the balance of two non-equivalent in-plane superexchange magnetic interactions, Mn-O3-Mn and Mn-O4-Mn interactions. (Kozlenko et al., 2005, 2006, 2007) Kozlenko et al. have defined a parameter :

$$s = \frac{l_{Mn-O4} - l_{Mn-O3}}{l_{Mn-O4} + l_{Mn-O3}} \quad (3.1)$$

where l_{Mn-O4} and l_{Mn-O3} are Mn-O4 and Mn-O3 bond lengths respectively. Figure 3.10 shows the dependence of the s value on the ionic radius r of the R cation, calculated from high-resolution power neutron diffraction and single-crystal x-ray diffraction data by Kozlenko et al. (Kozlenko et al., 2007; Munoz et al., 2001a, 2000; Aken & Palstra, 2001) It clearly shows that $P6'_3c'm$ or $P6_3c'm'$ are stabilized for low ionic radius (Yb), and $P6'_3cm'$ and $P6_3cm$ for higher ionic radius (Y, Ho). Therefore, in YbMnO₃, the two stable magnetic ordering are $P6'_3c'm$ and $P6_3c'm'$.

The magnon mode labeled P_3 is a spin excitation influenced by the Yb-Mn as discussed before. The strong impact of the magnetic field on the P_3 mode shows that the Mn-O-Yb superexchange is mostly involved in the phase transition.

Now, let us focus on the origin of the P_4 peak at 41 cm^{-1} . The P_4 peak only exists below the Néel temperature and thus is related to a magnetic excitation. Based on neutron measurements, this magnetic excitation does not correspond to any magnon mode at the center of Brillouin zone as shown in Fig. 3.7b. However, another mode on the dispersion curves can be proposed. The P_4 peak can correspond to a two-magnon excitation with twice the energy (around 23 cm^{-1}) of the zone edge along the $(1, 0, k)$ direction of the P_3 excitation. The experimental frequency of the two-magnon excitation is not exactly equal to twice the zone-edge magnon frequency, but a slightly lower in frequency due to interaction between pairs of spin waves created close together. The width of this peak is larger than that of one-magnon excitation and its intensity

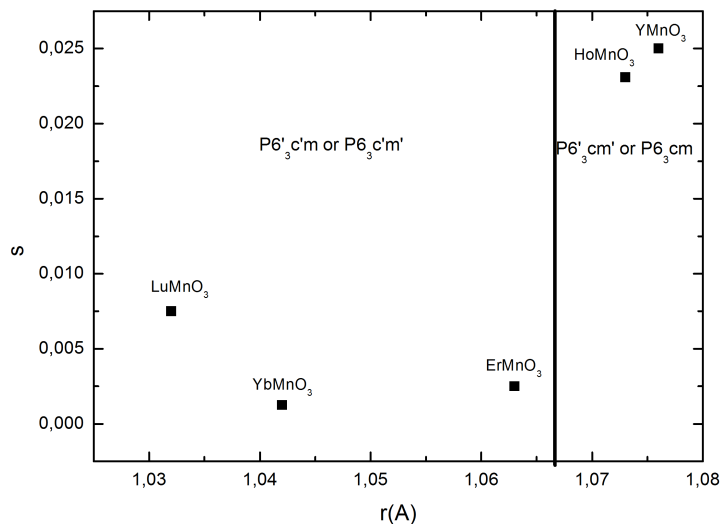


FIGURE 3.10: The magnetic structure of h-RMnO₃ as a function of rare-earth ions size.

is lower as shown in Fig. 3.7a. The two-magnon scattering arises not from the high-order of one magnon scattering mechanism but from exchange scattering mechanism that occurs only in the two-magnon scattering. (Hayes & Loudon, 1978) Because of the short range of exchange coupling, the strength of the scattering mechanism falls off rapidly with the ionic separation, and its effect is usually restricted to nearest neighbors on the opposite magnetic sublattices. The intensity of two-magnon scattering depends on the weighted state density. Due to the trigonometric factors in the weighted state density, contribution from the density of states around some critical point is suppressed depending on the polarization of the incident and scattering light. Lastly, the P_4 peak disappears at the phase transition point ($2T$). The reason is that the transition of the magnetic structure renormalizes strongly the zone edge density of states of the associated magnon mode.

3.3.3 Conclusion

We have observed 9 A_1 modes, 5 E_1 modes and 11 E_2 modes in the Raman spectra of YbMnO₃ single crystal. The E_2 mode at 256 cm^{-1} and A_1 mode at 678 cm^{-1} present an abrupt change at T_N , which indicate the coupling of lattice and spin structure. The abnormal behavior of A_1 mode clearly shows that interplane Mn-Mn interaction also plays an important role in the magnetic ordering of YbMnO₃. The magnetic excitations of YbMnO₃ are also observed and identified. The low frequency spectra of YbMnO₃ under external magnetic field show that the interplane Yb-Mn interaction drives the magnetic transition.

3.4 YMnO₃

3.4.1 Lattice excitations

YMnO₃ crystallizes in the hexagonal symmetry (P6₃cm) with lattice parameter equal to $a = 6.15 \text{ \AA}$ and $c = 11.40 \text{ \AA}$. The ferroelectric order appears below T_C about 900K. The group theoretical analysis for the Γ -point phonon modes of hexagonal (P6₃cm) YMnO₃ is the same to that of YbMnO₃.

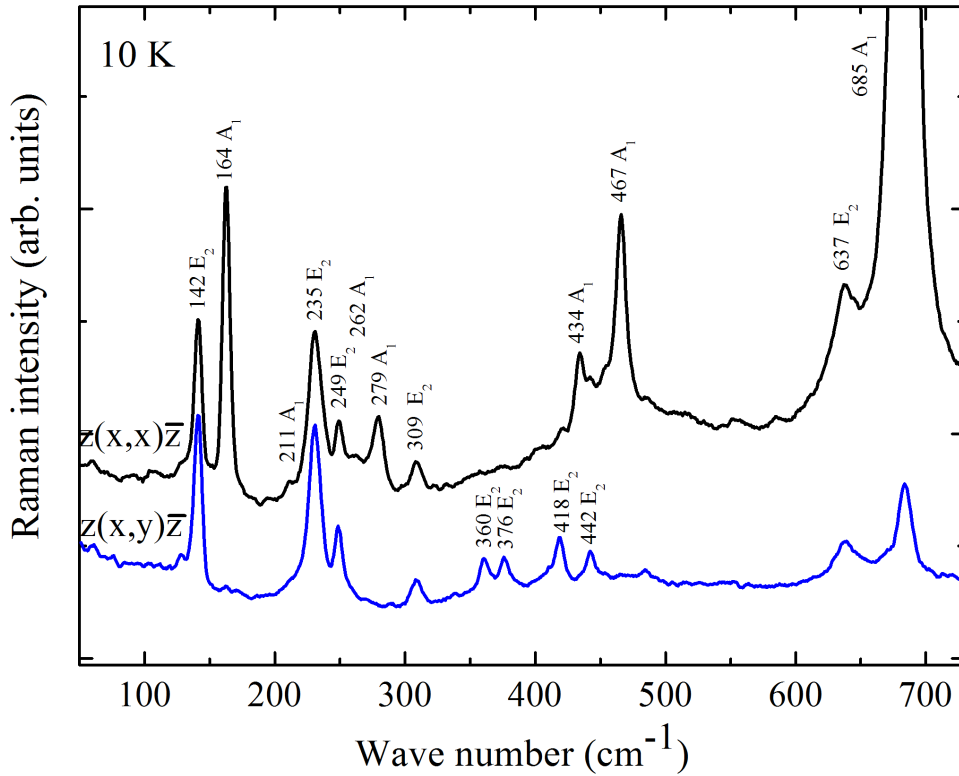


FIGURE 3.11: The Raman spectrum of YMnO₃ in $z(xy)\bar{z}$ and $z(xx)\bar{z}$ configurations.

Figure 3.11 shows the Raman spectra measured on h-YMnO₃ single crystals with $z(xx)\bar{z}$ and $z(xy)\bar{z}$ scattering configurations at 10K. We have identified 7 A₁ modes and 9 E₂ modes. The frequencies of the phonon modes are reported in Table 3.4 and compared to the previous experimental results on single crystals in addition to the associated atomic displacements.(Iliev et al., 1997)

Figure 3.12a shows the normalized frequencies of several A₁ and E₂ modes as a function of temperature. Except for the E₂ mode at 637 cm⁻¹, all frequencies are higher at lower temperature. Moreover, the shift behavior of this E₂ mode is different from that of the same E₂ mode in YbMnO₃ as shown in Fig. 3.12 b. The E₂ mode at 637 cm⁻¹ corresponds to the displacement of O3 and O4 in the a-b plane. This vibration strongly depends on the displacement of Mn³⁺ ions in the a-b plane. Because

TABLE 3.4: A₁ and E₂ mode frequencies (cm⁻¹) measured in h-YMnO₃ single crystal and description of the atomic displacements.

Mode	This work	Iliev et al. (Iliev et al., 1997)	Vermette et al. (Vermette et al., 2010)	Direction of the largest displacement (Iliev et al., 1997)
	10 K	300 K	10 K	
A ₁	164	148	161	+Z(Y ₁), -Z(Y ₂)
	211	190	244	Rot x,y (MnO ₅)
	262	257	264	+Z(Y ₁ , Y ₂), -Z(Mn)
	279	297	307	X(Mn), Z(O ₃)
	434	433	434	+Z(O ₄ , O ₃), -Z(Mn)
	467	459	467	+X,Y(O ₁ , O ₂), -X,Y(Mn)
	685	681	686	+Z(O ₁), -Z(O ₂)
E ₂	85			X,Y(Y ₁ , Y ₂ , Mn)
	142	135		+X,Y(Y ₁), -X,Y(Y ₂)
		215		+X,Y(O ₂ , Mn), -X,Y(O ₁ , O ₃)
	235		231	Z(Mn, O ₂ , O ₁)
	249			Z(Mn, O ₁ , O ₂)
	309	302		Z(O ₁ , O ₂), +X,Y(O ₄)
	376		357	+X,Y(O ₁ , O ₂ , O ₃ , O ₄), -X,Y(Mn)
	418			+X,Y(O ₁ , O ₄), -X,Y(O ₂ , Mn)
	442		441	+X,Y(O ₄), -X,Y(O ₁ , Mn)
	637			X,Y(O ₃ , O ₄)

of the triangular plane structure, the ideal position of Mn³⁺ ions in a-b plane is at the critical threshold 1/3 (the parameter x is used to represent the Mn³⁺ ions position). For YbMnO₃ and HoMnO₃, the parameter x is smaller than 1/3, but in the case of YMnO₃, x is bigger than 1/3, which means the displacement direction of Mn³⁺ ions in YMnO₃ is opposite to that in HoMnO₃ and YbMnO₃. This different displacement direction strongly affect the position of O3 and O4 in the a-b plane which finally may lead to the different shift behavior of the E₂ mode at 637 cm⁻¹ as a function of temperature.

The A₁ mode at 164 cm⁻¹ and E₂ mode at 235 cm⁻¹ also present beyond the mean behavior of the other modes with a change of the slope around the Néel temperature. The A₁ mode at 164 cm⁻¹ trends to harden at the magnetic transition followed by a softening at lower temperature. This mode is related to the relative displacement of the apical yttrium ions along the c axis. The result agrees with the measurement of the lattice parameters using high-resolution neutron diffraction which shown that the

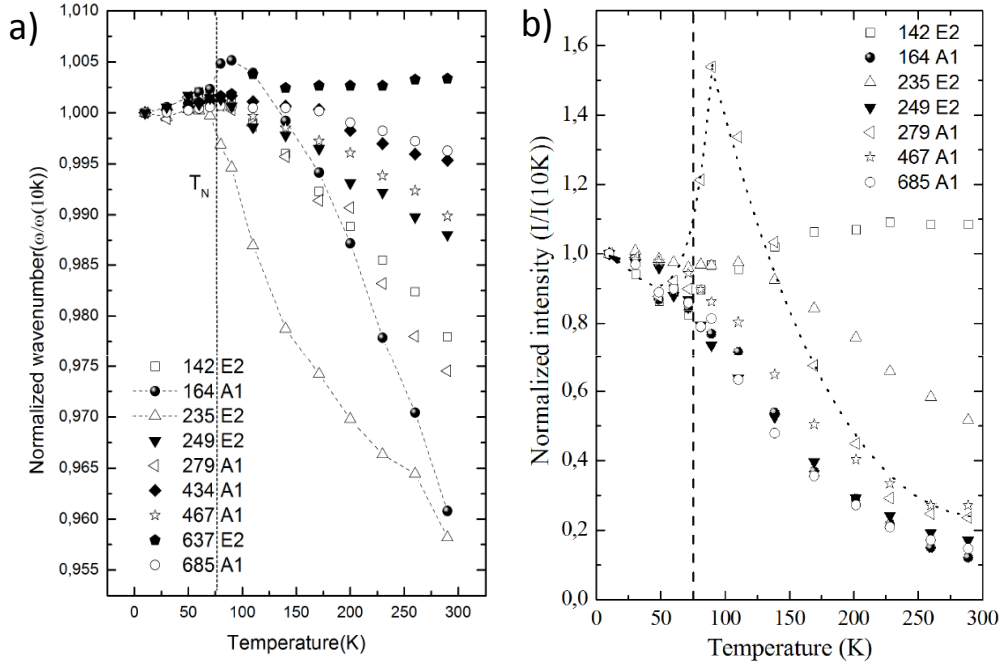


FIGURE 3.12: a) Normalized wavenumbers ($\omega(T)/\omega(10K)$) of several A₁ and E₂ modes as a function of temperature, (b) Normalized intensities ($I(T)/I(10K)$) of several A₁ and E₂ modes as a function of temperature.

position of Y(4b) ion increased from 0.270 Å to 0.280 Å and that of Y(2a) position increased from 0.230 Å to 0.232 Å. These displacements at the Néel temperature leads to the shift behavior of A₁ mode at 164 cm⁻¹. The origin of the displacement of Y ions is still unclear. The possible reason is that huge displacement of Mn³⁺ ion leads to the shift of Y³⁺ by lattice coupling to magnetic excitation.

The E₂ mode at 235 cm⁻¹ corresponds to the displacement of Mn³⁺ and two oxygen ions at the apical position along the c-axis. The anomaly shift behavior of this mode clearly shows the impact of interplane Mn-Mn interaction on the magnetic structure of YMnO₃. The interplane Mn-Mn interaction is conducted by the Mn-O-O-Mn path along the c-axis. Thus the displacement of Mn and O atoms along c-axis modifies the interplane Mn-Mn interaction. The same influence of interplane Mn-Mn interaction are also reported in other hexagonal RMnO₃ compounds. (Fukumura et al., 2009; Vermette et al., 2008) The anomaly behavior of this mode at Néel temperature proved that even through the interplane Mn-Mn interaction is weaker than inplane Mn-Mn interaction, it still play an important role in the magnetic ordering of RMnO₃.

In Fig. 3.12b the intensity of the A₁ mode at 279 cm⁻¹ dramatically increases around T_N and then decreases with increasing temperature. Its intensity curve is different from that of other modes. This mode is associated to the displacement of Mn³⁺ ions in the a-b plane. It has been shown that at T_N , h-YMnO₃ undergoes an isostructural transition with exceptionally large atom displacement. (Lee et al., 2005) In particular,

the displacement of the Mn ions is about 0.01 Å which is comparable to the value reported for prototype ferroelectric compounds. The Mn ions shift away from the ideal position of $x=1/3$ and the in-plane Mn-Mn interaction is modified. Due to the shift of Mn ions, the Mn-O bonds lengths are no more equivalent (Mn-O₃ bond length is longer than that of Mn-O₄ bond) which leads to the strong magnetoelastic coupling observed at T_N . Therefore the anomaly in the A₁ mode intensity around 80K characterizes this huge atomic shift.

3.4.2 Magnetic excitations

Figure 3.13a shows the magnon dispersion along the $\mathbf{k}=(0,0,k)$ and $\mathbf{k}=(k,0,0)$ axes. (Kadlec et al., 2011; Petit et al., 2007) Three spin waves branches are observed. Two branches degenerated in 43 cm^{-1} at the magnetic zone center that correspond to the in-plane fluctuations. (Petit et al., 2007) At the zone edge, the energy of these two branches are 80 and 130 cm^{-1} respectively. They are associated to the spin excitations of the Mn³⁺ magnetic structure in the a-b plane. At the Γ point, they correspond to the global rotations of the 120° pattern inside the a-b plane. The third dispersion branch has a zone-center energy around 20 cm^{-1} and corresponds to the out-of-plane spin fluctuation. This mode is related to the uniaxial anisotropy gap. Figure 3.13b shows the low frequency Raman spectra of h-YMnO₃ single crystal at 10K. Three peaks are detected : $P_1 = 24 \text{ cm}^{-1}$, $P_2 = 43 \text{ cm}^{-1}$, and $P_3 = 36 \text{ cm}^{-1}$. Combining the neutron and Raman measurements in Fig. 3.13 a and b, the P_1 and P_2 peaks correspond to one-magnon excitations at the center of Brillouin zone at 24 and 43 cm^{-1} and associated to the out-plane and in-plane spin fluctuations, respectively. The P_3 peak cannot be identified to one excitation at center of Brillouin zone.

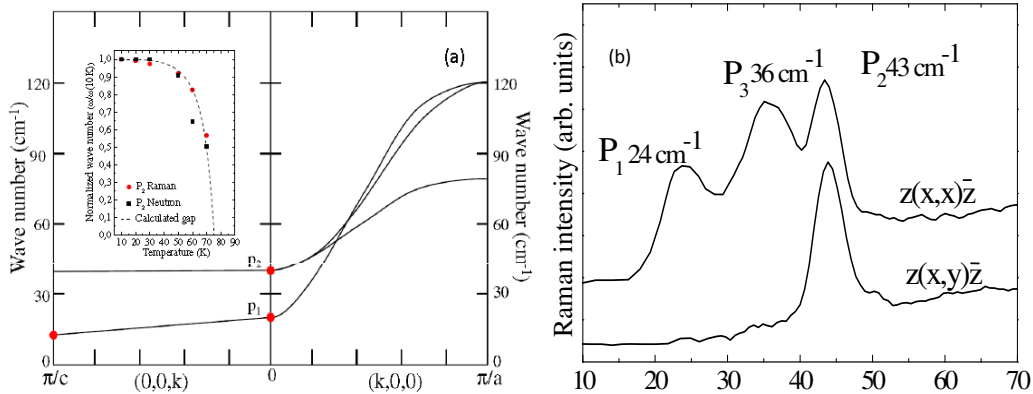


FIGURE 3.13: (a) Magnon dispersion along the $\mathbf{k}=(0,0,k)$ and $\mathbf{k}=(k,0,0)$ axes. (Kadlec et al., 2011; Petit et al., 2007) (b) Raman spectra of low frequency excitation at 7K in $z(xy)\bar{z}$ and $z(xx)\bar{z}$ configurations. The inset shows the temperature dependence of normalized wave-number of the magnetic mode at 43 cm^{-1} compared with the planar spin gap measured by the neutron spectroscopy. The dashed line is the calculated value of the inplane gap using $E_{gap} = 2S\sqrt{DJ_{in-plane}}$.

The temperature dependence of the normalized P₂ peak frequency from 10 to 70K in the $z(xy)\bar{z}$ configuration is shown in the inset of Fig. 3.13a. The planar spin gap energy measured by neutron scattering and the calculated energy gap are also presented in this figure. The gap energy associated with the planar anisotropy is given by : $E_{gap} = 2S\sqrt{DJ_{in-plane}}$ at the Γ point where $D=0.056 \text{ cm}^{-1}$ and $J_{in-plane} = 92.3 \text{ cm}^{-1}$. (Sato et al., 2003) The theoretical result and the experimental measurements are in good agreement. Therefore, the P₂ corresponds to the in-plane anisotropy.

To shed some light on the impact of magnetic field on the spin excitations, we have investigated the magnetic phase diagram of h-YMnO₃. The low frequency Raman spectra of h-YMnO₃ and the frequencies of the magnetic excitations as a function of the external magnetic field are shown in Fig. 3.14 a and b respectively. The frequencies of the P₁ and P₃ excitations are constant, whereas the P₂ peak splits between 4 T and 6 T, where one component increases in frequency and the other decreases. This mode is associated with the in-plane anisotropy gap. In h-RMnO₃ (R=Ho, Er, Tm, Yb) a reordering of the magnetic structure have been observed for different values of the applied magnetic field associated with the antiphase rotation of the Mn³⁺ spins.(Fiebig et al., 2000b) H-YMnO₃ (h-ScMnO₃ or h-LuMnO₃) has a complete 4f shell and therefore doesn't display an antiphase rotation of the Mn³⁺ spins when a magnetic field is applied. Thus in h-YMnO₃, no magnetic ordering transition is expected with the magnetic field. In an external magnetic field above 4 T along the c-axis, the doubly-degenerate magnon splits into two branches according to its effective g-factors and following the equation : $\omega_M^\pm(B) = \omega_M(4T) \pm 1/2g\mu_B H$ where μ_B is the Bohr magneton. The fit of the magnon splitted frequencies gives a g-factor equal to 2.10 ± 0.1 . This value is close to the g-factor of the Mn³⁺ ions $g_{Mn} = 2$. Since the Y³⁺ ion has a zero spin, the g-factor is determined by the Mn-Mn interaction.

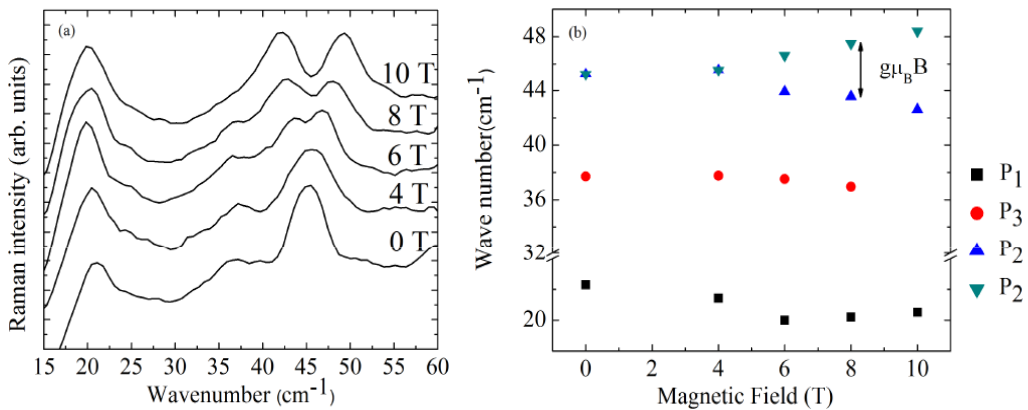


FIGURE 3.14: a) Raman spectra obtained at 10K in $z(xy)\bar{z}$ configuration using a magnetic field along the c axis, b) wavenumber of P₁, P₂ and P₃ excitation as a function of the magnetic field.

Now we can come back to the P₃ peak at 36 cm^{-1} as shown in Fig. 3.13 b. Based on

neutron measurements, this magnetic excitation does not correspond to a one magnon mode at the center of the Brillouin zone. To explain the origin of this excitation peak, several scenarios can be proposed :

(1) The peak might be associated with a crystal field electronic transition of the Y^{3+} ions. However, since Y^{3+} ($^1\text{S}_0$) has a complete $4f$ shell and zero spin, its compounds should not have any Y-related crystal field electronic transitions.

(2) It might be an electromagnon, an excitation arising from the hybridization between spin waves and phonon modes.

(3) The peak at 36 cm^{-1} could be associated to the opening of a gap in the phonon dispersion as observed in the neutron measurements. (Petit et al., 2007)

(4) It can be associated to a two magnons excitation with twice the energy (around 16 cm^{-1}) of the zone edge along the $(0,0,k)$ direction.

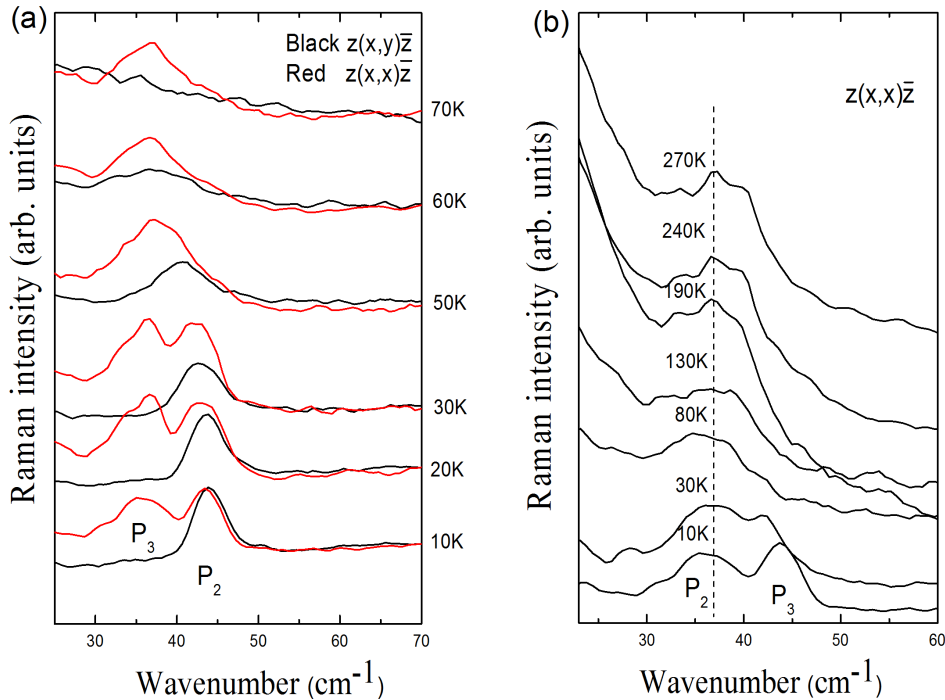


FIGURE 3.15: a) the low frequency Raman spectra of YMnO_3 in $z(xy)\bar{z}$ and $z(xx)\bar{z}$ configuration. b) Raman spectra of spin excitations from 10K to 270K in $z(xx)\bar{z}$ configuration.

Considering the second scenario, polarized inelastic neutron scattering measurements have reported the observation of hybrid Goldstone modes in $h\text{-YMnO}_3$. (Pailhes et al., 2009) This hybrid modes called electromagnons result from the coupling between spin and lattice excitation. This mode was observed around 40 cm^{-1} below T_N in non-spin-flip channel which provides the signal of nuclear, so this mode is a magnon excitation with a dipole activity. In the Raman experiments, this hybrid mode thus should be observed at the same energy. Two peaks (P_3 at 36 cm^{-1} and P_2 at 43

cm^{-1} are observed around 40 cm^{-1} . The electromagnon is sensitive to the polarization of light, but P_2 is observed using both configuration and can not be attributed to hybridized mode. Moreover, no electromagnon is expected above T_N , but P_3 peak can be observed at higher temperature as shown in Fig. 3.15b. Therefore, P_3 can not correspond to an electromagnon.

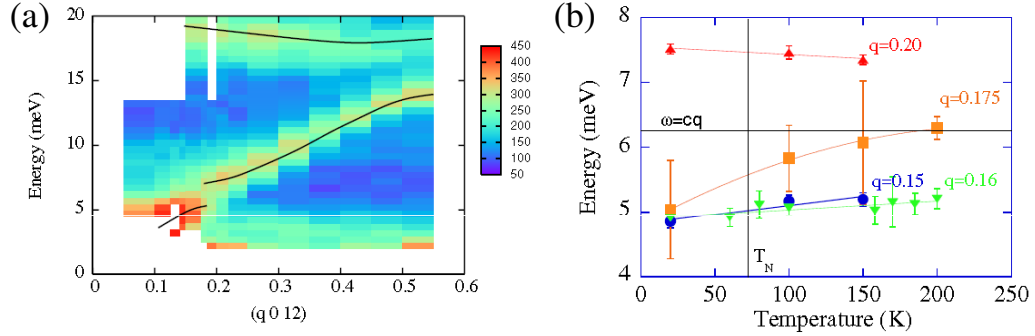


FIGURE 3.16: a) Color mapping of the neutron intensity of $YMnO_3$ obtained as a function of energy transfer and wavevector along $(q,0,12)$ at 18K, b) evolution of acoustic the phonon energy as a function of temperature for the different q -values : upward triangles, squares, circles and downward triangles correspond, respectively, to $q=0.2$, 0.175 , 0.16 and 0.15 .

Let us discuss the 3rd scenario. In previous work, (Petit et al., 2007) a gap in the transverse acoustic phonon mode dispersion curve was observed in $YMnO_3$ by neutron scattering measurement as shown in Fig. 3.16 a. The gap does not open at the zone-center, the dispersion are flat at the gap and by the phonon process it is still possible to observe it in Raman scattering. The energy of opening gap is around 40 cm^{-1} . P_3 peak is around 40 cm^{-1} which might be associated to this gap. Nevertheless, in the Raman scattering, to observe this gap it should be two-phonon excitation whose frequency should be 80 cm^{-1} instead of 40 cm^{-1} . Moreover, as shown in Fig. 3.16b which presents the temperature behavior of the gap energy, the gap measured by neutron scattering disappear when temperature is higher than 200K. In contrast, the P_3 peak can be observed even at 270K. Therefore the P_3 peak cannot be attributed to the opening gap in the acoustic phonon dispersion curve.

The last scenario associates the P_3 peak to a two-magnon excitation with twice the energy (around 16 cm^{-1}) of the zone edge along the $(0,0,k)$ direction as shown in Fig. 3.13 a. The diffraction experiments in hexagonal $RMnO_3$ indicated that magnetic 2D short-range order up to temperatures of 150K and SQUID (superconducting quantum interference device) magnetometry shows the short-range order up to at least 250 K. (Lonkai et al., 2003; Demmel & Chatterji, 2007) Our Raman scattering measurement shows that the P_3 peak survives up to 270K. Moreover, due to the exchange scattering mechanism, two-magnon excitation corresponds to the short-range magnetic structure. This explains the reduced sensitivity to the magnetic transition temperature and external magnetic field. Therefore, we attribute P_3 peak to a two-magnon excitation, but it is unusual to observe a persistent spin wave around room temperature.

3.4.3 Conclusion

7 A₁ modes and 9 E₂ modes are observed in the Raman spectra of YMnO₃ single crystal. Two A₁ modes (164 and 279 cm⁻¹) and one E₂ modes at 235 cm⁻¹ present abrupt change around T_N which shows the coupling of spin and lattice ordering. Three low energy excitations are observed. The peak at 43 cm⁻¹ corresponds to the in-plane anisotropy and the peak at 24 cm⁻¹ are attributed to out-plane spin fluctuation. The peak at 36 cm⁻¹ is identified to two-magnon excitation which can be observed at 270 K (much higher than T_N around 75K) which indicates the spin-liquid state in YMnO₃ single crystal.

3.5 HoMnO₃

3.5.1 Lattice excitations

Figure 3.17 shows the Raman spectra measured on h-HoMnO₃ single crystals with z(xx) \bar{z} and z(xy) \bar{z} scattering configurations. We have identified 6 A₁ modes and 5 E₂ modes. The frequencies of the phonon modes at 10K are reported in Table I and compared to the previous experimental results on single crystals in addition to the associated atomic displacements. (Litvinchuk et al., 2004)

TABLE 3.5: A₁ and E₂ mode frequencies (cm⁻¹) measured in h-HoMnO₃ single crystal and description of the atomic displacements.

Mode	This work	Litvinchuk et al. (Litvinchuk et al., 2004)	Direction of the largest displacement (Litvinchuk et al., 2004)
	10 K	300 K	
A ₁	124		Z(Ho)
	269	262	+Z(Ho), -Z(Mn)
	306	295	X(Mn), Z(O ₃)
		411	+Z(O ₃), -Z(O ₄), +X, Y(O ₂), -X, Y(O ₁)
	430	427	+Z(O ₄ , O ₃), -Z(Mn)
	466	463	+X, Y(O ₁ , O ₂), -X, Y(Mn)
	687	685	+Z(O ₁), -Z(O ₂)
E ₂	143	136	X, Y(Ho)
	164		X, Y(Ho)
	232	221	+X, Y(Mn), -X, Y(O ₃ , O ₄)
	300	295	Z(O ₁ , O ₂), X, Y(O ₄)
		442	+X, Y(O ₄), -X, Y(O ₁ , Mn)
	638		X, Y(O ₃ , O ₄)

Figure 3.18a shows the temperature dependence of Raman spectra and Fig. 3.18 b represents the normalized frequencies over the frequency at 10K of several A₁ and

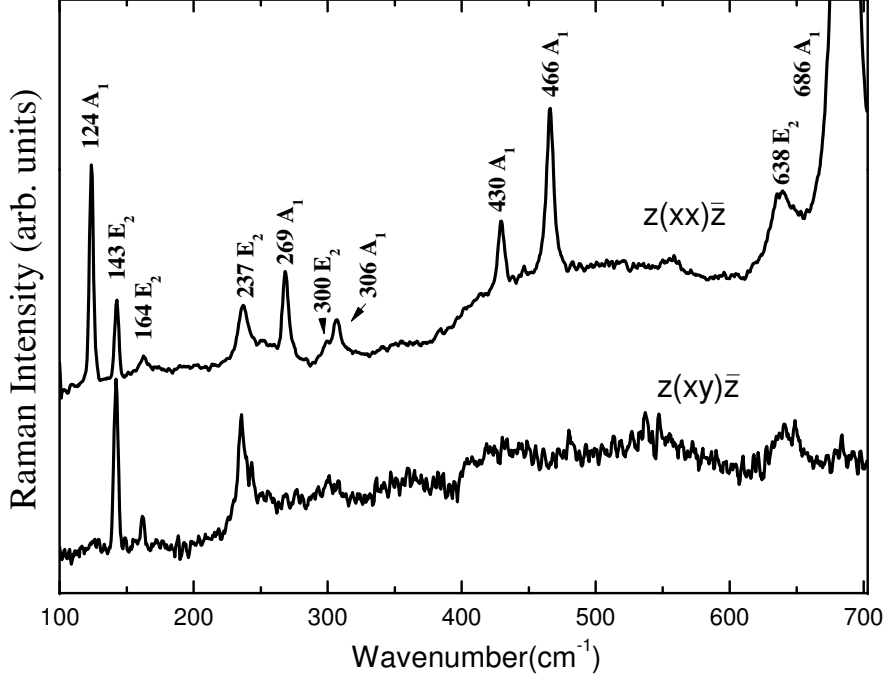


FIGURE 3.17: Raman spectra of h-HoMnO_3 single crystal measured at 10K using $z(xy)\bar{z}$ and $z(xx)\bar{z}$ configurations.

E_2 modes. The phonon frequencies soften due to the dilation of the unit cell when temperature increases. The E_2 modes at 237cm^{-1} presents a frequency shift beyond the mean behavior of the other modes as shown in Fig. 3.18 b. Moreover, two other A_1 modes at 267 and 686cm^{-1} present abnormal behavior around the Néel temperature. The frequencies of the three modes as a function of the temperature are shown in Fig. 3.19.

The frequency shift of E_2 mode at 237cm^{-1} presents a change of slope around the Néel temperature as shown in Fig. 3.19a. Similar anomalies have been reported in YbMnO_3 and YMnO_3 single crystal in this chapter. This mode corresponds to the relative displacement of Mn and O ions in the a-b plane, which modulates the Mn-O-Mn angles in the a-b plane and in-plane superexchange.

The frequencies of the A_1 modes at 267 and 686cm^{-1} presents an abrupt change at the magnetic transition. The A_1 modes at 686cm^{-1} corresponds to the displacement of apical O1 and O2 atom along the c-axis direction. Therefore this mode modulates the Mn-O-O-Mn bond angles, and, hence, the Mn-Mn interaction between the adjacent Mn planes. This interaction corresponds to the super-superexchange paths by the way of the apical oxygen and leads to the three dimensional magnetic ordering below Néel temperature. The A_1 modes at 267cm^{-1} represents the relative displacement of Mn and

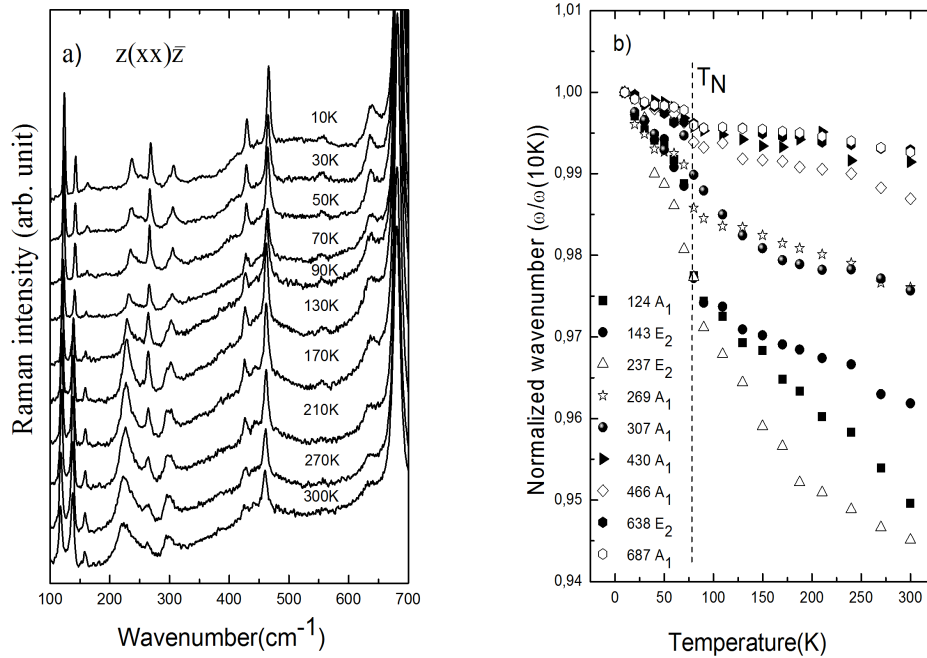


FIGURE 3.18: (a) Raman spectra of h-HoMnO₃ from 10 to 300 K in $z(xx)\bar{z}$ configuration, (b) Normalized wave numbers $[\omega(T)/\omega(7\text{ K})]$ of phonon modes as a function of temperature.

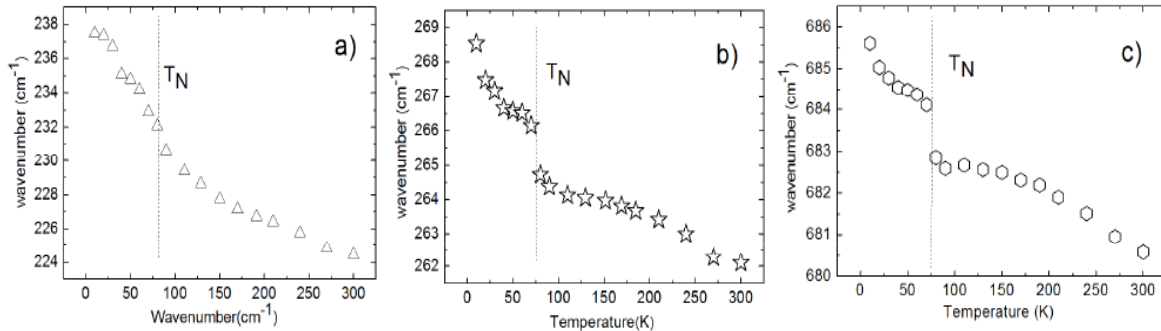


FIGURE 3.19: The frequency of (a) E₂ mode at 237 cm^{-1} , (b) A₁ mode at 267 cm^{-1} and (c) A₁ mode at 686 cm^{-1} as a function of temperature.

Ho along the c -axis direction. Therefore this mode modulates the Mn-O-Ho interaction which is conducted by the apical oxygen. Remember that the dominant magnetic interaction in hexagonal RMnO₃ is the Mn-O-Mn superexchange interaction within the plane whereas the Mn-O-O-Mn and R-O-Mn is weaker by 2 orders. Nevertheless, the abnormal behavior of these two modes around the Néel temperature demonstrates that the interplane Mn-Mn interaction and Ho-Mn interaction along c -axis also play an important role in the magnetic ordering of HoMnO₃.

3.5.2 Magnetic excitations

Figure 3.20a shows the magnon dispersion along the $\mathbf{k}=(1,0,k)$ and $\mathbf{k}=(k,0,0)$ axes. (Vajk et al., 2005) Three spin waves branches are observed in the direction $(k,0,0)$. Two branches are degenerated at 45 cm^{-1} at the zone center and correspond to the in-plane fluctuations. At the zone edge, the energy of these two branches are 88 and 128 cm^{-1} respectively. They are associated to the spin excitations of the Mn^{3+} magnetic structure in the a-b plane. At the Γ point, they correspond to the global rotations of the 120° pattern inside the a-b plane. The third dispersion branch has a zone-center energy around 10 cm^{-1} and corresponds to the out-of-plane spin fluctuation. This mode is related to the uniaxial anisotropy gap. Figure 3.20 shows the low frequency Raman spectra of h- HoMnO_3 single crystal at 10K . Two peaks are detected : $P_2 = 25 \text{ cm}^{-1}$ and $P_3 = 41 \text{ cm}^{-1}$. Combining the neutron and Raman measurements in Fig. 3.20 a and b, the P_3 peak can be clearly classified to one-magnon excitations at the center of Brillouin zone at 45 cm^{-1} and associated to the in-plane spin fluctuations. The P_2 peak cannot be identified to an excitation at the zone-center. Moreover the low energy excitation at 10 cm^{-1} in the neutron measurement in Γ point as shown in Fig. 3.20a cannot be observed in the Raman spectra. This is because this excitation is very close to the Rayleigh light (the inelastic scattering).

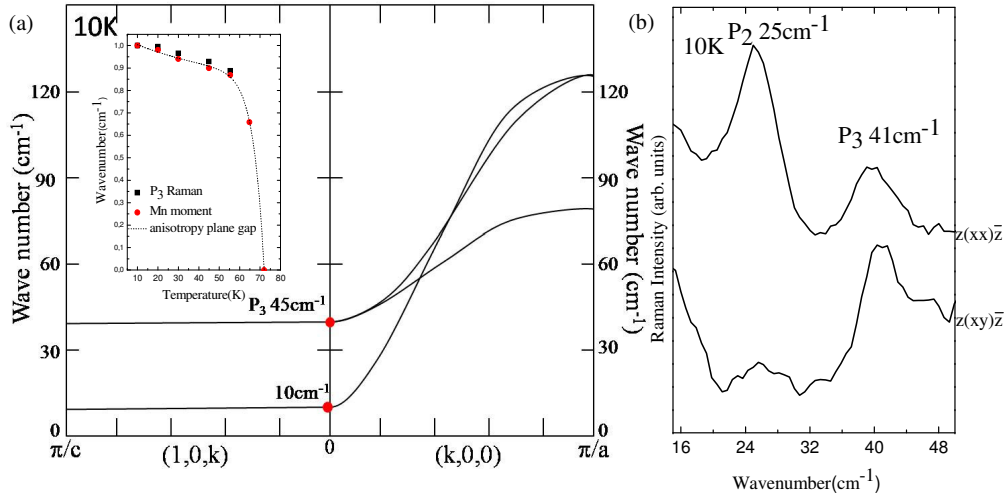


FIGURE 3.20: a) the magnon dispersion along the $\mathbf{k}=(1,0,k)$ and $\mathbf{k}=(k,0,0)$ axes. (Vajk et al., 2005; Fabreges, 2010) b) Raman spectra of low frequency excitation at 7K in $z(xy)\bar{z}$ and $z(xx)\bar{z}$ configurations.

We also measured the temperature dependence of low energy Raman spectra and frequencies as shown in Fig. 3.21a and b. respectively. The temperature dependence of the normalized P_3 frequency recorded from 10 to 55K in the $z(xy)\bar{z}$ configuration is shown in Fig. 3.21a inset. The planar spin gap energy and Mn moment measured by neutron scattering are also shown in this figure. It clearly shows that the temperature evolution of P_3 spin excitation agrees with that of planar gap energy and magnetic

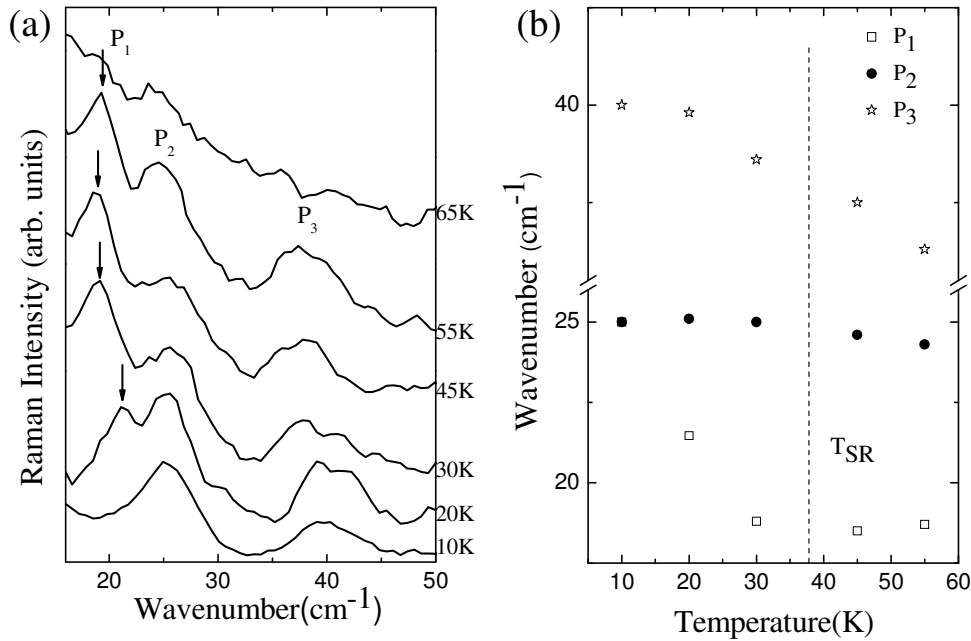


FIGURE 3.21: a) Temperature-dependent Raman spectra in the low frequency region between 10 and 55 K. b) Temperature dependence of wave number of magnetic modes.

moment of Mn ions. It proves that P₃ excitation corresponds to the Mn³⁺ spins in the a-b plane.

We can also observe that the P₂ peak divides into two peaks P₁ and P₂ with increasing temperature. To identify these two peaks, we can refer to the neutron diffraction measurements on HoMnO₃ single crystal by Fabreges. (Fabreges, 2010) Figure 3.22 shows the scattering intensity of HoMnO₃ along the (100) direction as function as the energy at a) 45K and b) 27K. Two excitations at 19.5 and 25 cm⁻¹ are observed at 45K. Two peaks at 20.8 and 25 cm⁻¹ are present in the spectra of 27K. We compare these two excitations to the P₁ and P₂ excitations in our temperature measurement. It clearly shows that P₁ and P₂ excitations correspond to the peak at 20 cm⁻¹ and 25 cm⁻¹ respectively. These two peaks are attributed to the crystal field of Ho ions. (Fabreges, 2010)

The Ho(4b) moment and uniaxial gap energy are compared to the Fabreges work. (Fabreges, 2010) Fig. 3.23 a presents the anisotropic uniaxial gap (black) and R(4b) moment (red) as a function of temperature in HoMnO₃ single crystal. It clearly shows that the anisotropic uniaxial gap does not agree with Ho(4b) moment below T_{SR}. The calculated uniaxial gap is based on the exchange interaction between Ho and Mn ions along c-axis. Therefore it proves the Ho ions on the 4b sites is not oriented by the Ho-Mn interaction. In the low frequency Raman measurement of HoMnO₃, we observe two crystal field excitations P₁ and P₂. Figure 3.23b shows the comparison of normalized Ho moment and P₁ excitation energy which are normalized by the equation $(E_T - E_{55K}) / (E_{10K} - E_{55K})$. E_T, E_{10K} and E_{55K} are the energy of these excitations

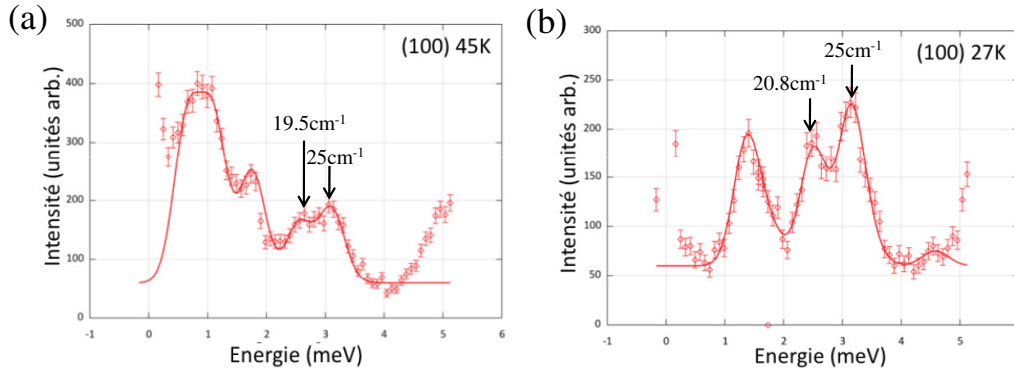


FIGURE 3.22: The scattered intensity of HoMnO_3 consists in the (100) of the reciprocal space as a function of energy for temperatures a) 45K and b) 27K measured by neutron scattering.(Fabreges, 2010)

in T, 10K, and 55K respectively. It can be observed that the temperature behavior of P_1 peak agrees with that of Ho(4b) moment which proves that the crystal field play an important role in the Ho (4b) ion ordering. In conclusion, the mechanism of Ho (4b) ion spin ordering is different from that of Yb (4b), only Ho-Mn interaction is not enough to interpret the Ho (4b) moment. The combination of Ho-Mn interaction and crystal field affect the Ho (4b) spin ordering and the crystal field play primary role in the ordering of Ho (4b) spin below T_{SR} .

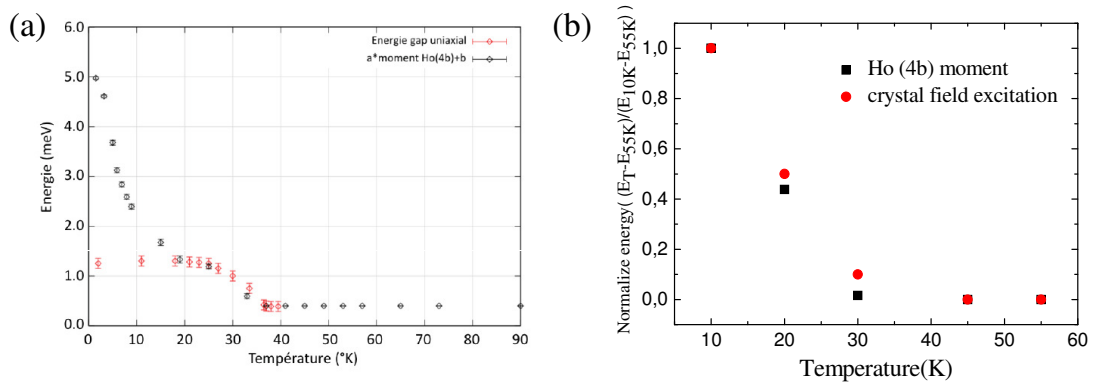


FIGURE 3.23: (a) Anisotropic uniaxial gap (black) and Ho(4b) moment (red) as a function of temperature of HoMnO_3 (Fabreges, 2010) and (b) the normalized Ho moment (black) and P_1 crystal field excitation energy (red).

3.5.3 Conclusion

We have identified 6 A_1 modes and 5 E_2 modes in the Raman spectra of HoMnO_3 single crystal. Two A_1 modes(267 and 686cm^{-1}) and one E_2 modes at 237cm^{-1}

present abrupt change around T_N which shows the role of interaction in HoMnO₃ single crystal. In low-energy Raman scattering, we observe three peaks. The peak at 41 cm⁻¹ corresponds to in-plane anisotropy. The other two peaks at 21 and 25 cm⁻¹ in 20K is attributed to crystal field excitation. The good agreement between the temperature behavior of the crystal field excitation and Ho (4b) moment below T_{SR} indicates the Ho(4b) magnetic order is connected to the crystal field excitation instead of molecular field below T_{SR} .

3.6 Conclusion

In summary, we measure Raman spectra of hexagonal RMnO₃ (R=Yb, Y and Ho) single crystals as a function of temperature and external magnetic field. The abrupt change of the lattice excitations around Néel temperature indicates the coupling of lattice and spin excitations. Moreover, the involved lattice excitations clearly shows the R-Mn and R-R interplane interaction along c-axis also play an important role in the establishment of the magnetic structure of h-RMnO₃.

The spin excitations are also observed in these compounds. We identify these spin excitations to one-magnon excitation, two-magnon excitation and crystal field excitation respectively. The results indicate that the interplane interaction also play an important role in the magnetic ordering of hexagonal RMnO₃. Moreover, phase transitions below the Néel temperature are observed in YbMnO₃ and HoMnO₃. Our work shows that the magnetic order of hexagonal RMnO₃ is strongly influenced by the R ions.

Chapitre 4

Magnetic excitations in BiFeO₃ thin films

BiFeO₃ thin films are multiferroics with both antiferromagnetic and ferroelectric orders and have shown application potential in fields as diverse as nanoelectronics (Seidel et al., 2009), photovoltaics (Yang et al., 2009; Allibe et al., 2010) and energy harvesting (Zeches et al., 2009). Nevertheless, the research on the magnetic excitations of BiFeO₃ thin films is rare and the results are contradictory. (Bai et al., 2005; Bea et al., 2007; Ke et al., 2010) Therefore, in this chapter, we investigate the dynamic and static spin properties of BiFeO₃ thin films on different substrates. We have collaborated with several groups : A. Barthelemy and M. Bibes group of Unite Mixte de Physique CNRS/Thales and Universite Paris-Sud which synthesized these BiFeO₃ thin films, L. Bellaiche groups of University of Arkansas for the theoretical calculations and J. Juraszek group of Universite de Rouen which conducts the Mössbauer measurements.

4.1 Raman spectroscopy of BiFeO₃ thin films

4.1.1 Magnetic excitations in BiFeO₃ single crystal

As we mentioned in chapter 1, below the Néel temperature, the incommensurate cycloid spin of Fe³⁺ appears in the BiFeO₃ single crystals. The corresponding spin wave modes (magnon) were firstly observed by Cazayous (Cazayous et al., 2008) and Singh (Singh et al., 2008).

Cazayous et al. observed two different types of peaks at low energies using two different polarizations. (Cazayous et al., 2008) The ϕ modes correspond to the oscillation of the spins in the cycloid plane (xz) called cyclon modes and the ψ modes correspond to the oscillation of the spins out of the plane and called extra-cyclon modes.

At the center of the Brillouin zone, the energies of cyclon (E_c) and extra-cyclon (E_{exc}) modes can be written in two simplified relations :

$$E_c(n) = \epsilon_c(q)n \quad (4.1)$$

$$E_{exc}(n) = \epsilon_c(q)(n^2 + 1)^{\frac{1}{2}} \quad (4.2)$$

where $\epsilon_c(q)$ is the calculated energy at wavevector q .

4.1.2 Strain effect on thin film

Strain engineering has recently emerged as a powerful means for tuning the various remarkable functionalities of perovskite oxide thin films. For instance, epitaxial strain can strongly enhance ferroelectric properties in BaTiO₃ (Choi et al., 2004), induces ferroelectricity in SrTiO₃ (Haeni et al., 2004) and EuTiO₃ (Lee et al., 2010) or suppresses ferromagnetism in mixed-valence magnites. However, to date, few strain engineering has been applied to modify the properties of antiferromagnets although they are ubiquitous in the perovskite family and show potential in many fields.

In BiFeO₃ single crystal, an additional long range cycloidal spin is superimposed upon the G-type antiferromagnetic order. It was proposed and experimentally confirmed through neutron diffraction that this cycloidal modulation is suppressed by high epitaxial strain in BiFeO₃ thin film. (Bai et al., 2005; Bea et al., 2007) Further measurements on thick, partially relaxed films however showed cycloidal characters. (Ke et al., 2010) To gain deeper insight into the influence of strains on the spin structure of BiFeO₃ thin film, a series of films on substrates spanning strains from -2.6% (compress) to +1.3% (tensile) : (LaAlO₃)_{0.3}-(Sr₂AlTaO₆)_{0.7} (LSAT) -2.6%, SrTiO₃(STO) -1.6%, DyScO₃(DSO) -0.7%, GdScO₃(GSO) -0.2%, SmScO₃(SSO) +0.4%, NdScO₃(NSO) +0.9% and PrScO₃(PSO)+1.3% are synthesized. Their thickness was set to 70 nm to prevent strain relaxation (except for LSAT for which it was 50 nm), as checked by reciprocal space maps. (Infante et al., 2010) Actually, these samples were already studied by Infante et al and the results show that Curie temperature is strongly affected by strains but the Néel temperature is almost constant in different strains samples as shown in Fig. 4.1. However, we will show that the magnetic structure is also strongly modified by strains.

4.1.3 Spin excitations in BiFeO₃ thin film

Figures 4.2a, b and c show the low energy Raman spectra measured on BiFeO₃ thin films on DSO, GSO and SSO substrates respectively. Just as BiFeO₃ single crystals, two different types of peaks in cross and parallel polarizations are identified in the films on DSO, GSO, SSO. The range of these peaks is between 8 and 45 cm⁻¹. As mentioned before, no phonon modes are expected below 70 cm⁻¹ and these two different types of modes are the fingerprint of cycloid structure in BiFeO₃. The peaks in parallel polarization are associated to ϕ mode and correspond to the cyclon modes. The peaks in cross polarization correspond to ψ mode and are associated to extra-cyclon magnetic excitations. In order to confirm the relationship between the peaks and spin modes, we

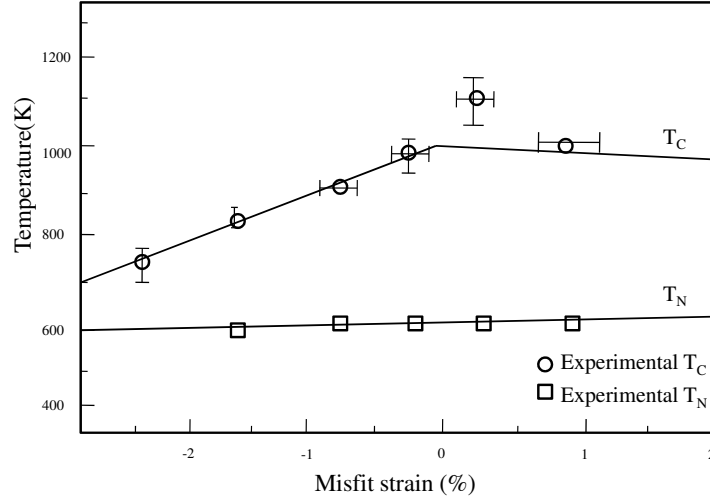


FIGURE 4.1: The Curie and Néel temperature curve as a function of misfit strain, the circles and squares correspond to the experimental Curie and Néel temperatures.

have drawn the peaks energies as function of peak index as shown in Fig. 4.2d, e and f. Our experimental data agree with the equation (4.1) and (4.2) well.

The experimental results have been fitted using the equation (4.1) and (4.2). The $\epsilon_c(q)$ values of DSO, GSO and SSO BiFeO₃ thin films are 6.2, 6.3 and 6.4 cm⁻¹ respectively. These values are smaller than the value (7.5 cm⁻¹) measured in BiFeO₃ single crystal which is 7.5 cm⁻¹. The estimated cyclon energy $\epsilon_c(q)$ calculated by de Sousa et al. is about 10¹² rad/s equivalent to 5.3 cm⁻¹ which is calculated in order to match the susceptibility of BiFeO₃ thin film.

Therefore, smaller $\epsilon_c(q)$ values in BiFeO₃ thin films on DSO, GSO and SSO substrates are expected comparing to the BiFeO₃ single crystal. For BiFeO₃ thin films under the strain from -0.7 % to +0.4 %, the agreement of our experimental data with the theoretical calculation proves the existence of cycloid spin. We also observe an abnormal peak (P_S peak) at 7.5 cm⁻¹ in DSO sample as shown in Fig. 4.2a. We will discuss this peak later.

Figures 4.3a, b, c and d show the low energy Raman spectra of BiFeO₃ thin films on LSAT, STO, NSO and PSO substrates respectively. The two different series of peaks disappear in these thin films, instead, there is only one peak in each polarization. The observation of two series of peaks by Raman scattering at the center of the Brillouin zone is due to the folding of the antiferromagnetic magnons induced by the incommensurability of the cycloid structure. Therefore, the disappearance of multi-peaks clearly shows that cycloidal spin is destroyed in these highly strained thin films with compressive misfit is bigger than -1.6% and tensile misfit is bigger than +0.9%. It indicates that strain engineering is an effective way to modify the magnetic structure in BiFeO₃ thin films. Bai's work also indicated that the cycloidal spin structure can be destroyed by a critical perturbation provide by the elastic constraint of the film and a homogenous antiferromagnetic (AFM) spin state is stabilized. (Bai et al., 2005)

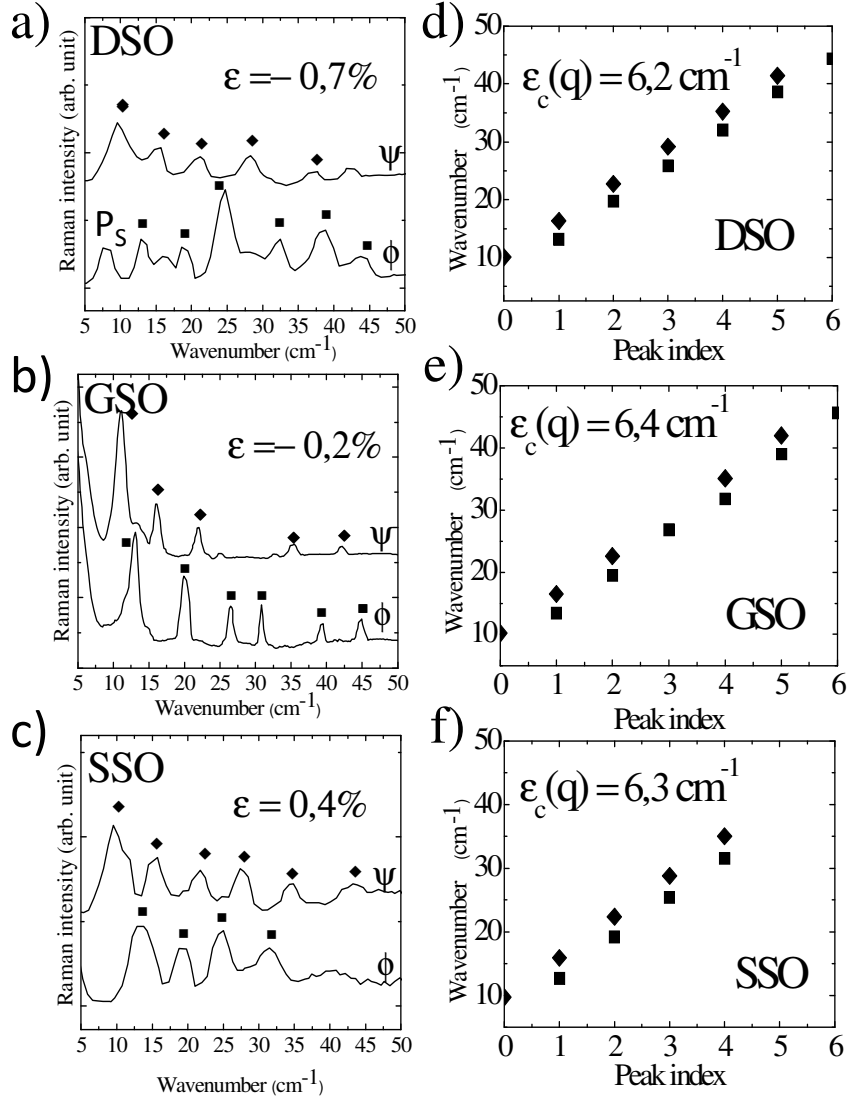


FIGURE 4.2: (a),(b) and (c) show the low energy Raman spectra of BiFeO₃ thin film on DSO, GSO and SSO substrates respectively. (d), (e) and (f) present the frequencies of the ϕ and ψ modes as a function of the mode index n .

To understand the origin of these two peaks, we can recall several theoretical and experimental works. C. Ederer et al. predicts a weak ferromagnetism in BiFeO₃ single crystal. (Ederer & Spaldin, 2005) Then Ramazanoglu et al. observed that the spins have a small canting out of the cycloid plane in BiFeO₃ single crystal by polarized small angle neutron scattering (Ramazanoglu et al., 2011) responsible for a weak ferromagnetism. In thin film where the cycloid is suppressed, we still expect the presence of a small canting for the spins and a weak ferromagnetism. Sousa et al. developed a phenomenological Ginzburg-Landau theory based on canted AFM structure to calculate the spin wave excitation in BiFeO₃ thin film. The canted AFM order is constrained in

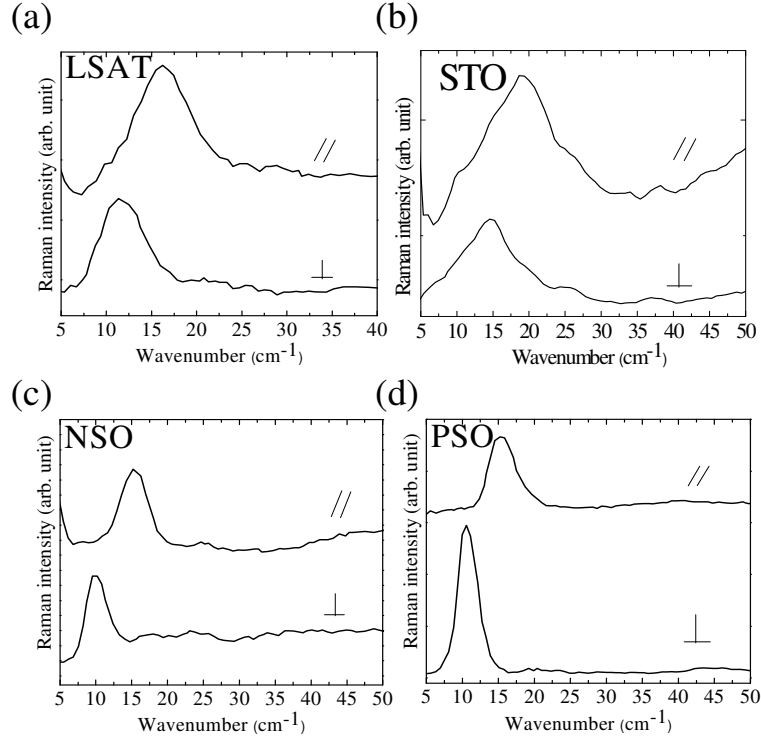


FIGURE 4.3: (a), (b), (c) and (d) are the Raman spectra of BiFeO₃ thin film on LSAT, STO, NSO and PSO substrates respectively.

the plane perpendicular to the ferroelectric polarization and two corresponding spin wave modes are shown in Fig. 4.4 a and b. In their work, two spin wave modes (low frequency and high frequency modes) are predicted in BiFeO₃ thin film. The low frequency spin wave mode around 4 cm⁻¹ corresponds to the magnetostatic correction in the presence of weak ferromagnetism. The high frequency mode around 25 cm⁻¹ is due to the Dzyaloshinskii-Moriya (DM) coupling. (de Sousa & Moore, 2008a) Recently, Wang et al. developed a new first-principles-based approach to simulate dynamical properties which includes both structural degrees of freedom and magnetic moments as dynamic variables in Newtonian and Landau-Lifshitz-Gilbert (LLG) equations within molecular dynamics. (Wang et al., 2012) The calculated complex electric and magnetic susceptibilities as function of frequency is shown in Fig. 4.5 a and b respectively.

In Fig. 4.5 b, two peaks which means two resonant frequencies around 7 (blue arrow) and 85 cm⁻¹ can be observed. The low energy magnon disappears when the parameter responsible for the spin-canted structure of BiFeO₃ is switched off. In other words, the pure AFM G-type structure does not possess such magnon and this magnon only exists in the spin-canted state. The supplement information in the work (Wang et al., 2012) demonstrates that this magnon is associated with the rotation of magnetic dipoles inside the (111) plane. This rotation of magnetic dipoles agree with the low-frequency spin wave mode in Sousa et al. work which means this low frequency magnon

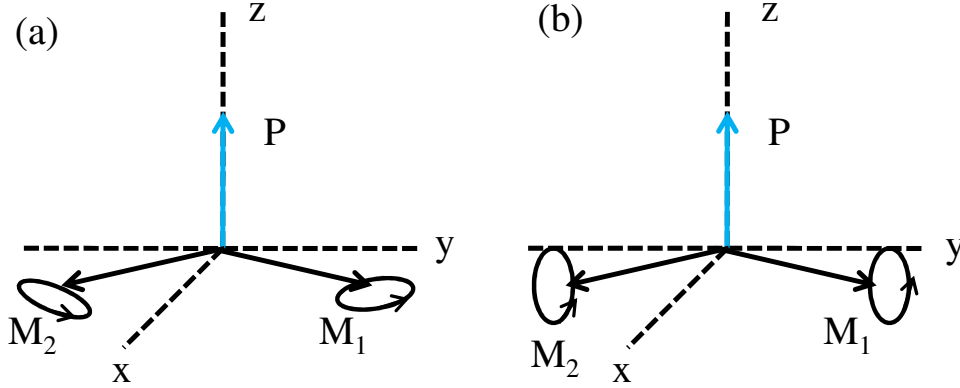


FIGURE 4.4: The spin wave in BiFeO₃ thin films. The sublattice magnetization M_1 and M_2 lie in the plane perpendicular to ferroelectric polarization. a) the low frequency spin wave mode. b) The high frequency spin wave mode.

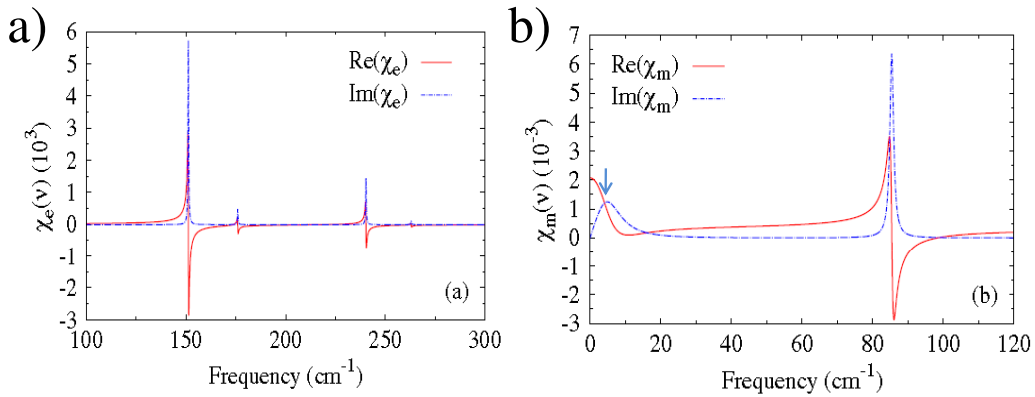


FIGURE 4.5: The (a) complex electric and (b) magnetic susceptibilities as function of frequency in BiFeO₃ at $T=20$ K. (Wang et al., 2012)

corresponds to the oscillation of the weak ferromagnetic moment around its equilibrium position in the basal plane as shown in Fig. 4.4a. The high energy mode is associated with fast oscillations of the magnetic dipoles going in and out of the (111) plane, as well as, a change in length of the weak ferromagnetic vector due to the DM coupling. The high energy magnon therefore corresponds to the high-frequency gapped spin wave mode in Sousa et al. work as shown in Fig. 4.4b.

Our Raman light scattering measurements of BiFeO₃ thin films on LSAT, STO, NSO and PSO substrates shows two peaks, the low energy peak is around 10 cm^{-1} which is very close to the theoretical low-frequency mode at 7 cm^{-1} and high energy peak is about $15\text{-}20 \text{ cm}^{-1}$. According to the previous theoretical calculation, we can attribute the low energy peak to the low-frequency spin wave mode. The small energy difference might be due to single ion anisotropy. The theoretical calculation shows that

the high-frequency spin wave mode is at around 80 cm^{-1} . This mode is due to the DM coupling so that the calculation is based on the DM coupling factor \mathbf{D} . Nevertheless, the value of \mathbf{D} is not determined yet. For example Matsuda et al. observed two excitation gap at 9 and 20 cm^{-1} by inelastic neutron scattering in BiFeO₃ single crystal and estimate \mathbf{D} to be 0.1623 meV . (Matsuda et al., 2012) Moreover, Jeong et al. measured one magnetic excitation at 72.5 meV in BiFeO₃ single crystal and estimate \mathbf{D} to be 0.107 meV . (Jeong et al., 2012) Therefore, the high energy peak still could be attributed to the high-frequency spin wave mode which corresponds to the oscillations of magnetic dipoles going in and out of the (111) plane. These two peaks are strong evidence for the spin-canted state in highly strained BiFeO₃ thin films, which also indicate the weak ferromagnetism induced by spin-canted state is not inert to the cycloidal spin structure.

Now let us back to the special excitation P_S at 7 cm^{-1} in BiFeO₃ thin film on DSO substrate as shown in Fig.4.2a. This peak could be the low-frequency spin wave excitation due to the presence of spin-canted phase. A spin-canted state may coexisted with the cycloidal phase in BiFeO₃ thin film. In the following part of this chapter, Mössbauer measurement will further prove the presence of spin-canted phase in BiFeO₃ thin film on DSO substrate.

4.2 Mössbauer measurements of BiFeO₃ thin film

4.2.1 Mössbauer spectroscopy

To deeply understand the magnetic order of BiFeO₃ thin films, we coworked with J. Juraszek group to use conversion electron Mössbauer spectroscopy (CEMS). This technique probes the hyperfine interactions between the ⁵⁷Fe nuclei and their electronic environment through the absorption of γ photons emitted by a radioactive source of ⁵⁷Co. During the experiments, the source is displaced towards or away from the sample, which respectively blue- or red-shifts the radiation, thereby allowing absorption in a narrow energy range around the intrinsic γ photons energy. The obtained spectra provide information on the electronic density at the nuclei (through the so-called isomer shift), a possible electric field gradient (quadrupole splitting) and the magnetic environment (magnetic splitting). The measurement geometry of conversion electron Mössbauer spectroscopy used to study BiFeO₃ thin films is shown in Fig. 4.6.

The cycloidal modulation in BiFeO₃ results in a gradual rotation of the magnetic moments of the Fe³⁺ ions in the plane defined by the direction of propagation of the cycloid and the direction of the electric polarization, which is along [111] in the bulk. We assume that this electric polarization direction, which is a high symmetry axis of the crystal, is the main axis OZ of the electric field gradient (EFG) tensor. Such rotation of the magnetic moments in a plane containing the main axis of the EFG tensor leads to an asymmetric line broadening on the reported Mössbauer spectra of polycrystalline BiFeO₃. In the case of single crystal samples, the line intensity ratio R_{23} between lines 2 (5) and 3 (4) of the magnetic sextet as shown in Fig. 4.6 will also depend on the orientation of the cycloid plane with respect to the direction of the

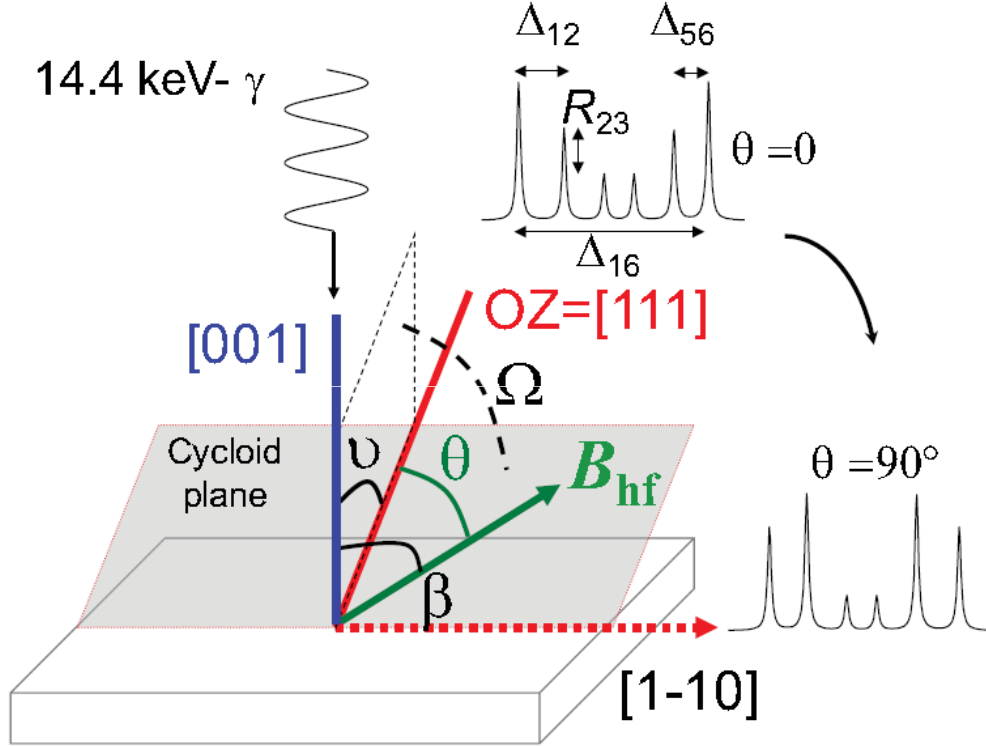


FIGURE 4.6: Sketch of measurement geometry for CEMS experiments and the bulk-like cycloidal plane. The six lines of the CEMS spectra are due to magnetic splitting which is a result of the interaction between the nucleus and surrounding magnetic field.

incident γ -ray beam.

Line broadening is related to small displacements of the hyperfine energy levels at the ^{57}Co nuclear site in the presence of combined quadrupole electric and magnetic dipole interactions. Indeed, any rotation of the magnetic moments by an angle β relative to the OZ axis would result in a shift of hyperfine energy levels, resulting to an angular variation of the quadrupole shift $2\varepsilon(\theta) = -\Delta E_Q/2 (3\cos^2\theta - 1)$, where $-\Delta E_Q = 0.44$ mm/s is the value of the quadrupole splitting reported for bulk BiFeO₃. This variation of the quadrupole shift $2\varepsilon(\theta)$ related to the rotation of the magnetic moments in the plane of the cycloid manifests itself by only a symmetric broadening of the absorption lines of the magnetic sextet.

To account for the asymmetry of the broadened lines observed in the Mössbauer spectra of bulk BiFeO₃, an additional anisotropy of the hyperfine interaction at the ^{57}Fe nucleus site along the cycloid resulting in a very small angular variation of the magnitude of the hyperfine field along the cycloid propagation direction has been proposed. A relation as $B_{hf}(\theta) = B_{hf//}\cos^2\theta + B_{hf\perp}\sin^2\theta$, where $B_{hf//}$ and $B_{hf\perp}$ are two constant parameters with a $h = B_{hf//} / B_{hf\perp}$ ratio value close to 0.98, allows to reproduce such asymmetric line of the BiFeO₃ spectrum of bulk BiFeO₃, as well as the line shape of ^{57}Fe Nuclear Magnetic Resonance (NMR) measurement. (Zalesky et al.,

2000)

A modulation of the magnetic moment orientation inside the cycloid plane implies also a variation of the orientation angle β between the hyperfine field and the γ - ray direction (which is along [001]). Such angular variation of β leads to a variation of the R_{23} line intensity ratio of the magnetic sextet by $R_{23}=4(1-\cos^2\beta)/(1+\cos^2\beta)$. Therefore, for a cycloid propagating along [1-10], β is ranging between 54.74° ($R_{23}=2$) and 90° ($R_{23}=4$) as θ varies from 0 to 90° , respectively. For the two other propagation directions ([10-1] and [0-11]) observed in the bulk, β is ranging between 35.26° ($R_{23}=0.8$) and 90° ($R_{23}=2$) for θ varying between 0 and 141° , respectively. Finally for a direction of propagation of the cycloid along [110], the cycloid plane is perpendicular to the film plane ($\beta=54.74^\circ$) and θ varies between 0 ($R_{23}=0$) and 90° ($R_{23}=4$).

4.2.2 Mössbauer spectra of BiFeO₃ thin films

The experimental CEMS spectra collected at 295 K on the seven BiFeO₃ films grown on various substrates are presented in Fig. 4.7 b to h. All spectra exhibit a six-line magnetic hyperfine pattern with an isomer shift value of $0.37 \text{ mm}\cdot\text{s}^{-1}$, which is characteristic of Fe³⁺ ions in octahedral coordination. The six lines are due to magnetic splitting induced by the interaction between the nucleus and surrounding magnetic field. While almost perfectly symmetric lines are found for BiFeO₃ films on LSAT, STO, NSO and PSO substrates (high compressive and tensile strain), a clear asymmetry (in both the amplitude and breadth of the peaks) is observed for those grown on DSO, GSO and SSO that are weakly strained. As mentioned before, the asymmetry pattern is due to the rotation of magnetic moment in a plane. Therefore, in BiFeO₃, such an asymmetric line broadening is the fingerprint of a cycloidal modulation of the Fe³⁺ spins (Lebeugle et al., 2007). The CEMS results therefore show that at low strain, the cycloid is present, while high strain destroys it. The measurements are consistent with the scenario based on our Raman measurement.

The red lines on Fig. 4.7 d and e are fits of the CEMS spectra with a model based on the bulk cycloid, i.e. with spins rotating in a plane defined by the pseudocubic [1-10] direction of propagation and the direction of the electric polarization, which is along [111] in the bulk (and close to [111] in weakly strained films (Daumont et al., 2012)). Because the γ photons impinge upon the films at normal incidence (see Fig. 4.7 a), the various magnetic domains equivalent by 90 degree rotations about the film normal are probed equivalently. For GSO, the spectrum can be well fitted with this model. This confirms a bulk-like cycloidal ordering in this weakly strained sample. For DSO, the data are not perfectly reproduced using a bulk-like harmonic cycloidal model.

Figure 4.8 shows different fits of the CEMS data for the BiFeO₃/DSO sample. Figure 4.8 a is a fit using a cycloid model, with a harmonic cycloid. The fit reproduces the asymmetry of the data, but the agreement is rather poor in terms of the intensity of the 2nd and 5th lines. To better visualize the fit quality, the difference between the data and the fit is shown. The absolute value of this difference (Δ) is used to quantify the fit quality. In Fig. 4.8 a, the harmonic cycloid fit yields to $\Delta=62.10^{-3}$. The fit is slightly improved by using an inharmonic cycloid ($m=0.95$, $\Delta=63.10^{-3}$), but the intensity of

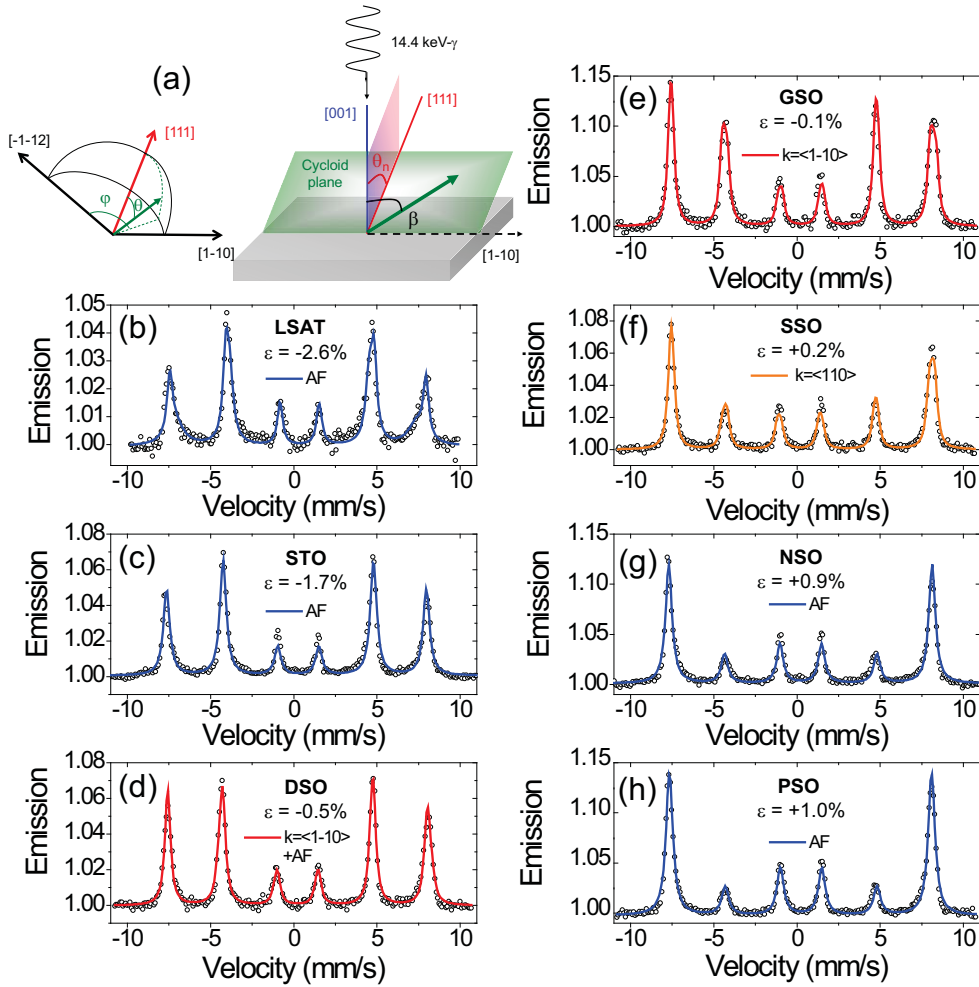


FIGURE 4.7: (a) Sketch of measurement geometry for CEMS experiments and the bulk-like cyclodial plane. The different angles used in this work are indicated. (b)-(h) present the CEMS spectra of BiFeO₃ thin film on seven different substrates. The data are shown as symbols and lines are the best fits to the data. Blue lines correspond to fits with an AFM arrangement and AFM vector lying at an angle β from the film normal.

lines 2 and 5 is still not perfectly reproduced (Fig. 4.8 b). Considering a mixed system, with 30% type-1 cycloid and 70% pseudo-collinear antiferromagnetic order with spins in the plane yields a much perfect fit with $\Delta = 40 \cdot 10^{-3}$ (Fig. 4.8 c). This measurement indicates that the magnetic order BiFeO₃ thin film on DSO substrate is a mixture with cycloid and homogenous state. This result agrees with the Raman result on the same sample where one special peak P_S is observed (Fig. 4.2 a).

For BiFeO₃ thin films on SSO the data cannot be reproduced by a conventional cyclodial model. (Fig. 4.9 a) This spectrum is however clearly asymmetric, meaning that a pseudo-collinear antiferromagnetic order cannot apply either. In Fig. 4.9 b the data are fitted with a type 1 model (bulk-like type), but with propagation direction

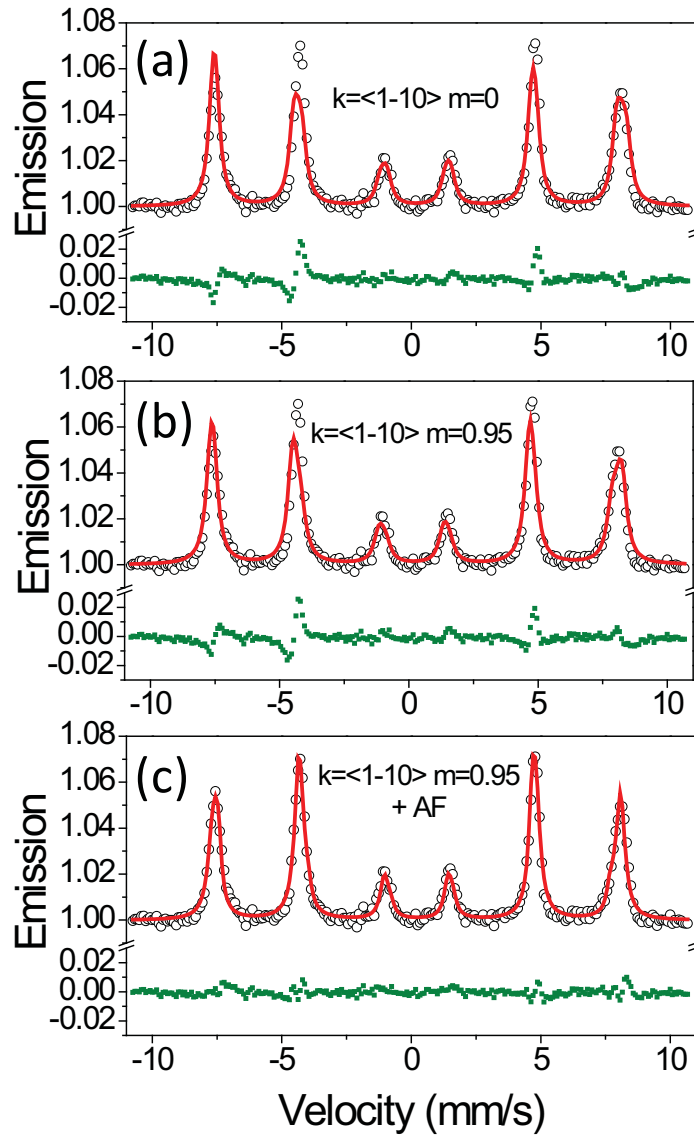


FIGURE 4.8: CEMS data and fits for a BiFeO_3 thin film on DSO substrate. The data in (a), (b) and (c) are fitted using type-1 cycloid model with a harmonic cycloid, type-1 cycloid model with an inharmonic cycloid, and 30% type-1 cycloid and 70% pseudo-collinear antiferromagnetic order respectively. The difference between the data and the fit is shown in green.

k along $[10-1]$. The fit is better. In Fig. 4.9 c, a type 2 cycloid (a period enlarged by a factor 1.22 with respect to bulk crystal) with k along $[110]$ is applied. This yields the best fit. Therefore the cycloidal structure in BiFeO_3 thin films on SSO substrate is changed. The strain can also influence the cycloid structure in BiFeO_3 thin films.

Now let us take a closer look at the homogeneous state that is stable at high strain.

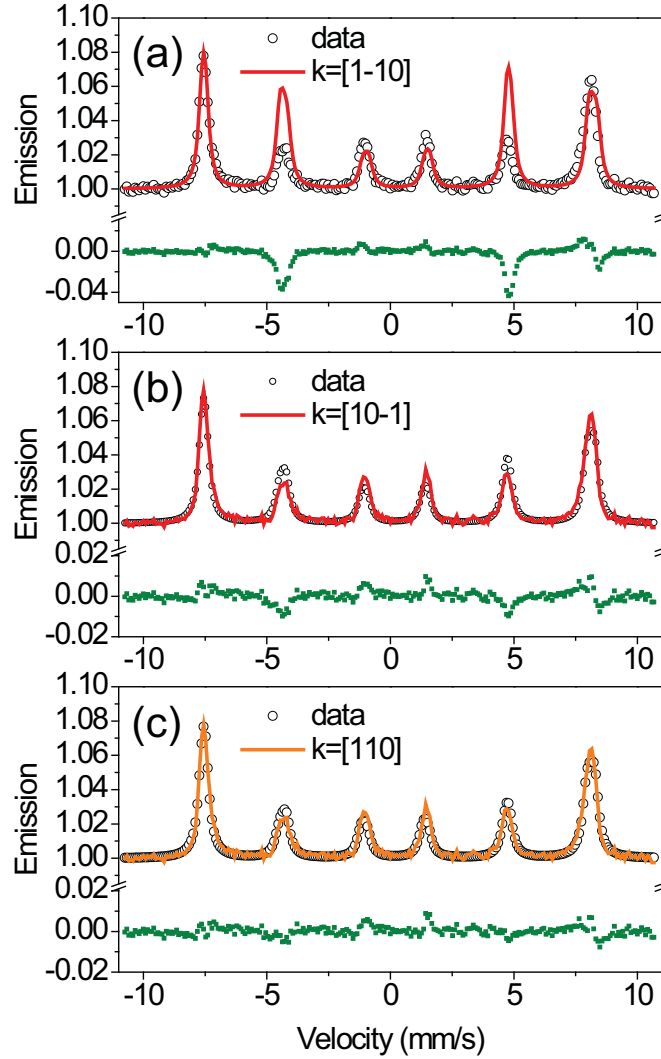


FIGURE 4.9: CEMS data and fits for a BiFeO_3 thin film on SSO substrate. The data in (a), (b) and (c) are fits using type-1 with $K=[1-10]$, type-1 with $K=[10-1]$ and type-2 with $K=[110]$ cycloid models respectively. The difference between the data and the fit is shown in green.

Beyond the strain-dependence of the spectral asymmetry, another visible feature is the variation of the relative intensity of the different peaks. In Mössbauer spectroscopy, the relative intensity of the lines in a magnetically split sextet is indicative of the average orientation of the magnetic moments. The ratio R_{23} between the second (or fifth) and third (or fourth) lines of the magnetic sextet is given by $R_{23} = 4 \sin^2 \beta / (1 + \cos^2 \beta)$. In normal incidence, $R_{23} = 4$ for in-plane spins, and $R_{23} = 0$ for perpendicular spins. At high compressive strain (LSAT, STO), R_{23} is close to 4 and thus the Fe spins are in-plane. For PSO, $R_{23} = 0.73$, which corresponds to spins being close to out-of-plane. Accordingly, the spectra for films on LSAT, STO, NSO and PSO can be well fitted by models with antiferromagnetic Fe^{3+} spins pointing at an angle β from the normal

direction (blue lines in Fig. 4.7 b, c, g and h).

4.2.3 Landau-Ginzburg theory

In order to support the Raman and Mössbauer measurements and to gain more insight into the influence of strain onto the magnetic order in BiFeO₃ films, we have used Landau-Ginzburg theory and the free energy can be expressed as :

$$F = F_{exch} + F_{ME} + F_{an} + F_{M_Elast} \quad (4.3)$$

where

$$F_{exch} = A \sum_{i=x,y,z} (\Delta L_i)^2 = A((\Delta\theta)^2 + \sin^2\theta(\Delta\varphi)^2) \quad (4.4)$$

is the inhomogeneous exchange, and (θ, φ) are the polar and azimuthal angles of the unit antiferromagnetic vector $\mathbf{L}=(\sin\theta \cos\varphi, \sin\theta \sin\varphi, \cos\theta)$ in the spherical coordinate system with the polar axis aligned with the principal axis the bulk crystal pseudocubic [111] direction, and azimuthal axis along [-1-12]

The second term is the inhomogeneous magnetoelectric interaction that is proportional to the spatial derivatives of the magnetic order parameter and responsible for the spin cycloid ordering :

$$\begin{aligned} F_{ME} &= -\gamma \mathbf{p}(\mathbf{L}(\Delta \cdot \mathbf{L}) - (\mathbf{L}\Delta)\mathbf{L}) \\ &= -\gamma(\Delta_x\theta\cos\varphi + \Delta_y\theta\sin\varphi - \cos\theta\sin\theta(\sin\varphi\Delta_x\varphi - \cos\varphi\Delta_y\varphi)) \end{aligned} \quad (4.5)$$

where \mathbf{p} is the unit vector of electric polarization and γ is the flexomagnetoelectric constant.

The third term is the magnetic anisotropy corresponding to the bulk crystal with the principal axis [111] :

$$F_{an} = -K_{eff}\cos^2\theta \quad (4.6)$$

where K_{eff} is the effective anisotropy constant that includes the uniaxial magnetic anisotropy and the contribution from the Dzyaloshinskii-Moriya interaction.

The final term is the magnetoelastic one that corresponds to the epitaxial strain in the BiFeO₃ thin film :

$$F_{M_Elast} = -U \cdot (\mathbf{L} \cdot \mathbf{n})^2 = -U \cdot (\sin\theta_n \sin\theta \cos\varphi + \cos\theta_n \cos\theta)^2 \quad (4.7)$$

where U is the magnetoelastic energy constant and θ_n is the angle between the

polar axis and the normal to the (001) film plane, in spherical coordinate system.

The minimization of the free-energy function by the Lagrange-Euler method gives is equations :

$$2A\Delta\theta + 2\gamma\sin^2\theta(\sin\varphi\Delta_x\varphi - \cos\varphi\Delta_y\varphi) - \sin(2\theta)(A(\Delta\varphi)^2 + K_{eff}) = -U\frac{\partial(\mathbf{L} \cdot \mathbf{n})^2}{\partial\theta} \quad (4.8)$$

$$2A(\sin^2\theta\Delta\varphi + \sin 2\theta(\Delta\theta\Delta\varphi)) - 2\gamma\sin^2\theta(\sin\varphi\Delta_x\theta - \cos\varphi\Delta_y\theta) = -U\frac{\partial(\mathbf{L} \cdot \mathbf{n})^2}{\partial\theta} \quad (4.9)$$

whose solution are spin cycloids with a wave vector \mathbf{q} lying in the film plane. Remarkably, two types of the cycloid fulfill this condition :

The first one ("type-1") is a cycloid with the wave vector \mathbf{q} along [1-10]. The cycloid plane is inclined to the normal \mathbf{n} at the angle θ_n . It is analogous to the one observed in the bulk crystals with a period $\lambda=62$ nm. In a harmonical approximation it is described by the dependences : $\theta=q_0y$, $\varphi=\pi/2$ (Sosnowska & Zvezdin, 1995).

The second solution ("type-2") corresponds to a cycloid running along the [110] pseudocubic direction (described by unit vector $\zeta_0=(-\cos\theta_n; 0; \sin\theta_n)$ in spherical coordinate system) with a plane perpendicular to the film plane. In a harmonical approximation the type-2 cycloid is described by the dependences $\theta=q\zeta$, $\varphi=0$. Minimization of the free energy with respect to the wave vector \mathbf{q} gives for the period of the second type cycloid :

$$\lambda = \frac{2\pi}{q} = \frac{\lambda_0}{\sin\theta_n} \quad (4.10)$$

Thus, the type-2 cycloid has a period enlarged with respect to the bulk crystal case (by a factor about 1.22). In BiFeO₃ bulk crystals this cycloid is energetically unfavorable. As we show, it may however be stabilized in BiFeO₃ films. In the previous section, the fit based on type-2 cycloid perfectly fit the Mössbauer spectra of BiFeO₃ films on SSO sample.

There are also solutions corresponding to a (pseudo) homogenous spin order. Compressive strain induces an easy-plane state : $\theta=\pi/2$, $\varphi=\pi/2$. At tensile strain the resulting homogeneous state is determined by competing anisotropic contributions F_{an} and effective anisotropy due to the strain F_{M_Elast} . The equilibrium state is at the angles $\varphi=0, \pi$, and $\theta=\theta_0$ that fulfill the following condition :

$$\sin(2\theta_0)K_{eff} = 2U\sin(\beta + 2\theta_0)\sin\beta \quad (4.11)$$

where $\beta=\theta_0-\theta$ is the angle between antiferromagnetic vector and the normal to the film plane, U is the magnetoelastic energy constant and K_{eff} the bulk crystal anisotropy that comprises the magnetic crystal anisotropy and contribution from the Dzyaloshinskii-Moriya interaction.

The comparison of the free energies of these different phases yields the phase dia-

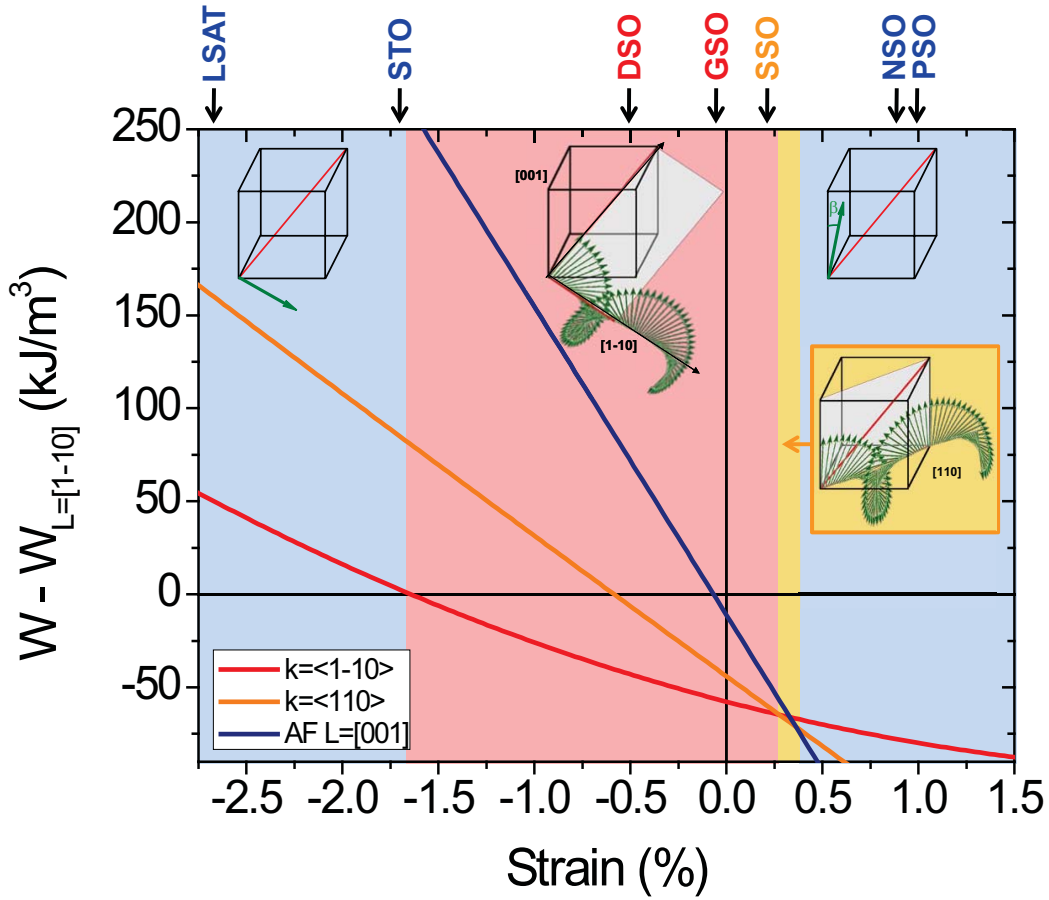


FIGURE 4.10: The energy of three magnetic states (bulk-like "type-1" cycloid with propagation vector along $\langle 1-10 \rangle$ directions, "type-2" cycloid with propagation vector along $\langle 110 \rangle$ directions and collinear antiferromagnetic order with antiferromagnetic vector close to $[001]$), relative to a fourth magnetic state, corresponding to a collinear antiferromagnetic order with antiferromagnetic vector along in-plane $[1-10]$ directions. The stability region of the different states is shown in colours (blue : antiferromagnetic ; red : type-1 cycloid ; orange : type-2 cycloid). The different substrates used are indicated on top of the diagram and located at their corresponding strain. Their colour corresponds to the magnetic state determined from the Mossbauer measurements. The sketches represent the different magnetic states, with spins shown in green.

gram shown in Fig. 4.10 (we use $H_{DM}=6.9$ T for the Dzyaloshinskii-Moriya field, which corresponds to a film magnetization $M_S=3.1$ kA/m, an exchange stiffness $A=0.04$ J/m estimated from the Neel temperature ; the flexomagnetolectric constant $\gamma=2Aq_0=0.6$ mJ/m² was found by minimization of the free energy ; $q_0=2\pi/\lambda_0$). (Sosnowska & Zvezdin, 1995) The homogeneous phases (shown in blue) are energetically favorable at high compressive and tensile strain (beyond about -1.6% and $+0.4\%$, respectively). The type-1 cycloid (shown in red) is predominant in the strain range from -1.6% to $+0.28\%$, while the type-2 cycloid (shown in orange) exists in narrow range (from $+0.28\%$ to

+0.37%). Note that the transitions between the different regions are of first order, so that phase coexistence (as found experimentally for the film on DSO) is possible.

To further understand these predictions, a recently developed effective Hamiltonian (H_{eff}) is supplemented to Landau-Ginzburg theory. (Rahmedov et al., 2012) This atomistic tool is able to reproduce the magnetic cycloid of bulk BiFeO₃ as well as its unusual features, by the incorporation of an original energetic term that can be thought of as representative of the converse spin-current model. (Katsura et al., 2005) The strength of this original energetic term is characterized by the coefficient denoted as C. In the present study and as done in previous work ((Daumont et al., 2012)), epitaxial (001)-oriented BiFeO₃ films is modeled by freezing some components of the strain tensor. Typically, 18×18×18 supercells are used to mimic such films, and the internal energy of this H_{eff} is used in Monte-Carlo simulations to predict their finite-temperature properties.

For small compressive strains, the H_{eff} approach indeed provides a magnetic cycloidal ground state that is similar to the one in the bulk. This cycloid has a propagation direction being along [1-10], when the polarization lies close to [111]. For a critical tensile strain and in accordance with the measurements and phenomenological works, the H_{eff} scheme predicts that this bulk-like cycloid becomes energetically unfavorable with respect to a second type of cycloid for which the propagation direction now lies along the in-plane [110] direction. Also consistent with the present experimental data and Landau-Ginzburg theory, the H_{eff} technique also gives a (slightly spin-canted) antiferromagnetic ground state for a large enough magnitude of compressive or tensile strains. The precise values of the critical strain leading to the transition between the cycloid of the first type and the cycloid of the second type, as well as those at which the transitions between these cycloids and the antiferromagnetic configurations occur strongly depend on the aforementioned C coefficient, but the qualitative trend is similar to that found in Landau-Ginzburg calculations.

4.3 Raman measurements under magnetic field

To shed more light on the magnetic structure of BiFeO₃ thin film, we have investigated the effect of external magnetic field on the magnetic excitations of BiFeO₃ thin films. Figures 4.11a and b show the Raman spectra of BiFeO₃ thin film on GSO and SSO substrates under external magnetic field (0-10T), respectively. The BiFeO₃ thin film on SSO shows a phase transition above 4T. Above 4T, the multi-peaks disappears which indicate the destruction of cycloidal spin structure and a new peak P_{cant} is observed. The frequency of P_{cant} is 11 cm⁻¹ which is consistent with the value of the spin-canted state. Therefore, the disappearance of multi-peaks and presence of P_{cant} proves that the magnetic structure of BiFeO₃ thin film on SSO substrate transformed from cycloidal spin to spin-canted state above 4 Tesla. This phenomenon is also observed in BiFeO₃ thin film on GSO substrate as shown in Fig. 4.11 a. The multi-peaks disappear above 6T but P_{cant} peak shows up above 4T. To analyze this issue, the peak frequencies of BiFeO₃ thin film on GSO and SSO substrates as a function of magnetic

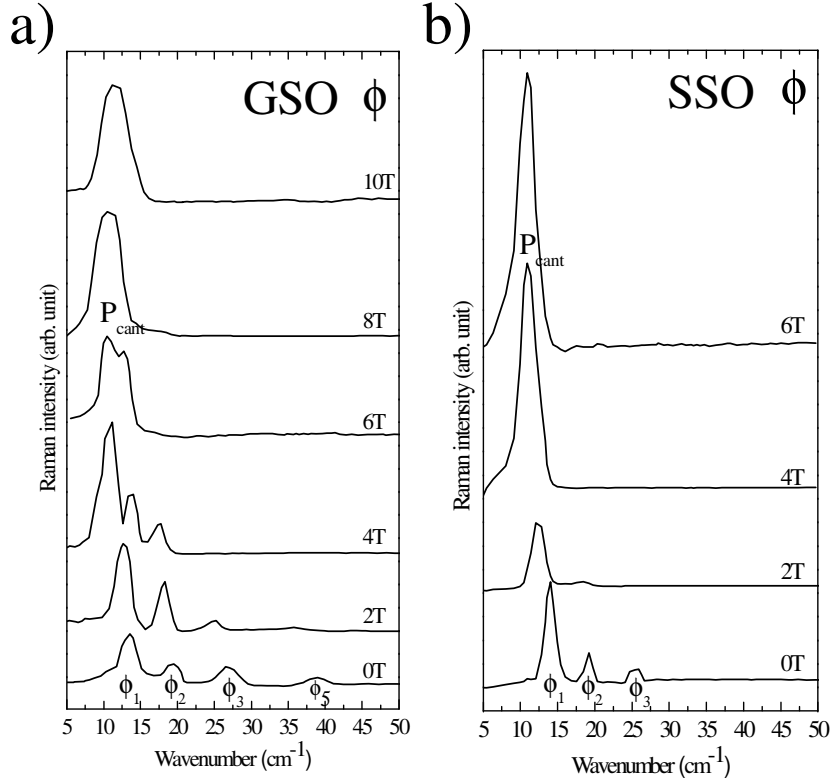


FIGURE 4.11: (a) and (b) present the Raman spectra of BiFeO_3 thin film on GSO and SSO substrates under magnetic field from 0 to 10 Tesla, respectively.

field are shown in Fig. 4.12 a and b respectively. Figure 4.12 b shows that ϕ peaks disappear and P_{cant} at 4T which clearly indicates a magnetic phase transition. Nevertheless, in the case of GSO, the situation is different. As we can see in Fig. 4.2 a, the presence P_{cant} and disappearance of ϕ peaks do not happen at the same magnetic field. In the blue zone of 4 to 6 Tesla, we can observed both the ϕ peaks and P_{cant} , which present a mix phase of cycloidal spin and spin-canted state. This result shows that the cycloid is more stable in $\text{BiFeO}_3/\text{GSO}$ substrate which has the smallest strain value.

According to Raman data under external magnetic field, the effect of magnetic field is similar to that of strain on the BiFeO_3 thin film. With increasing of magnetic field, the magnetic cycloid transforms into a spin-canted state but not into a pure AFM G-type state. Comparing with BiFeO_3 single crystal (bigger than 20 T) (Wardecki et al., 2008), it is easier to destroy the cycloidal spin in BiFeO_3 thin film (less than 10T).

Recently, an effective Hamiltonian is developed to investigate the effect of magnetic field on the magnetic cycloid of BiFeO_3 . (Rahmedov et al., 2012) In his work, the magnetic cycloid transforms into a spin-canted structure (possessing a large G-type AFM vector and a weak perpendicular magnetization) for a magnetic field around 7 Tesla when $C_{ij} = 4 \times 10^{-6}$ Hartree/(Bohr μ_B^2) and $T=5$ K. C_{ij} is coefficient of the term indi-

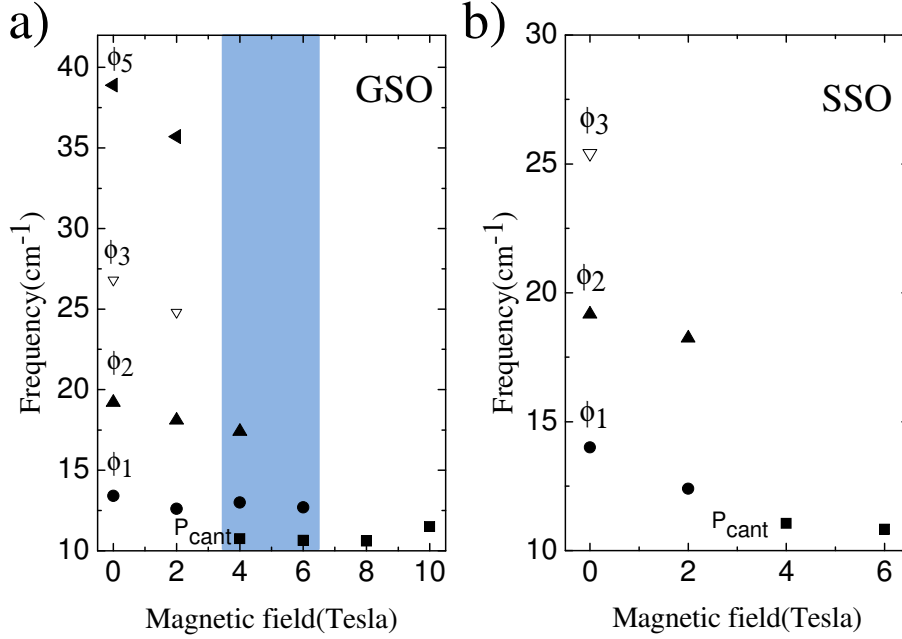


FIGURE 4.12: (a) and (b) present the peak frequencies as function of external magnetic field in BiFeO₃ thin film on GSO and SSO substrates, respectively.

cating the activation of the observed magnetic cycloid of BiFeO₃. Moreover, it is also observed that the critical magnetic field is sensitive to C_{ij} . As a result, increasing the value of C_{ij} , the critical magnetic field can be adjusted to 20 T which is consistent with the value of BiFeO₃ single crystal. (Wardecki et al., 2008) Rahmedov et al. also emphasize that the spin-canting, weak FM structure of BiFeO₃ and the magnetic cycloid are related to two different and competing energies respectively. (Rahmedov et al., 2012) The calculations are in good agreement with experimental results which can explain that the value of magnetic field needed to suppress the cycloid is a function of strain.

4.4 Conclusion

In this chapter, Raman scattering spectroscopy, conversion electron Mossbauer spectroscopy (CEMS), Landau-Ginzburg theory and effective Hamiltonian calculations are combined to investigate the effect of strain and magnetic field on the magnetic structure of BiFeO₃ thin film. The Raman measurements and CEMS results shows that while high epitaxial strain destroys the bulk-like cycloidal modulation, non-collinear orders are stable at low strain. A mixture phase of both magnetic orders is also observed in BiFeO₃ thin film on DSO substrate. In the lower-strain state, a new cycloidal spin structure (type-2) with a propagation wavevector along [110] and enlarged cycloid period is predicted and experimental observed. The homogeneous phases are energetically favorable at high compressive and tensile strain (beyond about -1.6% and +0.4%, res-

pectively) and are not pure G-type antiferromagnetic structure but a spin-canted state. The theoretical calculation indicates that the type-1 cycloid (bulk-like) is predominant in the strain range from -1.6% to +0.28%, while the type-2 cycloid exists in narrow range (from +0.28% to +0.37%). The theoretical calculations are in a great agreement with the experimental results.

The Raman spectra of BiFeO₃ thin films under external magnetic field have also been measured. A mixture phase of cycloid and spin-canted states is observed in BiFeO₃ thin film on GSO under 4-6 Tesla. The theoretical and experimental results indicate that the value of magnetic field needed to suppress the cycloid is a function of strain.

All these findings have profound implications for the implementation of BiFeO₃ films in magnonic and spintronic devices. Indeed, our Raman data reveal that strain can completely quench high energy magnon modes, offering exciting possibilities for BiFeO₃ -based magnonic devices.

Conclusion and perspectives

In this thesis, we have studied the lattice and magnetic excitations in several hexagonal RMnO₃ and BiFeO₃ thin films.

The Raman spectra of hexagonal RMnO₃ (R=Yb, Y and Ho) single crystals as a function of temperature and external magnetic field indicate the coupling of the lattice and magnetic excitations. The R-Mn and R-R interplane interactions along c-axis play an important role in the establishment of the magnetic structure of h-RMnO₃.

For YbMnO₃ single crystal, the E₂ mode at 256 cm⁻¹ and A₁ mode at 678 cm⁻¹ present an abrupt change at T_N, which indicate the coupling of lattice and spin structure. The abnormal behavior of A₁ mode clearly shows that interplane Mn-Mn interaction also plays an important role in the magnetic ordering of YbMnO₃. The spin excitations of YbMnO₃ have been observed and identified. The low frequency spectra of YbMnO₃ under external magnetic field is also observed. An abrupt decreasing of P₃ which associated to the Yb-Mn interaction at 2 T shows that the interplane Yb-Mn interaction drives the magnetic transition.

For YMnO₃ single crystal, two A₁ modes(164 and 279 cm⁻¹) and one E₂ modes at 235 cm⁻¹ present abrupt change around T_N which shows the coupling of spin and lattice ordering. Three low energy excitations are observed. The peak at 43 cm⁻¹ corresponds to the in-plane anisotropy and the peak at 24 cm⁻¹ are attributed to out-plane spin fluctuation. The peak at 36 cm⁻¹ is identified to two-magnon excitation which can be observed at 270 K (much higher than T_N around 75K). It shows the spin-liquid state in YMnO₃ single crystal.

For HoMnO₃ single crystal, two A₁ modes (267 and 686 cm⁻¹) and one E₂ modes at 237 cm⁻¹ present abrupt change around T_N which shows the coupling of spin and lattice ordering in HoMnO₃ single crystal. In low-energy Raman scattering, we observe three peaks. The peak at 41 cm⁻¹ corresponds to in-plane anisotropy. The other two peaks at 21 and 25 cm⁻¹ in 20K is attributed to crystal field excitation. The good agreement between the temperature behavior of the crystal field excitation and Ho (4b) moment below T_{SR} at 37 K indicates the Ho(4b) magnetic order is oriented mainly by the crystal field energy instead of molecular field below T_{SR}.

Raman scattering spectroscopy, conversion electron Mossbauer spectroscopy, Landau-Ginzburg theory and effective Hamiltonian calculations are combined to investigate the

effect of strain and magnetic field on the magnetic structure of BiFeO_3 thin film. While high epitaxial strain transforms the bulk-like cycloidal modulation to a spin-canted state, non-collinear orders are stable at low strain. In the lower-strain state, a new cycloidal spin structure with a propagation wavevector along $[110]$ and enlarged cycloid period is predicted and experimentally observed. A mixture phase of both magnetic orders is also observed in BiFeO_3 thin film. The homogeneous phases are energetically favorable at high compressive and tensile strain (beyond about -1.6% and $+0.4\%$, respectively) and are not pure G-type antiferromagnetic structure but a spin-canted state. The theoretical calculation indicates that the type-1 cycloid (bulk-like) is predominant in the strain range from -1.6% to $+0.28\%$, while the type-2 cycloid exists in narrow range (from $+0.28\%$ to $+0.37\%$). The theoretical calculations are in a great agreement with the experimental results. These findings have profound implications for the implementation of BiFeO_3 films in magnonic and spintronic devices. Indeed, our Raman data reveal that strain can completely quench high energy magnon modes, offering exciting possibilities for BiFeO_3 -based magnonic devices.

Bibliographie

- Aken, Bas B. van, M. A. & Palstra, T. T. M. (2001). Hexagonal ymno_3 . *Acta Crystallographica Section C*, 57(3), 230–232.
- Allibe, J., Bougot-Robin, K., Jacquet, E., Infante, I. C., Fusil, S., Carretero, C., Reverchon, J.-L., Marcilhac, B., Crete, D., Mage, J.-C., Barthelemy, A., & Bibes, M. (2010). Optical properties of integrated multiferroic bifeo_3 thin films for microwave applications. *Applied Physics Letters*, 96(18), 182902.
- Anderson, P. W. (1950). Antiferromagnetism. theory of superexchange interaction. *Phys. Rev.*, 79, 350–356.
- Arima, T., Tokunaga, A., Goto, T., Kimura, H., Noda, Y., & Tokura, Y. (2006). Collinear to spiral spin transformation without changing the modulation wavelength upon ferroelectric transition in $\text{tb}_{1-x}\text{dy}_x\text{mno}_3$. *Phys. Rev. Lett.*, 96, 097202.
- Ascher, E., Rieder, H., Schmid, H., & Stossel, H. (1966). Some properties of ferromagnetolectric nickel-iodine boracite, $\text{ni}_3\text{b}_7\text{o}_{13}\text{i}$. *Journal of Applied Physics*, 37(3), 1404–1405.
- Astrov, D. N. (1960). Discovery of the dectrically induced magnetolectric effect. *Theoret Phys*, 11, 708.
- Bai, F., Wang, J., Wuttig, M., Li, J., Wang, N., Pyatakov, A. P., Zvezdin, A. K., Cross, L. E., & Viehland, D. (2005). Destruction of spin cycloid in (111)c-oriented bifeo_3 thin films by epitaxial constraint : Enhanced polarization and release of latent magnetization. *Applied Physics Letters*, 86(3), 032511.
- Bea, H., Bibes, M., Barthelemy, A., Bouzehouane, K., Jacquet, E., Khodan, A., Contour, J.-P., Fusil, S., Wyczisk, F., Forget, A., Lebeugle, D., Colson, D., & Viret, M. (2005). Influence of parasitic phases on the properties of bifeo_3 epitaxial thin films. *Applied Physics Letters*, 87(7), 072508.
- Bea, H., Bibes, M., Ott, F., Dupe, B., Zhu, X.-H., Petit, S., Fusil, S., Deranlot, C., Bouzehouane, K., & Barthelemy, A. (2008). Mechanisms of exchange bias with multiferroic bifeo_3 epitaxial thin films. *Phys. Rev. Lett.*, 100, 017204.
- Bea, H., Bibes, M., Petit, S., Kreisel, J., & Barthelemy, A. (2007). Structural distortion and magnetism of bifeo_3 epitaxial thin films : A raman spectroscopy and neutron diffraction study. *Philosophical Magazine Letters*, 87(3-4), 165–174.

- Bea, H., Dupe, B., Fusil, S., Mattana, R., Jacquet, E., Warot-Fonrose, B., Wilhelm, F., Rogalev, A., Petit, S., Cros, V., Anane, A., Petroff, F., Bouzheouane, K., Geneste, G., Dkhil, B., Lisenkov, S., Ponomareva, I., Bellaiche, L., Bibes, M., & Barthelemy, A. (2009). Evidence for room-temperature multiferroicity in a compound with a giant axial ratio. *Phys. Rev. Lett.*, 102, 217603.
- Bertaut, E. & Mercier, M. (1963). Structure magnetique de mnyo_3 . *Physics Letters*, 5, 27.
- Bertaut, E. & Mercier, M. (1963). Structure magnetique de MnYO_3 . *Physics Letters*, 5, 27–29.
- Bertaut, E.F., Mercier, M., & Pauthenet, R. (1964). Ordre magnetique et proprietes magnetiques de mnyo_3 . *J. Phys. France*, 25(5), 550–557.
- Bibes, M. & Barthelemy, A. (2008). Multiferroics : Towards a magnetoelectric memory. *Nat Mater*, 7(6), 425–426.
- Binek, C. & Doudin, B. (2005). Magnetoelectronics with magnetoelectrics. *Journal of Physics : Condensed Matter*, 17(2), L39.
- Brown, P. J. & Chatterji, T. (2006). Neutron diffraction and polarimetric study of the magnetic and crystal structures of homno_3 and ymno_3 . *Journal of Physics : Condensed Matter*, 18(44), 10085.
- Catalan, G., Bea, H., Fusil, S., Bibes, M., Paruch, P., Barthelemy, A., & Scott, J. F. (2008). Fractal dimension and size scaling of domains in thin films of multiferroic bifeo_3 . *Phys. Rev. Lett.*, 100, 027602.
- Catalan, G. & Scott, J. F. (2009). Physics and applications of bismuth ferrite. *Advanced Materials*, 21(24), 2463–2485.
- Cazayous, M., Gallais, Y., Sacuto, A., de Sousa, Lebeugle, D., & Colson, D. (2008). Possible observation of cycloidal electromagnons in bifeo_3 . *Physical Review Letters*, 101(3), 037601.
- Chen, Y.-C., He, Q., Chu, F.-N., Huang, Y.-C., Chen, J.-W., Liang, W.-I., Vasudevan, R. K., Nagarajan, V., Arenholz, E., Kalinin, S. V., & Chu, Y.-H. (2012). Electrical control of multiferroic orderings in mixed-phase bifeo_3 films. *Advanced Materials*, 24(22), 3070–3075.
- Cheong, S.-W. & Mostovoy, M. (2007). Multiferroics : a magnetic twist for ferroelectricity. *Nat Mater*, 6(1), 13–20.
- Cho, D.-Y., Kim, J.-Y., Park, B.-G., Rho, K.-J., Park, J.-H., Noh, H.-J., Kim, B., Oh, S.-J., Park, H.-M., Ahn, J.-S., Ishibashi, H., Cheong, S.-W., Lee, J. H., Murugavel, P., Noh, T. W., Tanaka, A., & Jo, T. (2007). Ferroelectricity driven by y d^0 -ness with rehybridization in ymno_3 . *Phys. Rev. Lett.*, 98, 217601.

- Choi, K. J., Biegalski, M., Li, Y. L., Sharan, A., Schubert, J., Uecker, R., Reiche, P., Chen, Y. B., Pan, X. Q., Gopalan, V., Chen, L.-Q., Schlom, D. G., & Eom, C. B. (2004). Enhancement of ferroelectricity in strained batio₃ thin films. *Science*, 306(5698), 1005–1009.
- Choi, K.-Y., Do, S. H., Lemmens, P., Wulferding, D., Woo, C. S., Lee, J. H., Chu, K., & Yang, C.-H. (2011). Anomalous low-energy phonons in nearly tetragonal bifeo₃ thin films. *Phys. Rev. B*, 84, 132408.
- Christen, H. M., Nam, J. H., Kim, H. S., Hatt, A. J., & Spaldin, N. A. (2011). Stress-induced $r - M_A - M_C - t$ symmetry changes in bifeo₃ films. *Phys. Rev. B*, 83, 144107.
- Chu, Y.H., M. L. W. H. M. B. G. M. H. S.-J. H. Q. B. N. Y. C.-H. L. D. H. W. Z. Q. Y. P.-L. F.-R. A. S. A. W. S. X. & Ramesh, R. (2008). Electric-field control of local ferromagnetism using a magnetoelectric multiferroic. *Nat Mater*, 7(6), 478–482.
- Cohen, R. E. (1992). Origin of ferroelectricity in perovskite oxides. *Nature*, 358(6382), 136–138.
- Curie, P. (1894). Sur la symétrie dans les phénomènes physiques, symétrie d'un champ électrique et d'un champ magnétique. *J. Phys. Theor. Appl.*, 3, 393.
- Daumont, C., Ren, W., Infante, I. C., Lisenkov, S., Allibe, J., Carrtaaro, C., Fusil, S., Jacquet, E., Bouvet, T., Bouamrane, F., Prosandeev, S., Geneste, G., Dkhil, B., Bellaiche, L., Barthalamy, A., & Bibes, M. (2012). Strain dependence of polarization and piezoelectric response in epitaxial bifeo₃ thin films. *Journal of Physics : Condensed Matter*, 24(16), 162202.
- de Sousa, R., Allen, M., & Cazayous, M. (2012). Theory of spin-orbit enhanced electric-field control of magnetism in multiferroic bifeo₃. *ArXiv e-prints*.
- de Sousa, R. & Moore, J. E. (2008a). Electrical control of magnon propagation in multiferroic bifeo₃ films. *Applied Physics Letters*, 92(2), 022514.
- de Sousa, R. & Moore, J. E. (2008b). Optical coupling to spin waves in the cycloidal multiferroic bifeo₃. *Phys. Rev. B*, 77, 012406.
- Debye, P. (1926). Einige bemerkungen zur magnetisierung bei tiefer temperatur. *Annalen der Physik*, 386(25), 1154–1160.
- dela Cruz, C., Yen, F., Lorenz, B., Wang, Y. Q., Sun, Y. Y., Gospodinov, M. M., & Chu, C. W. (2005). Strong spin-lattice coupling in multiferroic homn₃ : Thermal expansion anomalies and pressure effect. *Phys. Rev. B*, 71, 060407.
- Demmel, F. & Chatterji, T. (2007). Persistent spin waves above the néel temperature in ymno₃. *Phys. Rev. B*, 76, 212402.

- Devonshire, A. (1949). Theory of barium titanate. *Philosophical Magazine Series 7*, 40(309), 1040–1063.
- Devonshire, A. (1954). Theory of ferroelectrics. *Advances in Physics*, 3(10), 85–130.
- Dupe, B., Infante, I. C., Geneste, G., Janolin, P.-E., Bibes, M., Barthelemy, A., Lisenkov, S., Bellaiche, L., Ravy, S., & Dkhil, B. (2010). Competing phases in bifeo₃ thin films under compressive epitaxial strain. *Phys. Rev. B*, 81, 144128.
- Dzyaloshinskii, I. (1959). On the magneto-elastic effect in antiferromagnets. *Sov. Phys. JETP*, 10, 628.
- Dzyaloshinsky, I. (1958). A thermodynamic theory of a weak ferromagnetism of anti-ferromagnetics. *Journal of Physics and Chemistry of Solids*, 4(4), 241 – 255.
- Ederer, C. & Spaldin, N. A. (2005). Effect of epitaxial strain on the spontaneous polarization of thin film ferroelectrics. *Phys. Rev. Lett.*, 95, 257601.
- Eerenstein, W., Morrison, F. D., Dho, J., Blamire, M. G., Scott, J. F., & Mathur, N. D. (2005). Comment on "epitaxial bifeo₃ multiferroic thin film heterostructures". *Science*, 307(5713), 1203.
- E.F Bertaut, J. M. (1967). Etude de la structure magnetique des chromites d'erbium et de neodyme par diffraction neutronique. *Solid State Communications*, 5, 93.
- Efremov, D. V., van den Brink, J., & Khomskii, D. I. (2004). Bond- versus site-centred ordering and possible ferroelectricity in manganites. *Nat Mater*, 3(12), 853–856.
- Fabreges, X. (2010). *Etude des proprietes magnetiques et du couplage spin/reseau dans les composes multiferroiques RMnO3 hexagonaux par diffusion de neutrons*.
- Fabreges, X., Mirebeau, I., Bonville, P., Petit, S., G., L.-J., Forget, A., Andre, G., & Pailhes, S. (2008). Magnetic order in ybmno₃ studied by neutron diffraction and mossbauer spectroscopy. *Phys. Rev. B*, 78, 214422.
- Fabreges, X., Petit, S., Mirebeau, I., Pailhes, S., Pinsard, L., Forget, A., Fernandez-Diaz, M. T., & Porcher, F. (2009). Spin-lattice coupling, frustration, and magnetic order in multiferroic rmno₃. *Phys. Rev. Lett.*, 103, 067204.
- Fennie, C. J. (2008). Ferroelectrically induced weak ferromagnetism by design. *Phys. Rev. Lett.*, 100, 167203.
- Fiebig, M. (2005). Revival of the magnetoelectric effect. *Journal of Physics D : Applied Physics*, 38(8), R123.
- Fiebig, M., Frohlich, D., Kohn, K., Leute, S., Lottermoser, T., Pavlov, V. V., & Pisarev, R. V. (2000a). Determination of the magnetic symmetry of hexagonal manganites by second harmonic generation. *Phys. Rev. Lett.*, 84, 5620–5623.

- Fiebig, M., Frohlich, D., Lottermoser, T., & Kohn, K. (2000b). Spin-angle topography of hexagonal manganites by magnetic second-harmonic generation. *Applied Physics Letters*, 77(26), 4401–4403.
- Fiebig, M., Frohlich, D., Lottermoser, T., & Maat, M. (2002a). Probing of ferroelectric surface and bulk domains in rmno_3 ($r=y$, ho) by second harmonic generation. *Phys. Rev. B*, 66, 144102.
- Fiebig, M., Lottermoser, T., Frohlich, D., Goltsev, A. V., & Pisarev, R. V. (2002b). Observation of coupled magnetic and electric domains. *Nature*, 419(6909), 818–820.
- Fishman, R. S., Furukawa, N., Haraldsen, J. T., Matsuda, M., & Miyahara, S. (2012). Identifying the magnetoelectric modes of multiferroic bifeo_3 . *ArXiv e-prints*.
- Fleury, P. A. & Porto, S. P. S. (1968). Light scattering by spin waves. *Journal of Applied Physics*, 39(2), 1035–1041.
- Frohlich, D., Leute, S., Pavlov, V. V., & Pisarev, R. V. (1998). Nonlinear optical spectroscopy of the two-order-parameter compound ymno_3 . *Phys. Rev. Lett.*, 81, 3239–3242.
- Fukumura, H., Hasuike, N., Harima, H., Kisoda, K., Fukae, K., Yoshimura, T., & Fujimura, N. (2009). Spin-phonon coupling in multiferroic ybmno_3 studied by raman scattering. *Journal of Physics : Condensed Matter*, 21(6), 064218.
- Fukumura, H., Matsui, S., Harima, H., Kisoda, K., Takahashi, T., Yoshimura, T., & Fujimura, N. (2007). Raman scattering studies on multiferroic ymno_3 . *Journal of Physics : Condensed Matter*, 19(36), 365239.
- Gajek, M., Bibes, M., Fusil, S., Bouzouane, K., Fontcuberta, J., Barthelemy, A., & Fert, A. (2007). Tunnel junctions with multiferroic barriers. *Nat Mater*, 6(4), 296–302.
- Goto, T., Kimura, T., Lawes, G., Ramirez, A. P., & Tokura, Y. (2004). Ferroelectricity and giant magnetocapacitance in perovskite rare-earth manganites. *Physical Review Letters*, 92, 257201.
- Haeni, J. H., Irvin, P., Chang, W., Uecker, R., Reiche, P., Li, Y. L., Choudhury, S., Tian, W., Hawley, M. E., Craigo, B., Tagantsev, A. K., Pan, X. Q., Streiffer, S. K., Chen, L. Q., Kirchoefer, S. W., Levy, J., & Schlom, D. G. (2004). Room-temperature ferroelectricity in strained srtio_3 . *Nature*, 430(7001), 758–761.
- Haumont, R., Kornev, I. A., Lisenkov, S., Bellaiche, L., Kreisel, J., & Dkhil, B. (2008). Phase stability and structural temperature dependence in powdered multiferroic bifeo_3 . *Phys. Rev. B*, 78, 134108.
- Hayes, W. & Loudon, R. (1978). *Scattering of light by crystals*. Dover publications Inc.

- Hermet, P., Goffinet, M., Kreisel, J., & Ghosez, P. (2007). Raman and infrared spectra of multiferroic bismuth ferrite from first principles. *Phys. Rev. B*, 75, 220102.
- Hill, N. A. (2000). Why are there so few magnetic ferroelectrics? *The Journal of Physical Chemistry B*, 104(29), 6694–6709.
- Huang, Z. J., Cao, Y., Sun, Y. Y., Xue, Y. Y., & Chu, C. W. (1997). Coupling between the ferroelectric and antiferromagnetic orders in ymno_3 . *Phys. Rev. B*, 56, 2623–2626.
- Hur, N., Park, S., Sharma, P. A., Ahn, J. S., Guha, S., & Cheong, S.-W. (2004). Electric polarization reversal and memory in a multiferroic material induced by magnetic fields. *Nature*, 429(6990), 392–395.
- Ikeda, N., Ohsumi, H., Ohwada, K., Ishii, K., Inami, T., Kakurai, K., Murakami, Y., Yoshii, K., Mori, S., Horibe, Y., & Kito, H. (2005). Ferroelectricity from iron valence ordering in the charge-frustrated system lufe_2o_4 . *Nature*, 436(7054), 1136–1138.
- Iliev, M. N., Lee, H.-G., Popov, V. N., Abrashev, M. V., Hamed, A., Meng, R. L., & Chu, C. W. (1997). Raman- and infrared-active phonons in hexagonal ymno_3 : Experiment and lattice-dynamical calculations. *Phys. Rev. B*, 56, 2488–2494.
- Infante, I. C., Lisenkov, S., Dupe, B., Bibes, M., Fusil, S., Jacquet, E., Geneste, G., Petit, S., Courtial, A., Juraszek, J., Bellaiche, L., Barthelemy, A., & Dkhil, B. (2010). Bridging multiferroic phase transitions by epitaxial strain in bifeo_3 . *Phys. Rev. Lett.*, 105, 057601.
- Ishiwata, S., Kaneko, Y., Tokunaga, Y., Taguchi, Y., Arima, T.-h., & Tokura, Y. (2010). Perovskite manganites hosting versatile multiferroic phases with symmetric and antisymmetric exchange strictions. *Phys. Rev. B*, 81, 100411.
- Ishiwata, S., Tokunaga, Y., Taguchi, Y., & Tokura, Y. (2011). High-pressure hydrothermal crystal growth and multiferroic properties of a perovskite ymno_3 . *Journal of the American Chemical Society*, 133(35), 13818–13820.
- Jahn, H. A. & Teller, E. (1937). Stability of polyatomic molecules in degenerate electronic states. i. orbital degeneracy. *Proceedings of the Royal Society of London. Series A, Mathematical and Physical Sciences*, 161(905), 220–235.
- Jang, H. W., Baek, S. H., Ortiz, D., Folkman, C. M., Das, R. R., Chu, Y. H., Shafer, P., Zhang, J. X., Choudhury, S., Vaithyanathan, V., Chen, Y. B., Felker, D. A., Biegalski, M. D., Rzechowski, M. S., Pan, X. Q., Schlom, D. G., Chen, L. Q., Ramesh, R., & Eom, C. B. (2008). Strain-induced polarization rotation in epitaxial (001) bifeo_3 thin films. *Phys. Rev. Lett.*, 101, 107602.
- Jeong, J., Goremychkin, E. A., Guidi, T., Nakajima, K., Jeon, G. S., Kim, S.-A., Furukawa, S., Kim, Y. B., Lee, S., Kiryukhin, V., Cheong, S.-W., & Park, J.-G. (2012). Spin wave measurements over the full brillouin zone of multiferroic bifeo_3 . *Phys. Rev. Lett.*, 108, 077202.

- Kadlec, C., Goian, V., Rushchanskii, K. Z., Kužel, P., Ležaić, M., Kohn, K., Pisarev, R. V., & Kamba, S. (2011). Terahertz and infrared spectroscopic evidence of phonon-paramagnon coupling in hexagonal piezomagnetic ymno_3 . *Phys. Rev. B*, 84, 174120.
- Kadomtseva, A., Zvezdin, A., Popov, Y., Pyatakov, A., & Vorobaev, G. (2004). Space-time parity violation and magnetoelectric interactions in antiferromagnets. *JETP Letters*, 79, 571–581. 10.1134/1.1787107.
- Katsufuji, T., Masaki, M., Machida, A., Moritomo, M., Kato, K., Nishibori, E., Takata, M., Sakata, M., Ohoyama, K., Kitazawa, K., & Takagi, H. (2002). Crystal structure and magnetic properties of hexagonal rmno_3 ($r=y, \text{lu}$, and sc) and the effect of doping. *Phys. Rev. B*, 66, 134434.
- Katsura, H., Nagaosa, N., & Balatsky, A. V. (2005). Spin current and magnetoelectric effect in noncollinear magnets. *Phys. Rev. Lett.*, 95, 057205.
- Ke, X., Zhang, P. P., Baek, S. H., Zarestky, J., Tian, W., & Eom, C. B. (2010). Magnetic structure of epitaxial multiferroic bifeo_3 films with engineered ferroelectric domains. *Phys. Rev. B*, 82, 134448.
- Kenzelmann, M., Harris, A. B., Jonas, S., Broholm, C., Schefer, J., Kim, S. B., Zhang, C. L., Cheong, S.-W., Vajk, O. P., & Lynn, J. W. (2005). Magnetic inversion symmetry breaking and ferroelectricity in tbmno_3 . *Phys. Rev. Lett.*, 95, 087206.
- Khomskii, D. (2009). Classifying multiferroics : Mechanisms and effects. *Physics*, 2, 20.
- Kimura, T., Goto, T., Shintani, H., Ishizaka, K., Arima, T., & Tokura, Y. (2003a). Magnetic control of ferroelectric polarization. *Nature*, 426(6962), 55–58.
- Kimura, T., Ishihara, S., Shintani, H., Arima, T., Takahashi, K. T., Ishizaka, K., & Tokura, Y. (2003b). Distorted perovskite with e_g^1 configuration as a frustrated spin system. *Phys. Rev. B*, 68, 060403.
- Kozlenko, D., Kichanov, S., Lee, S., Park, J.-G., Glazkov, V., & Savenko, B. (2005). High-pressure effect on the crystal and magnetic structures of the frustrated antiferromagnet ymno_3 . *Journal of Experimental and Theoretical Physics Letters*, 82, 193–197.
- Kozlenko, D., Kichanov, S., Lee, S., Park, J.-G., Glazkov, V., & Savenko, B. (2006). High-pressure effect on the crystal and magnetic structure of lumno_3 : Correlation between a distortion of the triangular lattice and the symmetry of the magnetic state in hexagonal frustrated manganites. *Journal of Experimental and Theoretical Physics Letters*, 83, 346–350.
- Kozlenko, D. P., Kichanov, S. E., Lee, S., Park, J.-G., & Savenko, B. N. (2007). Pressure-induced spin fluctuations and spin reorientation in hexagonal manganites. *Journal of Physics : Condensed Matter*, 19(15), 156228.

- Kramers, H. A. (1934). L'interaction entre les atomes magnetogenes dans un cristal paramagnetique. *Physica*, 1, 182–192.
- Landau, L. D. & Lifshitz, E. M. (1969). *Statistical physics. Pt.1*.
- Landsberg, G. & Mandelstam, L. (1928). Eine neue erscheinung bei der lichtzerstreuung in krystallen. *Naturwissenschaften*, 16, 557–558.
- Laukhin, V., Skumryev, V., Marti, X., Hrabovsky, D., Sanchez, F., Garcia-Cuenca, M. V., Ferrater, C., Varela, M., Luders, U., Bobo, J. F., & Fontcuberta, J. (2006). Electric-field control of exchange bias in multiferroic epitaxial heterostructures. *Phys. Rev. Lett.*, 97, 227201.
- Lebeugle, D., Colson, D., Forget, A., Viret, M., Bataille, A. M., & Gukasov, A. (2008). Electric-field-induced spin flop in bifeo₃ single crystals at room temperature. *Phys. Rev. Lett.*, 100, 227602.
- Lebeugle, D., Colson, D., Forget, A., Viret, M., Bonville, P., Marucco, J. F., & Fusil, S. (2007). Room-temperature coexistence of large electric polarization and magnetic order in bifeo₃ single crystals. *Phys. Rev. B*, 76, 024116.
- Lee, J. H., Fang, L., Vlahos, E., Ke, X., Jung, Y. W., Kourkoutis, L. F., Kim, J.-W., Ryan, P. J., Heeg, T., Roeckerath, M., Goian, V., Bernhagen, M., Uecker, R., Hammel, P. C., Rabe, K. M., Kamba, S., Schubert, J., Freeland, J. W., Muller, D. A., Fennie, C. J., Schiffer, P., Gopalan, V., Johnston-Halperin, E., & Schlom, D. G. (2010). A strong ferroelectric ferromagnet created by means of spin-lattice coupling. *Nature*, 466(7309), 954–958.
- Lee, N., Choi, Y. J., Ramazanoglu, M., Ratcliff, W., Kiryukhin, V., & Cheong, S.-W. (2011). Mechanism of exchange striction of ferroelectricity in multiferroic orthorhombic homno₃ single crystals. *Phys. Rev. B*, 84, 020101.
- Lee, S., Pirogov, A., Han, J. H., Park, J.-G., Hoshikawa, A., & Kamiyama, T. (2005). Direct observation of a coupling between spin, lattice and electric dipole moment in multiferroic ymno₃. *Phys. Rev. B*, 71, 180413.
- Lee, S., Pirogov, A., Kang, M., Jang, K.-H., Yonemura, M., Kamiyama, T., Cheong, S.-W., Gozzo, F., Shin, N., Kimura, H., Noda, Y., & Park, J.-G. (2008). Giant magneto-elastic coupling in multiferroic hexagonal manganites. *Nature*, 451(7180), 805–808.
- Litvinchuk, A. P., Iliev, M. N., Popov, V. N., & Gospodinov, M. M. (2004). Raman and infrared-active phonons in hexagonal homno₃ single crystals : magnetic ordering effects. *Journal of Physics : Condensed Matter*, 16(6), 809.
- Lonkai, T., Hohlwein, D., Ihringer, J., & Prandl, W. (2002). The magnetic structures of ymno₃ and homno₃. *Applied Physics A : Materials Science and Processing*, 74, s843–s845. 10.1007/s003390101158.

- Lonkai, T., Tomuta, D. G., Hoffmann, J.-U., Schneider, R., Hohlwein, D., & Ihringer, J. (2003). Magnetic two-dimensional short-range order in hexagonal manganites. *Journal of Applied Physics*, 93(10), 8191–8193.
- Lorenz, B., Wang, Y.-Q., & Chu, C.-W. (2007). Ferroelectricity in perovskite homn_3 and ymno_3 . *Phys. Rev. B*, 76, 104405.
- Lottermoser, T., Lonkai, T., Amann, U., Hohlwein, D., Ihringer, J., & Fiebig, M. (2004). Magnetic phase control by an electric field. *Nature*, 430(6999), 541–544.
- Loudon, R. (1970). The propagation of electromagnetic energy through an absorbing dielectric. *Journal of Physics A : General Physics*, 3(3), 233.
- MacDougall, G. J., Christen, H. M., Siemons, W., Biegalski, M. D., Zarestky, J. L., Liang, S., Dagotto, E., & Nagler, S. E. (2012). Antiferromagnetic transitions in tetragonal-like bifeo_3 . *Phys. Rev. B*, 85, 100406.
- Malashevich, A. & Vanderbilt, D. (2008). First principles study of improper ferroelectricity in tbmno_3 . *Phys. Rev. Lett.*, 101, 037210.
- Matsuda, M., Fishman, R. S., Hong, T., Lee, C. H., Ushiyama, T., Yanagisawa, Y., Tomioka, Y., & Ito, T. (2012). Magnetic dispersion and anisotropy in multiferroic bifeo_3 . *Phys. Rev. Lett.*, 109, 067205.
- Mochizuki, M. & Furukawa, N. (2009). Microscopic model and phase diagrams of the multiferroic perovskite manganites. *Phys. Rev. B*, 80, 134416.
- Monceau, P., Nad, F. Y., & Brazovskii, S. (2001). Ferroelectric mott-hubbard phase of organic $(\text{TMTTF})_2X$ conductors. *Phys. Rev. Lett.*, 86, 4080–4083.
- Moreau, J., Michel, C., Gerson, R., & James, W. (1971). Ferroelectric bifeo_3 x-ray and neutron diffraction study. *Journal of Physics and Chemistry of Solids*, 32(6), 1315 – 1320.
- Moriya, T. (1960). Anisotropic superexchange interaction and weak ferromagnetism. *Phys. Rev.*, 120, 91–98.
- Munoz, A., Alonso, J. A., Martanez-Lope, M. J., Cassis, M. T., Martanez, J. L., & Fernandez-Diaz, M. T. (2001a). Evolution of the magnetic structure of hexagonal homno_3 from neutron powder diffraction data. *Chemistry of Materials*, 13(5), 1497–1505.
- Munoz, A., Alonso, J. A., Martinez-Lope, M. J., Casais, M. T., Martinez, J. L., & Fernandez-Diaz, M. T. (2000). Magnetic structure of hexagonal rmno_3 $r=y,sc$: Thermal evolution from neutron powder diffraction data. *Phys. Rev. B*, 62, 9498–9510.

- Munoz, A. A., Cassis, M. T., Alonso, J. A., Martanez-Lope, M. J., Martanez, J. L., & Fernandez-Daaz, M. T. (2001b). Complex magnetism and magnetic structures of the metastable homno_3 perovskite. *Inorganic Chemistry*, 40(5), 1020–1028.
- Naganuma, H. & Okamura, S. (2007). Structural, magnetic, and ferroelectric properties of multiferroic bifeo_3 film fabricated by chemical solution deposition. *Journal of Applied Physics*, 101(9), 09M103.
- Pailhes, S., Fabreges, X., Regnault, L. P., Pinsard-Godart, L., Mirebeau, I., Moussa, F., Hennion, M., & Petit, S. (2009). Hybrid goldstone modes in multiferroic ymno_3 studied by polarized inelastic neutron scattering. *Phys. Rev. B*, 79, 134409.
- Palai, R., Katiyar, R. S., Schmid, H., Tissot, P., Clark, S. J., Robertson, J., Redfern, S. A. T., Catalan, G., & Scott, J. F. (2008). β phase and γ - β metal-insulator transition in multiferroic bifeo_3 . *Phys. Rev. B*, 77, 014110.
- Petit, S., Moussa, F., Hennion, M., Pailhes, S., Pinsard-Gaudart, L., & Ivanov, A. (2007). Spin phonon coupling in hexagonal multiferroic ymno_3 . *Phys. Rev. Lett.*, 99, 266604.
- Picozzi, S. & Ederer, C. (2009). First principles studies of multiferroic materials. *Journal of Physics : Condensed Matter*, 21(30), 303201.
- Picozzi, S., Yamauchi, K., Sanyal, B., Sergienko, I. A., & Dagotto, E. (2007). Dual nature of improper ferroelectricity in a magnetoelectric multiferroic. *Phys. Rev. Lett.*, 99, 227201.
- Pimenov, A., Mukhin, A. A., Ivanov, V. Y., Travkin, V. D., Balbashov, A. M., & Loidl, A. (2006). Possible evidence for electromagnons in multiferroic manganites. *Nat Phys*, 2(2), 97–100.
- Popov, Y. F., Kadomtseva, A. M., Krotov, S. S., Belov, D. V., Vorobev, G. P., Makhov, P. N., & Zvezdin, A. K. (2001). Features of the magnetoelectric properties of bifeo_3 in high magnetic fields. *Low Temperature Physics*, 27, 478.
- Popov, Y. F., Zvezdin, A. K., Vorobev, G. P., Kadomtseva, A. M., Murashev, V. A., & Rakov, D. N. (1993). Linear magnetoelectric effect and phase transitions in bismuth ferrite, bifeo_3 . *JETP Letter*, 57, 69.
- Porto, S. P. S., Giordmaine, J. A., & Damen, T. C. (1966). Depolarization of raman scattering in calcite. *Physical Review*, 147, 608.
- Prosandeev, S., Kornev, I. A., & Bellaiche, L. (2011). Magnetoelectricity in bifeo_3 films : First-principles-based computations and phenomenology. *Phys. Rev. B*, 83, 020102.
- Pytte, E. & Feder, J. (1969). Theory of a structural phase transition in perovskite-type crystals. *Phys. Rev.*, 187, 1077–1088.

- Rahmedov, D., Wang, D., Iniguez, J., & Bellaiche, L. (2012). Magnetic cycloid of bifeo₃ from atomistic simulations. *Phys. Rev. Lett.*, 109, 037207.
- Ramazanoglu, M., Laver, M., Ratcliff, W., Watson, S. M., Chen, W. C., Jackson, A., Kothapalli, K., Lee, S., Cheong, S.-W., & Kiryukhin, V. (2011). Local weak ferromagnetism in single-crystalline ferroelectric bifeo₃. *Phys. Rev. Lett.*, 107, 207206.
- Rana, D. S., Takahashi, K., Mavani, K. R., Kawayama, I., Murakami, H., Tonouchi, M., Yanagida, T., Tanaka, H., & Kawai, T. (2007). Thickness dependence of the structure and magnetization of bifeo₃ thin films on laalo_{30.3}sr₂altao_{60.7} (001) substrate. *Phys. Rev. B*, 75, 060405.
- Ridley, B. K. (1993). *quantum processes in semiconductors*. oxford university.
- Rontgen, W. C. (1888). Uber die durch bewegung eines im homogen electrischen felde befindlichen dielectricums hervorgerufene electrodynamische kraft. *Ann. Phys. Chem*, 35, 264.
- Rossell, M. D., Erni, R., Prange, M. P., Idrobo, J.-C., Luo, W., Zeches, R. J., Pantelides, S. T., & Ramesh, R. (2012). Atomic structure of highly strained bifeo₃ thin films. *Phys. Rev. Lett.*, 108, 047601.
- Rovillain, P., de Sousa, R., Gallais, Y., Sacuto, A., Measson, M. A., Colson, D., Forget, A., Bibes, M., Barthalamy, A., & Cazayous, M. (2010). Electric-field control of spin waves at room temperature in multiferroic bifeo₃. *Nat Mater*, 9(12), 975–979.
- Sato, T. J., Lee, S. H., Katsufuji, T., Masaki, M., Park, S., Copley, J. R. D., & Takagi, H. (2003). Unconventional spin fluctuations in the hexagonal antiferromagnet ymno₃. *Phys. Rev. B*, 68, 014432.
- Schmid, H. (1994). Multi-ferroic magnetoelectrics. *Ferroelectrics*, **162**, 317.
- Scott, J. F. (1974). Soft-mode spectroscopy : Experimental studies of structural phase transitions. *Review of Modern Physics*, **46**, 83.
- Seidel, J., Martin, L. W., He, Q., Zhan, Q., Chu, Y.-H., Rother, A., Hawkrige, M. E., Maksymovych, P., Yu, P., Gajek, M., Balke, N., Kalinin, S. V., Gemming, S., Wang, F., Catalan, G., Scott, J. F., Spaldin, N. A., Orenstein, J., & Ramesh, R. (2009). Conduction at domain walls in oxide multiferroics. *Nat Mater*, 8(3), 229–234.
- Selbach, S. M., Tybell, T., Einarsrud, M.-A., & Grande, T. (2008). The ferroic phase transitions of bifeo₃. *Advanced Materials*, 20(19), 3692–3696.
- Sergienko, I. A., Cengiz, & Dagotto, E. (2006). Ferroelectricity in the magnetic e-phase of orthorhombic perovskites. *Phys. Rev. Lett.*, 97, 227204.

- Setter, N., Damjanovic, D., Eng, L., Fox, G., Gevorgian, S., Hong, S., Kingon, A., Kohlstedt, H., Park, N. Y., Stephenson, G. B., Stolitchnov, I., Taganstev, A. K., Taylor, D. V., Yamada, T., & Streiffer, S. (2006). Ferroelectric thin films : Review of materials, properties, and applications. *Journal of Applied Physics*, 100(5), 051606.
- Sharma, P. A., Ahn, J. S., Hur, N., Park, S., Kim, S. B., Lee, S., Park, J.-G., Guha, S., & Cheong, S.-W. (2004). Thermal conductivity of geometrically frustrated, ferroelectric ymno_3 : Extraordinary spin-phonon interactions. *Phys. Rev. Lett.*, 93, 177202.
- Singh, M. K., Katiyar, R. S., & Scott, J. F. (2008). New magnetic phase transitions in bifeo_3 . *Journal of Physics : Condensed Matter*, 20(25), 252203.
- Singh, R. (2002). C. v. raman and the discovery of the raman effect. *Physics in Perspective*, 4, 399–420.
- Smekal, A. (1923). Zur quantentheorie der dispersion. *Naturwissenschaften*, 11, 873–875.
- Solovyev, I. V., Valentyuk, M. V., & Mazurenko, V. V. (2012). Magnetic structure of hexagonal ymno_3 and lumno_3 from a microscopic point of view. *Phys. Rev. B*, 86, 054407.
- Sosnowska, I., Neumaier, T. P., & Steichele, E. (1982). Spiral magnetic ordering in bismuth ferrite. *Journal of Physics C : Solid State Physics*, 15(23), 4835.
- Sosnowska, I. & Zvezdin, A. (1995). Origin of the long period magnetic ordering in bifeo_3 . *Journal of Magnetism and Magnetic Materials*, 140–144, Part 1(0), 167 – 168. <ce :title>International Conference on Magnetism</ce :title>.
- Spaldin, N. A. & Fiebig, M. (2005). The renaissance of magnetoelectric multiferroics. *Science*, 309(5733), 391–392.
- Spitzer, W. G., Miller, R. C., Kleinman, D. A., & Howarth, L. E. (1962). Far infrared dielectric dispersion in batio_3 , srtio_3 , and tio_2 . *Phys. Rev.*, 126, 1710–1721.
- Standard, E. C., Stanislavchuk, T., Sirenko, A. A., Lee, N., & Cheong, S.-W. (2012). Magnons and crystal-field transitions in hexagonal rmno_3 (r = er, tm, yb, lu) single crystals. *Phys. Rev. B*, 85, 144422.
- Talbayev, D., Trugman, S. A., Lee, S., Yi, H. T., Cheong, S.-W., & Taylor, A. J. (2011). Long-wavelength magnetic and magnetoelectric excitations in the ferroelectric anti-ferromagnet bifeo_3 . *Phys. Rev. B*, 83, 094403.
- Vajk, O. P., Kenzelmann, M., Lynn, J. W., Kim, S. B., & Cheong, S.-W. (2005). Magnetic order and spin dynamics in ferroelectric homno_3 . *Phys. Rev. Lett.*, 94, 087601.
- Vermette, J., Jandl, S., & Gospodinov, M. M. (2008). Raman study of spin-phonon coupling in ermno_3 . *Journal of Physics : Condensed Matter*, 20(42), 425219.

- Vermette, J., Jandl, S., Mukhin, A. A., Ivanov, V. Y., Balbashov, A., Gospodinov, M. M., & Pinsard-Gaudart, L. (2010). Raman study of the antiferromagnetic phase transitions in hexagonal ymno_3 and lumno_3 . *Journal of Physics : Condensed Matter*, 22(35), 356002.
- Walker, H. C., Fabrizi, F., Paolasini, L., de Bergevin, F., Herrero-Martin, J., Boothroyd, A. T., Prabhakaran, D., & McMorrow, D. F. (2011). Femtoscale magnetically induced lattice distortions in multiferroic tbmno_3 . *Science*, 333(6047), 1273–1276.
- Wang, D., Weerasinghe, J., & Bellaiche, L. (2012). Atomistic molecular dynamic simulations of multiferroics. *Phys. Rev. Lett.*, 109, 067203.
- Wang, J., Neaton, J. B., Zheng, H., Nagarajan, V., Ogale, S. B., Liu, B., Viehland, D., Vaithyanathan, V., Schlom, D. G., Waghmare, U. V., Spaldin, N. A., Rabe, K. M., Wuttig, M., & Ramesh, R. (2003). Epitaxial bifeo_3 multiferroic thin film heterostructures. *Science*, 299(5613), 1719–1722.
- Wang, J., Scholl, A., Zheng, H., Ogale, S. B., Viehland, D., Schlom, D. G., Spaldin, N. A., Rabe, K. M., Wuttig, M., Mohaddes, L., Neaton, J., Waghmare, U., Zhao, T., & Ramesh, R. (2005). Response to comment on "epitaxial bifeo_3 multiferroic thin film heterostructures". *Science*, 307(5713), 1203.
- Wardecki, D., Przenioso, R., Sosnowska, I., Skourski, Y., & Loewenhaupt, M. (2008). Magnetization of polycrystalline bifeo_3 in high magnetic fields. *Journal of the Physical Society of Japan*, 77(10), 103709.
- Wojdel, J. C. & Iniguez, J. (2010). Ab initio indications for giant magnetoelectric effects driven by structural softness. *Phys. Rev. Lett.*, 105, 037208.
- Wollan, E. O. & Koehler, W. C. (1955). Neutron diffraction study of the magnetic properties of the series of perovskite-type compounds $(1-x)\text{laxcamno}_3$. *Phys. Rev.*, 100, 545–563.
- Wu, S. M., Cybart, S. A., Yu, P., Rossell, M. D., Zhang, J. X., Ramesh, R., & Dynes, R. C. (2010). Reversible electric control of exchange bias in a multiferroic field-effect device. *Nat Mater*, 9(9), 756–761.
- Yamauchi, K., Freimuth, F., Blügel, S., & Picozzi, S. (2008). Magnetically induced ferroelectricity in orthorhombic manganites : Microscopic origin and chemical trends. *Phys. Rev. B*, 78, 014403.
- Yang, F., Tang, M. H., Ye, Z., Zhou, Y. C., Zheng, X. J., Tang, J. X., Zhang, J. J., & He, J. (2007). Eight logic states of tunneling magnetoelectroresistance in multiferroic tunnel junctions. *Journal of Applied Physics*, 102(4), 044504.
- Yang, S. Y., Martin, L. W., Byrnes, S. J., Conry, T. E., Basu, S. R., Paran, D., Reichertz, L., Ihlefeld, J., Adamo, C., Melville, A., Chu, Y.-H., Yang, C.-H., Musfeldt, J. L., Schlom, D. G., Ager, J. W., III, & Ramesh, R. (2009). Photovoltaic effects in bifeo_3 . *Applied Physics Letters*, 95(6), 062909.

- Yen, F., dela Cruz, C. R., Lorenz, B., Sun, Y. Y., Wang, Y. Q., Gospodinov, M. M., & Chu, C. W. (2005). Low-temperature dielectric anomalies in homno_3 : The complex phase diagram. *Phys. Rev. B*, 71, 180407.
- Yu, P. Y. & Cardona, M. (1999). *Fundamentals of semiconductors*. Springer-Verlag, Berlin.
- Yu, P. Y., Cardona, M., & Sham, L. J. (1997). Fundamentals of Semiconductors : Physics and Materials Properties. *Physics Today*, 50, 76.
- Zalessky, A. V., Frolov, A. A., Khimich, T. A., Bush, A. A., Pokatilov, V. S., & Zvezdin, A. K. (2000). 57 fe nmr study of spin-modulated magnetic structure in bifeo₃. *EPL (Europhysics Letters)*, 50(4), 547.
- Zeches, R. J., Rossell, M. D., Zhang, J. X., Hatt, A. J., He, Q., Yang, C.-H., Kumar, A., Wang, C. H., Melville, A., Adamo, C., Sheng, G., Chu, Y.-H., Ihlefeld, J. F., Erni, R., Ederer, C., Gopalan, V., Chen, L. Q., Schlom, D. G., Spaldin, N. A., Martin, L. W., & Ramesh, R. (2009). A strain-driven morphotropic phase boundary in bifeo₃. *Science*, 326(5955), 977–980.
- Zhang, S. T., Lu, M. H., Wu, D., Chen, Y. F., & Ming, N. B. (2005). Larger polarization and weak ferromagnetism in quenched bifeo₃ ceramics with a distorted rhombohedral crystal structure. *Applied Physics Letters*, 87(26), 262907.
- Zhao, T., Scholl, A., Zavaliche, F., Lee, K., Barry, M., Doran, A., Cruz, M. P., Chu, Y. H., Ederer, C., Spaldin, N. A., Das, R. R., Kim, D. M., Baek, S. H., Eom, C. B., & Ramesh, R. (2006). Electrical control of antiferromagnetic domains in multiferroic bifeo₃ films at room temperature. *Nat Mater*, 5(10), 823–829.
- Zhou, J.-S., Goodenough, J. B., Gallardo-Amores, J. M., Moran, E., Alario-Franco, M. A., & Caudillo, R. (2006). Hexagonal versus perovskite phase of manganite rmno_3 r=(y, ho, er, tm, yb, lu). *Phys. Rev. B*, 74, 014422.